



**OPTICAL FIBRE BRAGG GRATING  
ANALYSIS THROUGH FEA AND ITS  
APPLICATION TO PRESSURE  
SENSING**

**NITHILA DEDIYAGALA**

A thesis submitted in fulfilment of the requirements for the degree of  
**DOCTOR OF PHILOSOPHY**

2019

**COLLEGE OF ENGINEERING AND SCIENCE  
VICTORIA UNIVERSITY**

## **DECLARATION**

"I, Nithila Dediyagala, declare that the PhD thesis entitled 'Optical fibre Bragg grating analysis through FEA and its application to pressure sensing' is no more than 100,000 words in length including quotes and exclusive of tables, figures, appendices, bibliography, references and footnotes. This thesis contains no material that has been submitted previously, in whole or in part, for the award of any other academic degree or diploma. Except where otherwise indicated, this thesis is my own work".

Signature:

Date: 06/06/2019

## ABSTRACT

The focus of this thesis is developing optical fibre Bragg grating (FBG) pressure sensors with enhanced sensitivity for use in a low (gauge) pressure range (0 - 50 kPa) together with understanding observed non-linear behaviour. To appreciate the behaviour of FBG sensor spectra, it is necessary to understand geometrical and material properties of FBGs. The thesis is an in-depth investigation of the behaviour of FBGs including their manufacturing and fabrication process details. A new computational approach has been introduced to simulate FBG structures based on how the FBG fabrication process produces changes in refractive index.

There are various numerical analysis methods existing for analysing fibre Bragg grating structures and their spectral properties. Although computation design and simulations are used extensively in engineering problems, current computational approaches do not combine FBGs formation and their resultant spectra. In this study, this has been addressed by developing a simple Finite Element Analysis (2-D) model using the *Wave Optics* module in COMSOL Multiphysics simulation software. The 2-D model was developed considering the phase mask method commonly used to fabricate FBGs. It simulates a complex grating structure which is useful for manufacturers and researchers. The 2-D model then creates a unit cell of a grating structure which is able to be implemented within an optical fibre. The model allows users to decide the length of the grating by selecting the number of unit cells required. By changing the geometrical parameter of a unit cell of the 2-D phase mask structure, it was possible to demonstrate formation of complex grating structures. There have been many studies reported for ideal gratings; however, much less attention and research has been given to the spectra produced by these complex FBG structures. Therefore, this study specially focuses on complex grating structures and their spectral behaviour. The developed 2-D model successfully reproduced observed complex grating structures arising with the use of multiple phase masks orders, with theoretically acceptable results for the spectrum produced. Furthermore, the 2-D model of the phase-mask method was also able to produce tilted gratings by changing the incident angle of light on the phase mask. Therefore, this FEA approach provides insight into not only complex FBG structures but also tilted FBGs using a simple

computational tool which will be useful in further research to understand the behaviour of a variety of FBG structures. For this study, material properties of standard single mode fibre (SMF-28) was considered. However, the model is able to simulate any optical fibre used in FBG fabrication by changing the material properties.

The thesis also considers the understanding of FBG pressure sensors and observed non-linear behaviour. Therefore, a thorough literature review was carried out to find the influence of structural and material properties of optical fibres and FBGs which is believed to be the cause of non-linear behaviour. It investigates in depth the birefringence effect on fibres due to point load and distributed load on FBGs using the *Structural Mechanics* and *Wave Optics* module in COMSOL software. Many research studies have employed a plane strain assumption for structural mechanics problems; however, they do not clearly explain the true nature of FBGs under stress generalized strain. This study overcomes that problem by introducing proper mathematical equations to develop 3-D behaviour in a 2-D computational model. The behaviour of a distributed load on FBGs was discussed in detail with the help of the computational model. It provides new information about an asymmetric peak produced as a result of birefringence effects.

The research proposes a new FBG uniform pressure sensor using a 2-D computational model. It was designed in simulation by adding a polymer material to the cladding of an SMF-28 by reducing the cladding diameter. In this study, polymers of PDMS and PTFE were chosen to further investigate the pressure enhancement in the suggested pressure range. The results show similar pressure sensitivity for both materials. Both materials are highly capable of enhancing pressure sensitivity in the range of 0 – 50 kPa. The suggested pressure range is most suitable for biomedical application. The positive results of the current study lend credibility for using the envisaged sensor for commercial use.

## LIST OF PUBLICATIONS

Peer reviewed conference papers:

Dediyagala, N., Baxter, G. W., Sidiropoulos, F. & Collins, S. F. 2016, *FEA and FFT modelling of harmonics from fibre Bragg gratings*, paper presented at the 2016 Australian Institute of Physics (AIP) Congress, Brisbane, Australia.

Dediyagala, N., Baxter, G. W., Sidiropoulos, F. & Collins, S. F. 2014, *Comparison of experimental, theoretical and Finite Element Analysis on fibre Bragg grating pressure sensitivity*, paper presented at the 2014 Australian Institute of Physics (AIP) Congress, Canberra, Australia.

## **ACKNOWLEDGEMENTS**

My journey through PhD in Victoria University has given me a transition period of my life. Completion of the thesis is the end of that journey and one of my biggest achievements. This journey would not be completed without tremendous support given to me by many great people around me. Hence, it is my duty to thank and acknowledge all of them and share all the credit with them.

First and foremost, I would like to dedicate my sincere thanks to Professor Gregory Baxter for his continued support, guidance and valuable comments as my senior supervisor. I would like to dedicate my heartfelt appreciation for my co-supervisor, Professor Stephen Collins, for his great guidance, valuable and constructive comments. This thesis would not be completed without his tremendous support throughout the entire process. My sincere thanks go to co-supervisor, Dr. Fotios Sidiropoulos for his constructive suggestions and encouragements during this whole time. I greatly appreciate their kindness and friendship during the research. Thanks also go to Dr. Nicoleta Dragomir for her valuable suggestions and comments in the early stage of the research.

I am deeply grateful for Victoria University for accepting me as a PhD student and providing financial support for the proposed project. I would also like to thank all administration staff and technical staff in the School of Engineering and Science for their valuable support during this period. This is also the time to remind the support and encouragement from dear colleagues Dr. Robab Antonios, and Dr. Wan Hafiza, who have become forever friends of mine. I am also indebted to the support provided by team of COMSOL Multiphysics® simulation software. This project would not be possible and successful without their useful comments and support.

I would also like to extend my gratitude and admiration to my siblings for their continuous and devoted support throughout the research. Millions of thanks go to my beloved parents, my mother, Daya Dediya Gal and my late father, Somapala Dediya Gal for their inspiration, encouragement and unconditional support and love from my childhood. I owe a huge debt of gratitude to my mother

in law, Mallika Dias, for her continuous support and inspiration throughout my research.

Last but not least, my heartfelt thanks go to my beloved husband and mentor, Pushpitha Kalutara. His continuous support and inspiration has made me achieve this possible and his remarkable understanding and commitment to family during this difficult period is outstanding. I have been blessed and honoured to have such a lovely husband who is quite considerate not only me but also our children. Finally, my most heartfelt thanks go to my million-dollar smile son, Kemith, and darling daughter, Ranli, both were born during the time of research who have given me the determination to complete this target. Every day, your smiles made me happy and forgot my tough times during the research. Being your mother is the most amazing thing happened to me.

## TABLE OF CONTENTS

DECLARATION .....	II
ABSTRACT .....	III
LIST OF PUBLICATIONS.....	V
ACKNOWLEDGEMENTS.....	VI
TABLE OF CONTENTS .....	VIII
LIST OF FIGURES.....	XII
LIST OF TABLES .....	XIX
CHAPTER 1: Introduction .....	1
1.1 Overview .....	1
1.2 Why optical fibre technology? (Optical based method and advantages)	2
1.3 Why Fibre Bragg Grating (FBG) pressure sensors? .....	4
1.4 Motivation and significance .....	6
CHAPTER 2: Optical Fibres, FBGs and FBG fabrication .....	9
2.1 Overview .....	9
2.2 Optical fibre and its properties.....	9
2.3 Fibre Bragg Gratings .....	14
2.3.1 Photosensitivity.....	14
2.3.2 Classification of Fibre Bragg Gratings .....	16
2.4 Theory of Fibre Bragg Gratings.....	20
2.4.1 FBG fabrication methods .....	21
2.4.2 Theory of FBG fabrication technique by a phase mask .....	25
2.4.3 Induced Bragg period, index of refraction change and reflectance	26

2.4.4	Grating formation with multiple phase mask orders .....	27
2.4.5	Induced reflectance and spectral characteristics .....	31
2.5	Summary.....	34
CHAPTER 3: Pressure measurement using FBGs .....		35
3.1	Overview .....	35
3.2	Fibre Bragg Grating pressure sensors .....	35
3.2.1	Uniform pressure .....	36
3.2.2	Transverse compressive load.....	38
3.3	Refractive index variation and stress variation with pressure.....	39
3.4	Material properties.....	40
3.5	Bragg wavelength monitoring; experimental and theoretical .....	42
3.6	Summary.....	45
CHAPTER 4: Finite Element Analysis (FEA).....		46
4.1	Overview .....	46
4.2	Why Finite Element Analysis (FEA)?.....	46
4.3	Introduction (History) of Finite Element Analysis (FEA).....	48
4.3.1	Finite Element Analysis (FEA) .....	48
4.4	Finite Element Analysis of modes in optical fibres at $\lambda_B$ , $2\lambda_B$ and $(\frac{2}{3})\lambda_B$	
	52	
4.4.1	Modes at $\lambda_B$ and $2\lambda_B$ .....	53
4.4.2	Modes at $\frac{2}{3}\lambda_B$ .....	56
4.5	Computation modelling of FBG and their spectra.....	58

4.5.1	FEA on complex FBG formed by phase mask under UV illumination	59
4.5.2	FEA on wave spectrum produced by complex FBG structure .....	69
4.6	FFT analysis of the diffracted distribution intensity of higher order phase mask and FEA of reflection spectra at different wavelengths.....	72
4.6.1	Normal incidence of the light on Phase mask.....	72
4.6.2	FFT analysis at different position of intensity variation along the core of the fibre.....	74
4.7	Spectral analysis of fibre Bragg Gratings patterns .....	79
4.8	Summary.....	83
CHAPTER 5:	Finite Element Analysis on pressure sensitivity (Computational design)	86
5.1	Overview .....	86
5.2	Pressure exertions on FBGs .....	86
5.3	FEA on point load and distributed load.....	87
5.3.1	FEA for uniform pressure.....	88
5.3.2	Physical domain of the model.....	89
5.3.3	Mathematical model.....	89
5.3.4	Boundary conditions .....	93
5.3.5	Finite Element Analysis .....	96
5.3.6	Analysis (Post processing) .....	98
5.4	Result for point load and distributed load simulation .....	98
5.4.1	Effective mode indices change with temperature and point load ..	99
5.4.2	Behaviour under a distributed load .....	105

5.5	Results of uniform pressure sensing .....	110
5.5.1	Bare fibre .....	110
5.5.2	Polymer Coated Fibre.....	111
5.6	Summary.....	117
CHAPTER 6: Conclusion and future works .....		119
6.1	Key outcomes .....	119
6.2	Future work .....	122
REFERENCES.....		124

## LIST OF FIGURES

Figure 1.1: Patent data accepted in (Patent Insight Pro, 2011) shows the differentiation in terms of number of patent issued of distributed sensing approaches, Bragg grating and interferometric sensors (Kersey, 2012) .....	1
Figure 1.2: Fibre Optic Sensor Global Consumption Market Forecast (Values in \$ Billions) (Electronicast, 2012) .....	2
Figure 2.1: Schematic diagram of (a) end view and (b) side view of an optical fibre - x, y and z show the direction of axis of the fibre which is used throughout the study.....	9
Figure 2.2: Schematic diagram of transmission of a light ray in an optical fibre	10
Figure 2.3: Electric field of lowest 12 modes of corresponding LP modes in step index fibre (Ma, 2009). ....	12
Figure 2.4: Normalized frequency (V) Vs normalized propagation constant (b) (Keck, 1981). The vertical line applies to $(\frac{2}{3})\lambda_B$ for SMF-28 fibre (assuming $\lambda_B = 1550$ nm). ....	13
Figure 2.5: Transmission and reflection spectra due to FBG.....	20
Figure 2.6: Optical system for interferometric inscription of FBGs (a) transverse holographic method and (b) phase mask method .....	22
Figure 2.7: Optical system for Interference Lithographic method .....	23
Figure 2.8: Image of 400 nm grating in photoresist Transfer the photoresist grating pattern into substrate (fused silica) - (Chen & Schattenburg, 2004) .....	25
Figure 2.9: Image of Scanning Electron Microscopy of 400 nm grating in fused silica (Buchwald, 2007) .....	25
Figure 2.10: FBG writing method using phase mask (a) Interference of first order diffraction behind phase mask by forming a uniform grating structure (b) Interference of higher orders diffractions including zeroth order by forming a complex FBG structure.....	26

Figure 2.11: The induced index changes along the longitudinal axis of fibre core to a FBG - the colour spectrum shows variation of index change in FBG region	27
Figure 2.12: DIC images of the fibre core containing Bragg grating, recorded for two different fibre orientation (a) the images was taken from a direction parallel to the writing UV laser beam and (b) after rotating 90 degrees from (a) (Dragomir, 2004)	28
Figure 2.13: DIC microscopy images of FBG in core region of Type 1 fibre at different orientation to the writing beam (a) Images of fibre orientation is perpendicular to the writing beam (b) Images of fibre orientation is parallel to the writing beam (c) schematic diagram of writing technique and image planes orientation to the writing beam (d) Schematic diagram of (b) showing the interleaving planes belongs to index modulation of $\Lambda_{pm}$ and $\Lambda_{pm}/2$ ; $Z_T$ is Talbot length (Rollinson, 2012)	28
Figure 2.14: Modelled intensity variation in the core area of the fibre due to contribution of multiple diffraction orders from phase mask fabrication (Kouskousis et al., 2013)	29
Figure 2.15: Reflection (a) and transmission (b) of uniform Bragg grating	32
Figure 3.1: Schematic diagram of typical FBG sensing system	42
Figure 4.1: Representation of Boundary Value Problem	48
Figure 4.2: Schematic diagram of volume discretization method in FEA (a) the object which represent the problem (b) the object is divided into number of small units which is called elements (c) elements are a combination of points and lines or surfaces	50
Figure 4.3: Flow chart of FEA process	51
Figure 4.4: End face of optical fibre of SMF-28 and its mesh diagram	53
Figure 4.5: Electrical field profile across optical fibre for a guided mode	54

Figure 4.6: (a) Electric field variation of HE <sub>11</sub> in the fibre surface and (b) Intensity variation along z direction across fibre core (b) at $\lambda_B$ .....	55
Figure 4.7: (a) Electric field variation of HE <sub>11</sub> in the fibre surface and (b) intensity variation along z direction across fibre core at $2\lambda_B$ .....	55
Figure 4.8: Electric field variation of HE <sub>11</sub> in the fibre surface and electric field variation along x direction across fibre core at $(\frac{2}{3})\lambda_B$ .....	56
Figure 4.9: Electric field variation of TM <sub>01</sub> in the fibre surface and electric field variation along x direction across fibre core at $(\frac{2}{3})\lambda_B$ .....	56
Figure 4.10: Electric field variation of TE <sub>01</sub> in the fibre surface and electric field variation along x direction across fibre core at $(\frac{2}{3})\lambda_B$ .....	57
Figure 4.11: Electric field variation of HE <sub>21</sub> in the fibre surface and electric field variation along x direction across fibre core at $(\frac{2}{3})\lambda_B$ .....	57
Figure 4.12: Electric field variation of each mode in the fibre surface x direction across the fibre core at $(\frac{2}{3})\lambda_B$ .....	58
Figure 4.13: Schematic diagram of phase mask structure .....	59
Figure 4.14: Schematic diagram of beam splitting at phase mask with respect to the angle of incident .....	60
Figure 4.15: Schematic diagram of FBG writing process using phase mask method for a unit cell .....	62
Figure 4.16: Schematic diagram of boundary conditions on the model, inside of dashed line will be used to show the relevant mesh in Figure 4.18 .....	65
Figure 4.17: Schematic diagram of S-parameter.....	67
Figure 4.18: Mesh diagram of the FEA domain around phase change area in Figure 4.16 .....	68
Figure 4.19: Schematic diagram of FBG structure in SMF-28, and parameter values used .....	70

Figure 4.20: Diagram of boundary conditions for light propagation through a FBG	71
Figure 4.21: Mesh diagram of optical fibre .....	72
Figure 4.22: Simulated intensity spectrum along the fibre core using phase mask method (red and yellow lines represent the line scans along the fibre core and Talbot length respectively).....	73
Figure 4.23: Line profile of intensity distribution at -71.00 $\mu\text{m}$ along the fibre core .....	74
Figure 4.24: Evaluated harmonics using FFT for intensity distribution of Figure 4.23, i.e. line scan at -71.00 $\mu\text{m}$ .....	74
Figure 4.25: Line profile of intensity distribution at -71.75 $\mu\text{m}$ along the fibre core .....	75
Figure 4.26: Evaluated harmonics using FFT for intensity distribution of Figure 4.25 i.e. line scan at -71.75 $\mu\text{m}$ .....	75
Figure 4.27: Line profile of intensity distribution at -73.35 $\mu\text{m}$ along the fibre core .....	76
Figure 4.28: Evaluated harmonics using FFT for intensity distribution of Figure 4.27, i.e. line scan at -73.35 $\mu\text{m}$ .....	76
Figure 4.29: FBG pattern was obtained using phase mask technique, the colour line represents the refractive index value of FBG pattern.....	79
Figure 4.30: Simulated FBG reflection spectrum at $\lambda_B$ for complex FBG pattern of Figure 4.29, obtained by phase mask method.....	80
Figure 4.31: Simulated FBG reflection spectrum at $2\lambda_B$ , obtained for complex FBG pattern .....	81
Figure 4.32: Resultant FBG reflection spectrum at $(\frac{2}{3})\lambda_B$ by complex FBG pattern .....	82
Figure 4.33: Tilted FBG pattern obtained by phase mask method .....	84

Figure 5.1: Possible forms of pressure exertion on an optical fibre (a) Transverse compressive load, (b) Tensile and compressive strain, (c) Uniform pressure ..	87
Figure 5.2: Schematic diagram of 2D cross section of point load (a) and distributed load (b) on FBG .....	88
Figure 5.3: Schematic diagram of a 3-D cylindrical fibre (a) and simplified (2-D cross section) view of the same FBG due to axial symmetry (b) .....	88
Figure 5.4: Schematic diagram of computational domain for point load (a) and mesh diagram (b) .....	93
Figure 5.5: Schematic diagram of computational domain for distributed load on an optical fibre (a) and boundary conditions (b) .....	94
Figure 5.6: Schematic diagrams of bare fibre (a) and polymer coated fibre (b) experiencing uniform pressure in cylindrical coordinates .....	94
Figure 5.7: Screen shot of wave equation is set under electromagnetic wave, frequency domain in COMSOL.....	96
Figure 5.8: The domains of distributed load with its defining mesh .....	97
Figure 5.9: Mesh diagram on the uniform pressure sensing on bare fibre .....	98
Figure 5.10: Effective mode index variations, with and without stress-optic relations when reference temperature is 20 °C (a) and 1000 °C (b) .....	99
Figure 5.11: Effective mode variation with plain strain and generalized plain strain when reference temperature is 1000 °C .....	100
Figure 5.12: Power flow across modes across end face of the fibre. ....	101
Figure 5.13: Power flow variation on the end face of the fibre due to 0 N (a), 20 N (b) and 40 N (c).....	102
Figure 5.14: Stress variations along x (a), y (b) and z direction (c) and along the middle of the fibre as shown in red line (d) .....	103
Figure 5.15: Stress variations in the x (a), y (b) and z direction (c) and in the middle of the fibre line as shown in (d) .....	104

Figure 5.16: Graph of effective mode index variations with applied load for distributed load fibre .....	105
Figure 5.17: Intensity variation on the end face of the fibre with different loads .....	106
Figure 5.18: Intensity of all effective mode values along z direction.....	106
Figure 5.19: Stress variations along x (a), y (b), z direction (c) along middle of the fibre as shown in red line (e) and relevant effective mode index for different loads (d).....	107
Figure 5.20: Stress variations along x (a), y (b), z direction (c), along middle of the fibre as shown in red line (d) and, relevant effective mode index for different loads.....	108
Figure 5.21: Index of refraction changes in (a) x and y directions are calculated using equations and simulation results (b) birefringence, in the centre of the fibre .....	109
Figure 5.22: (a) Bragg wavelength change in x and y directions and (b) Bragg wavelength in x and y directions for a distributed load .....	110
Figure 5.23: Graph of radial axial and radial strain (a) and stress (b) vs pressure .....	110
Figure 5.24: Pressure vs wavelength shift.....	111
Figure 5.25: (a) Wavelength shift Vs pressure and (b) 2D cross section view of structure deformation due to pressure experience (b).....	112
Figure 5.26: Strain (a) and stress (b) variation along axial and radial directions on the centre of the fibre .....	113
Figure 5.27: Experiment results of (a) wavelength shift vs pressure graph for PDMS (Cooksey & Ahmed, 2016), (b) simulation results for wavelength shift vs pressure for PDMS and PTFE.....	114

Figure 5.28: Wavelength shift vs pressure, without any diameter deduction of the fibre cladding (a), wavelength shift after 30 µm deduction from the cladding of the fibre .....	115
Figure 5.29: Wavelength shift vs pressure graph for PTFE and PDMS when fibre diameter is 30 µm .....	116

## LIST OF TABLES

Table 1.1: Collection of exemplary standards for medical pressure analysis ....	7
Table 1.2: Medical areas and the research impact on FBG based sensors .....	8
Table 2.1: Properties of SMF-28 fibre .....	13
Table 2.2: Physical and material properties of SMF-28 (FEA simulation) .....	14
Table 2.3: Types of FBGs, their characteristics and properties ((Canning, 2008)) .....	18
Table 3.1: Summary of FBG-based pressure sensors, in order of pressure sensitivity for bare/polymer coated/mechanical/force multipliers .....	36
Table 3.2: Reported material values for the silica fibre and the calculated pressure sensitivity.....	42
Table 4.1: Parameters and values for the simulation* .....	59
Table 4.2: The calculated and defined parameters for the simulation .....	66
Table 4.3: Results of spectral components of SMF-28 for simulated FBG patterns: evaluated grating periods using FFT analysis and their harmonics, fraction of period compare to the phase mask period, calculated wavelength using Equation 2.10 and ratio of calculated wavelength to Bragg wavelength.....	77
Table 4.4: Results of diffracted efficiency of harmonics for different line scans and the expected efficiencies according to the manufacturer information .....	77
Table 4.5: Calculated Talbot length (in free space) of the diffracted pattern produced by the phase mask with period of $1.066 \mu\text{m}$ , index of refraction of 1.488 and wavelength at 244 nm. ....	78
Table 5.1: Material properties of selected polymers .....	112
Table 5.2: Material properties of PTEF and PDMS .....	114
Table 5.3: Pressure sensitivity of selected materials.....	115

Table 5.4: Pressure sensitivity by different materials under different pressure and changing diameter ..... 116

Table 6.1: Mapping key outcomes of the study with the initial objectives ..... 121

# CHAPTER 1: Introduction

## 1.1 OVERVIEW

The invention of fibre optic wire or “Optical Waveguide Fibres” by Corning Glass researchers in 1960 has had a tremendous impact on global communication as it revolutionized the telecommunications industry. Fibre optics is a major industry and today it plays a key role in modern day life such as long-distance telephone service, internet and use in health care services. The invention of the fibre-optic gyroscope in 1976 led fibre optic sensor explorations for the next ten years (McLandrich & Rast, 1978). Commercialization of optical fibres provides more components for other uses which have led to the opportunity for their use as sensors in many field applications. Since then various ideas have been suggested and techniques have been developed for many measurands and applications. According to statistics presented at OFS-15 (Optical Fibre Sensors Conference held in Portland, Oregon, USA 2002), strain and temperature are the most highly studied measurands, with fibre Bragg grating (FBG) sensors becoming increasingly popular. According to statistics of OFS-22, FBG sensors had the highest number of patent issued among optical fibre sensors (Kersey, 2012). Figure 1.1 illustrates FBG sensor popularity, as derived from an industry survey (Patent Insight Pro, 2011).

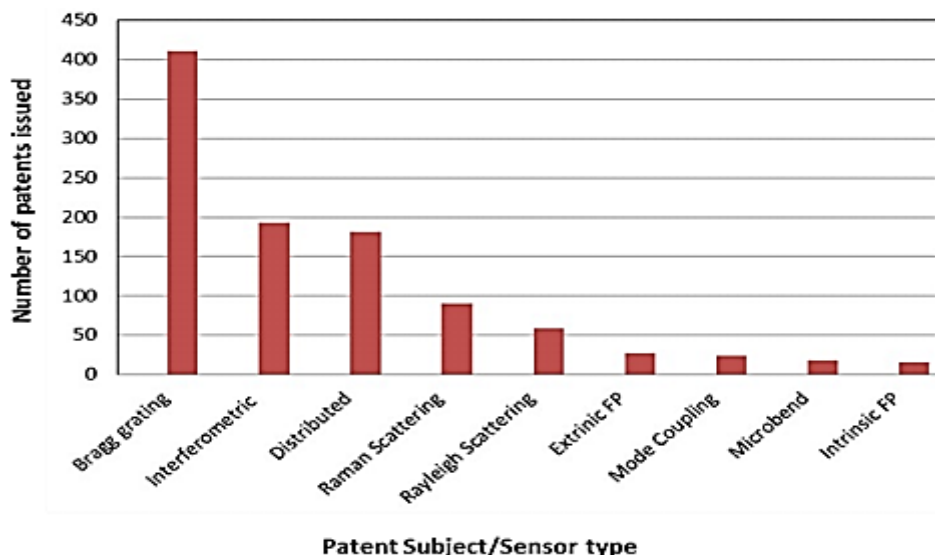
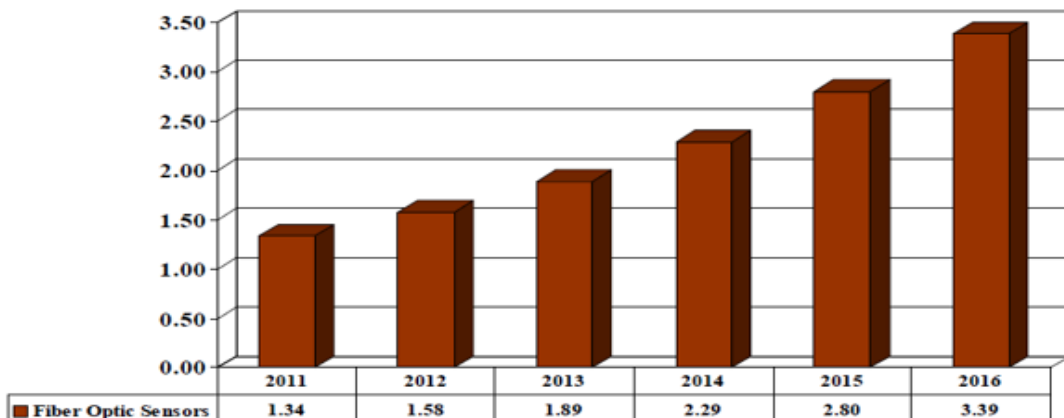


Figure 1.1: Patent data accepted in (Patent Insight Pro, 2011) shows the differentiation in terms of number of patent issued of distributed sensing approaches, Bragg grating and interferometric sensors (Kersey, 2012)

FBG sensors have attracted a considerable amount of interest in a vast range of applications due to their wavelength-encoded character and linear response to changes in various measurands (Hill & Meltz, 1997; Othonos & Kyriacos, 1999). Figure 1.2 shows the annual investment in fibre optics sensors including FBG sensors from 2011 - 2016. It shows 20.5% (from \$1.34 to \$3.39 billion) of estimated annual growth rate of fibre optics sensors, which further signifies their importance (Electronicast, 2012; Méndez, 2007).



*Figure 1.2: Fibre Optic Sensor Global Consumption Market Forecast (Values in \$ Billions) (Electronicast, 2012)*

## **1.2 WHY OPTICAL FIBRE TECHNOLOGY? (OPTICAL BASED METHOD AND ADVANTAGES)**

The major concern of any sensor device is their production, performance and addressing of issues which are relevant for their intended applications. Their capacity depends on sensor characteristics, the external environment, and physical characteristics of the instrument, safety, performance, installation and maintenance, type of use, signal conditioning and price. In this context, optical fibre has become a potential candidature for sensing applications largely due to its high sensitivity, small size, light weight, price, material properties and sensing capabilities. Other main advantages of fibre optics sensors are chemical passivity, high temperature tolerance, immunity to electromagnetic interference (EMI) and long life with possibility of use in a harsh environment. Many researchers have undertaken studies to identify the advantages of optical fibres and their possible applications in many different fields over conventional electronic and electric sensors. Today optical fibre sensors are largely applied in

chemical, biological, aviation, healthcare, automation industries, illustrating how it has been valuable and a promising technology for industrial applications (Annamdas, 2012).

Fibre optic sensors can be categorized into extrinsic and intrinsic sensors (Othonos & Kyriacos, 1999). Extrinsic sensors are mostly used in harsh condition where most of the other sensors are unable to operate. In these sensors, fibre is used as an information carrier but the interaction between the light and the quantity of the measurement takes place outside of the fibre itself. This means the transducer is external to the fibre; hence, these sensors are called extrinsic sensors. They are mostly used in industry to measure rotation, vibration velocity, displacement, twisting, torque and acceleration. In contrast, intrinsic sensors behave differently where the optical fibre becomes the sensing element itself by keeping the propagating light inside and which experiences modulation when the fibre is subjected to pressure, strain or temperature variation. These sensors are used to measure intensity, phase, polarization, wavelength or transit time of light. The simplicity of intrinsic sensors has attracted many industries like, aviation, civil engineering for physical measurements.

Currently available fibre optic sensors can be mainly classified into four major categories based on the operating principle:

1. Intensity
2. Phase (interferometric)
3. Polarization
4. Wavelength

Their advantages and disadvantages for pressure sensing are discussed below.

Major disadvantages of intensity-based sensors are fibre loss, power fluctuation of the power source and large hysteresis. In the current market, there are three types of interferometric pressure sensors utilised for pressure measurement; they are: Mach-Zehnder, Michelson and Fabry-Perot. Among them, the first two sensors are mostly considered for acoustic pressure sensing. However, all of them are limited in their application in commercial use due to the small photoelastic effect, thermal instability or polarization fading (effects for fringe

visibility). The next sensor type are polarization-modulated fibre optics sensors, which were not successful in pressure sensing in hazardous conditions due to its bulk size. Hence, all three sensor types have been limited in commercial use due to the issues above. However, the fourth sensor type, namely FBG sensors which are based on wavelength/spectrum modulation have been attractive to many industries due to their ability to overcome the aforementioned issues and offer specific advantages. FBG sensors and their advantages will be discussed below.

### **1.3 WHY FIBRE BRAGG GRATING (FBG) PRESSURE SENSORS?**

Pressure measurement is vital in many industrial applications: aviation, bio-medical, oil and gas are some of them. Many sensors have been commercialized for pressure measurements from extreme vacuum ( $10^{-12}$  Pa) to explosion ( $10^{+12}$  Pa), the latter implying a flammable or harsh environment in some fields of application. In this range, optical fibre sensors have been identified as a potential solution for use as pressure sensors (Pinet, 2011) due to properties which are outlined in section 1.2.

Optical fibre photosensitivity was first discovered in germanium-doped silica optical fibres when an optical fibre core was exposed to a periodic pattern of ultraviolet (UV) light by Hill and co-workers (Hill, 2000; Hill et al., 1993). During the exposure to UV light, there was some intensity of light back-reflected which increased with time. Spectral responses confirmed the reflectivity was a result of a periodic modulation of the photo-induced refractive index change created along the core of the optical fibre. This triggered a new class of in-fibre component, now known as a Fibre Bragg Grating (FBG). The resultant central wavelength of back reflected light of a FBG depends on the effective index of refraction of the core and the grating periodicity. When a FBG experiences strain or a temperature change the effective index of refraction and grating periodicity are also affected. As a result, the changes of these two physical parameters have provided a means to measure temperature and strain variations. FBGs have hence emerged as a favourable sensing element owing to their potential use in measuring strain, temperature and pressure.

The main advantage of FBG sensors is their unique wavelength-encoded nature, as noted in Section 1.1 When an FBG experiences temperature, tension, bending

compression and impact, its material and physical properties change such as refractive index and grating length, with the Bragg condition providing the reflection wavelength of light launched into the fibre. Therefore, FBGs have become more popular in pressure, strain and temperature measurement. Their versatility, reliability and ease of embedding in a variety of structures make their use possible in smart structure applications. Moreover, the size of these sensors has been carefully considered and developed for biomedical application. FBGs are also popular in applications like robotics due to resolution, sensitivity and dielectric properties and multiplexing capability.

FBG sensors are popular not only for one parameter sensing but also multi-parameter sensing such as strain and temperature. Many sensors have been reported for multi-parameter sensing such as strain and temperature measurement simultaneously using pairs of FBGs operating at two different wavelengths (Brady et al., 1997; Echevarria et al., 2001) or using two different types of FBGs (Shu et al., 2002). A multi-axis strain sensor has been reported for multidimensional strain measurement such as transverse and longitudinal strain sensing using FBGs inscribed in birefringent optical fibre (Udd et al., 2002; Udd et al., 2000)

Although FBG sensors are more popular among optical fibre sensors a few drawbacks can be identified (Mihailov, 2012). First, the lifetime of these sensors which has been questioned when exposed to harsh environments. It has also been reported that degeneration of material and physical properties has occurred, especially in high temperature and pressure environments. Two more disadvantages are the possible need for compensation due to cross sensitivity between temperature and strain and inability to replace them if they are damaged especially for embedded sensors. However, the most critical issue of these sensors in pressure measurement is low sensitivity over a wide pressure measurement range and thus a difficulty in applying them in a very low (gauge) pressure range as elaborated on below. This has limited their application in low pressure measurement which is characteristic of important fields such as the environment, sport and biomedicine.

Although FBGs are potential candidates for pressure sensors, some drawbacks have been identified. FBGs inscribed in bare silica fibre exhibit a linear response over a large pressure range (0-70 MPa) but their sensitivity is low due to their material properties (Othonos & Kyriacos, 1999). Fibre is made of glass, which is less stiff than metal but stiffer than plastics, having a high Young's modulus and low Poisson's ratio. Although the pressure response is linear at high pressures, at moderate pressure (< 0.2 MPa) it is difficult to measure due to the very low sensitivity (Hill & Meltz, 1997). Furthermore, the response has been observed to become non-linear (Bal et al., 2011; Lawrence et al., 1999). Modification of the physical properties of optical fibre by application of a suitable coating has been pursued by many authors, including for improving their response to external pressure, as noted by Giallorenzi et al. (1982). Thus, having considered the above issues, the main objective in this research is to investigate the behaviour of FBGs at moderate (gauge) pressures (0 – 0.5 *atm*, i.e. 0 - 50 kPa) when an optical fibre is coated with a polymer material, since this should improve their pressure response, by lowering the Young's modulus and increasing their Poisson's ratio. This will include studies of various polymer materials as fibre coatings and noting how this affects the sensitivity of FBG pressure sensitivity in each case.

#### **1.4 MOTIVATION AND SIGNIFICANCE**

A variety of pressure sensors have been developed investigating various ranges of pressures from very low to extremely high. But the cost of pressure sensors and their failure in some field applications have questioned their reliability and extended operation. Therefore, developing new methodologies and techniques to produce optimum devices is a necessity for current and future industrial requirement. Investigation of optical FBGs for sensing applications significantly contributes to producing more low cost, highly sensitive, durable and reliable devices. However, some material properties of optical fibres limit their application in pressure sensing. Due to this reason, the proposed research focuses on gaining a greater understanding of and thereby improving the performance of FBG sensors with different coatings in pressure sensing applications, at moderate gauge pressures. To achieve this, it is necessary to understand FBGs

spectra, their behavior under pressure and the effect of coating materials. Therefore, the main objectives of the study can be stated as follows:

- Model FBGs structures and their spectra using Finite Element Analysis (FEA) methods
  - Analyze their spectra for better understanding of their relationship with the underlying FBG complex refractive index variation;
- Model FBGs with different polymer coatings using a FEA method to identify suitable materials for enhancing the pressure sensitivity at moderate pressures
  - Compare the results with existing literature to confirm efficacy of the findings in simulations.

As an example, Table 1.1, shows that for the medical fields of urology, neurology, gastroenterology and ophthalmology, the pressure range of interest is between 0 – 30 kPa. Therefore, the pressure range under consideration (0 - 50 kPa) is highly applicable in these fields.

*Table 1.1: Collection of exemplary standards for medical pressure analysis (Poeggel et al., 2015)*

Area (Technique)	Body Part	Min. Pressure	Max. Pressure	Pressure Resolution	Sampling (Frequency)	Additional
Cardiology (BP Monitoring)	Heart, Veins, Arteries	-4 kPa (-30 mmHg)	40 kPa (300 mmHg)	13 Pa (0.1 mmHg)	200 Hz	Volume restricted
Urology (Cystometry)	Bladder, Abdomen	0 Pa (0 cmH <sub>2</sub> O)	25 kPa (250 cmH <sub>2</sub> O)	50 Pa (0.5 cmH <sub>2</sub> O)	10 Hz	Differential measurement
Neurology (ICP Monitoring)	Brain, Skull, Dural Tissue	0 Pa (0 mmHg)	13.3 kPa (100 mmHg)	260 Pa (2 mmHg)	-	Sterilization
Pulmonology (Transpulmonary)	Respiratory Tract, Lungs	-10 kPa (-100 cmH <sub>2</sub> O)	15 kPa (150 cmH <sub>2</sub> O)	2–40 Pa (4 mmH <sub>2</sub> O)	200 Hz (10 Hz)	Temperature, humidity
Gastroenterology (Manometry)	Stomach, Colon	0 Pa (0 mmHg)	13.3 kPa (100 mmHg)	-	8 Hz	Multi probes (6 or more)
Ophthalmology (Tonometry)	Eyes	0 Pa (0 cmH <sub>2</sub> O)	8 kPa (60 mmHg)	13 Pa (0.1 mmHg)	100 Hz	Volume restricted
Rheumatology	Muscle, Bones, Spine	0 kN * <sup>2</sup>	3 kN * <sup>2</sup>	-	-	High pressure
Cancer Treatment (Ablation)	Full Body	0 kPa * <sup>3</sup>	200 kPa * <sup>3</sup>	-	-	Temperature, RF-field

Table 1.2 lists the research already reported for fibre optic sensors in biomedical applications and highlight the possible area for further developed FBG-based sensors. In the field of neurology, a Fabry Perot interferometer (FPI) has been reported but there has not reported any application of a FBG sensor yet, and the

pressure range of 0 – 50 kPa is of interest. There are a limited number of publications that have been published in the areas listed in Table 1.2, showing the potential for the sensor investigated in this study using computational design. Consequently, there is significant motivation to explore the feasibility of developing a FBG pressure sensor for the 0 – 50 kPa range. This thesis achieves that objective by developing a COMSOL model to test the effectiveness of using a polymer coating on a standard glass fibre with an embedded FBG.

*Table 1.2: Medical areas and the research impact on FBG based sensors  
(Poeggel et al., 2015)*

Medical Area	Modulation Type	Place	Temperature Compensation	Sensor State	Already Explored	Research Impact
Cardiology	Intensity, FPI, FBG	<i>in vivo</i> , <i>ex vivo</i>	No	100 % * <sup>1</sup>	70 %	70 %
Neurology	Intensity, FPI	<i>in vivo</i>	No	100 % * <sup>1</sup>	70 %	60 %
Gastroenterology	FPI, FBG	<i>in vivo</i>	Possible	70 %	50 %	60 %
Pulmonology	Intensity	<i>in vivo</i> , <i>ex vivo</i>	No	30 %	20 %	20 %
Ophthalmology	FPI, FBG	<i>ex vivo</i>	No	40 %	20 %	30 %
Urology	Intensity, FPI + FBG	<i>in vivo</i>	Yes	60 %	30 %	40 %
Rheumatology	Intensity, FBG	<i>in vivo</i> , <i>ex vivo</i>	No	60 %	30 %	40 %
RF ablation	FPI + FBG	<i>ex vivo</i>	Yes	30 %	20 %	60 %

\*<sup>1</sup> Medical sensors existing on the market and used by clinicians for medical examinations.

## CHAPTER 2: Optical Fibres, FBGs and FBG fabrication

### 2.1 OVERVIEW

This chapter focuses on optical fibres, their operational characteristics including waveguide modes related to different wavelengths. It also provides a detailed insight into light propagation through optical fibres and the resultant number of waveguide modes. It deeply discusses fibre Bragg gratings (FBGs), their classification, fabrication methods and the theory of their operation including their spectra.

### 2.2 OPTICAL FIBRE AND ITS PROPERTIES

An optical fibre is a light guiding structure which enables light to propagate from one end to the other end of the structure. The phenomenon of light propagation occurs due to its material and geometrical properties. An optical fibre's geometrical representation with cylindrical shape of layers is shown in Figure 2.1. These cylindrical layers are made of either glass or plastic material which has different dielectric properties that allow light propagation.

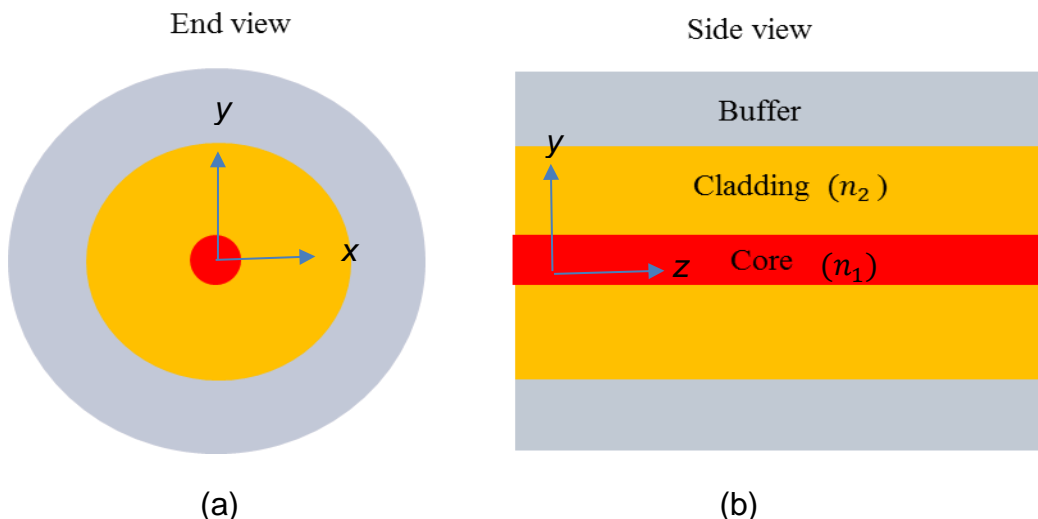


Figure 2.1: Schematic diagram of (a) end view and (b) side view of an optical fibre - *x*, *y* and *z* show the direction of axis of the fibre which is used throughout the study

The centre of an optical fibre is called the core and has higher refractive index ( $n_1$ ) than the cladding layer ( $n_2$ ). As a result, light is confined in the core area of the structure. When a light beam is incident on the fibre-air interface with

an angle  $\theta$ , as shown in Figure 2.2, it propagates through the structure as it experiences total internal reflection at the core-cladding interface.

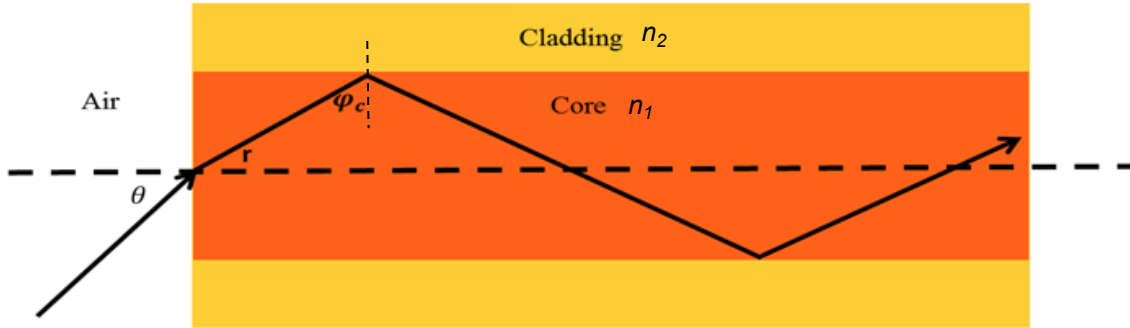


Figure 2.2: Schematic diagram of transmission of a light ray in an optical fibre

At the core-cladding interface the critical angle ( $\varphi_c$ ) is given by *Equation 2.1*.

$$\sin \varphi_c = \frac{n_2}{n_1} \quad \text{Equation 2.1}$$

The amount of light propagating through the structure depends on the light beam characteristics at the air-fibre interface, as not all rays will be coupled into a guided mode of the optical fibre. Therefore, it is necessary to determine the Numerical Aperture (NA), which measures the light gathering capacity.

At an air-fibre interface, if there is no surface irregularity and surface roughness, the NA is determined by the refractive indices difference between core and cladding areas, where the maximum value of  $\sin\theta$  for a ray to be guided, corresponding to  $\varphi_c$ , is given by the following equation:

$$\sin \theta_{max} = NA = \sqrt{n_1^2 - n_2^2} \quad \text{Equation 2.2}$$

The coupling efficiency of launching light into propagating modes in the fibre depends on the NA; the smaller the NA the smaller the acceptance angle. Hence, coupling with a small NA requires careful consideration of optical components and precise mechanical positioning and alignment of the optical fibre. In contrast, a larger NA has a larger acceptance angle which can be easily aligned with the fibre and it is more effective in light gathering. However, in situations where the incident angle is larger than  $\arcsin(NA)$ , the light is not guided through the core

properly and the loss of light will be high. This can be reduced by using lenses to ensure the light beam is directed into the acceptance cone of the fibre.

The transmission of light along the optical fibre can be explained by a set of Maxwell's equations in electromagnetic theory. These describe the behaviour of optical fibre including its properties such as absorption, attenuation and dispersion. The behaviour of a transmitted wave is described by modes which represent the distinct waveform transmitted through the fibre according to its geometrical structure, material properties and existing boundary conditions. Fibre modes can be categorized into two types: radiation modes and guided modes. Radiation modes carry energy out of the core and disappear while the guided modes carry energy and information along the fibre. The guided modes have particular mode profiles due to their electric (**E**) and magnetic (**H**) field configuration during the light propagation. Generally, there are two types of modes existing in planar and cylindrical waveguides. They are *TE* and *TM* modes, where **E** and **H** are zero along the propagation direction. In addition to those modes in cylindrical waveguides, hybrid modes (where **E** and **H** are non-zero in the direction of propagation) occur as a result of skew ray propagation. In telecommunication-grade optical fibres, the relative refractive index difference  $\Delta \sim 0.003$ , with

$$\Delta = \frac{n_1 - n_2}{n_1} \quad \text{Equation 2.3}$$

Therefore, it satisfies the weak guidance approximation where the relative refractive index difference  $\Delta \ll 1$  (Gloge, 1971). Under the weak guidance condition, longitudinal fields are very small compared to transverse components. Therefore, it is assumed that the fibre modes are transverse and linearly polarized in one direction, which is called a linearly polarized ( $LP_{lm}$ ) mode. The optical properties of  $LP_{lm}$  modes (Gloge, 1971) and its propagation constant can be obtained by solving eigenvalue equations (Snyder & Love, 2012). Figure 2.3 shows the electric field intensity profile with their electric field profile of the lowest four  $LP_{lm}$  modes (Ma, 2009; Poole et al., 1994).

Exact modes											
$HE_{11}$ even	$HE_{11}$ odd	$TE_{01}$	$HE_{21}$ even	$HE_{21}$ odd	$TM_{01}$	$HE_{31}$ even	$HE_{31}$ odd	$EH_{11}$ even	$EH_{11}$ odd	$HE_{12}$ even	$HE_{12}$ odd

$LP_{01}$		$LP_{11}$			$LP_{21}$		$LP_{02}$	
$E_x$	$E_y$	$E_x$	$E_y$	$E_x$	$E_y$	$E_x$	$E_y$	
		$\cos(k\varphi)$						

Figure 2.3: Electric field of lowest 12 modes of corresponding LP modes in step index fibre (Ma, 2009).

Depending on the number of modes guided through a particular fibre, it can be categorized into single mode or multimode. Single mode fibre supports one guided mode ( $HE_{11}$ ) whilst multimode has more than one mode. The number of modes guided through the structure depends on the operating wavelength ( $\lambda$ ), radius of the core ( $a$ ) and numerical aperture ( $NA$ ). If these parameters are known, the number of modes through the structure can be determined considering the normalized frequency  $V$ , which is defined by

$$V = \frac{2\pi a}{\lambda} NA \quad \text{Equation 2.4}$$

Figure 2.4 depicts the allowed guided modes by showing the normalized propagation constant ( $b$ ) which can be calculated by *Equation 2.5* and *Equation 2.6*, as a function of  $V$  in each case;

$$b = \frac{\bar{n} - n_2}{n_1 - n_2} \quad \text{Equation 2.5}$$

$$\bar{n} = \beta/k_0 \quad \text{Equation 2.6}$$

where  $\bar{n}$ ,  $\beta$  and  $k_0$  are the mode index, the propagation constant and the free space wave number, respectively.

According to Figure 2.4, only the  $HE_{11}$  mode exists for  $V < 2.4$  which is known as the fundamental mode of the fibre. In contrast, there are more modes for  $V > 2.4$  and those fibres are called multimode fibres.

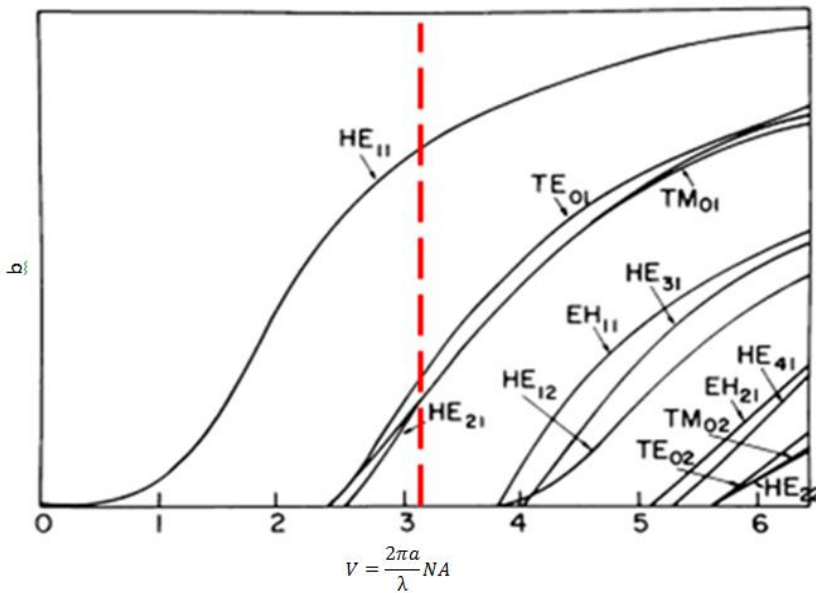


Figure 2.4: Normalized frequency ( $V$ ) Vs normalized propagation constant ( $b$ ) (Keck, 1981). The vertical line applies to  $(2/3)\lambda_B$  for SMF-28 fibre (assuming  $\lambda_B=1550$  nm).

Many types of fibres have been produced in various core and cladding diameters, from the range of nm to mm. Among them Corning SMF-28 is widely used around the world and all work in this thesis employs SMF-28. The properties of SMF-28 are listed in Table 2.1 and Table 2.2. Its behaviour is related to its  $V$  number as discussed using Figure 2.4.

Table 2.1: Properties of SMF-28 fibre

Single Mode Fibre, Corning SMF-28			
Coating diameter	$245 \pm 5 \mu\text{m}$	Numerical aperture	0.14
Cladding diameter	$125 \pm 1 \mu\text{m}$	Effective group index of refraction	1.4677 @ 1310 nm
Core diameter	$8.2 \mu\text{m}$	Effective group index of refraction	1.4682 @ 1550 nm
Core-clad concentricity	$\leq 0.5 \mu\text{m}$	Refractive index difference	0.36 %
Cladding non-circularity	$\leq 1 \%$	Mode field diameter @ 1310 nm	$9.2 \pm 0.4 \mu\text{m}$
Zero dispersion wavelength	1312 nm	Mode field diameter @ 1550 nm	$10.4 \pm 0.5 \mu\text{m}$

Source: [www.corning.com/opticalfiber](http://www.corning.com/opticalfiber)

*Table 2.2: Physical and material properties of SMF-28 (FEA simulation)*

Parameter	Symbol	Value
First strain-optic coefficient	$p_{11}$	0.121
Second strain-optic coefficient	$p_{12}$	0.270
Young's modulus	$E$	73.1GPa
Poisson's ratio	$\nu$	0.17
First stress-optic coefficient	$B_1$	$-0.65 \times 10^{-12} \text{ m}^2/\text{N}$
Second stress-optic coefficient	$B_2$	$-4.2 \times 10^{-12} \text{ m}^2/\text{N}$
Reference temperature	$T_{Ref}$	1000 °C
Room temperature	$T_R$	20 °C

## 2.3 FIBRE BRAGG GRATINGS

### 2.3.1 PHOTOSENSITIVITY

A Bragg grating is a result of a permanent periodic index of refraction modulation in the core area of an optical fibre due to UV exposure. This modulated index of refraction of the core depends on the wavelength and intensity of the light source and the properties of the optical fibre. The phenomenon of a permanent refractive index change is called photosensitivity. As noted in Section 1.3, it was first observed when 488 nm laser light was launched to an optical fibre core (Hill et al., 1993). Initially, it was believed photosensitivity occurred only for UV exposure on a fibre with high concentration of germanium dopants in the fibre core. Later photosensitivity was observed in fibres with different core dopants showing that this phenomenon is not solely dependent on germanium. Europium (Hill et al., 1991), cerium (Broer, Cone & Simpson, 1991) and erbium-germanium (Bilodeau et al., 1990) are also used as dopants instead of germanium. Although it is not the only material for photosensitivity, germanium-doped fibre is the most common material for fabricating devices utilizing photosensitivity. However, the mechanism of photosensitivity is not fully understood.

There are some theoretical explanations proposed, based on experimental and material arrangements that address the mechanism of photosensitivity. As photosensitivity depends on the wavelength and the intensity, it was suggested that the phenomenon is associated with a two photon mechanism which showed a strong periodic structure with square of light intensity (Lam & Garside, 1981). Later, Meltz, Morey & Glenn (1989) introduced a transverse writing technique which uses direct excitation at a wavelength of 240 nm and it was more

successful in FBG fabrication. The defect centres in germanosilicate glass are the cause of the absorption band occurring at the excitation wavelength of 240 nm (Hosono et al., 1992; Hosono, Kawazoe & Nishii, 1996; Nishii et al., 1995), which was explained by using the Kramers-Kronig relations (Russell et al., 1991). The concept of the photo-induced index changes due to a germanium oxygen vacancy defect in germanium doped fibre was changed after realizing that dopants other than germanium could exhibit photosensitivity. It appears that the mechanism of photosensitivity is a function of photochemical, photomechanical or thermochemical processes and depends on fibre type, wavelength and intensity (Othonos & Kyriacos, 1999).

Discovery and understanding of the photosensitivity mechanism was further established by improving the photosensitivity by up to two orders of magnitude by hydrogenation of fibre core prior to UV illumination (Atkins et al., 1993; Lemaire et al., 1993). Since then various methods have been reported to enhance the photosensitivity such as flame brushing, co-doping and staining. Among them, hydrogen loading has become a more common and popular method to enhance photosensitivity.

In hydrogen loading, hydrogen molecules diffuse into the fibre core when the fibre is soaked in hydrogen gas at 20 – 75 °C under pressure from ~ 20 to more than 750 atm (typically 150 atm). This treatment can increase the index of refraction by up to 0.01 permanently. In addition to fabricating FBGs in germanium silicate fibres, this method allows FBG inscription in germanium free fibres. Also, it helps to diffuse hydrogen out of unexposed fibre sections by minimizing (leaving negligible) absorption losses at the optical communication windows. FBGs treated with and without hydrogen confirm the mechanism of index change depends on the interaction between dopant and hydrogen molecules and UV exposure conditions (Lemaire et al., 1993). In hydrogen loaded fibres, temperature has significant impact on the growth of refractive index (Atkins et al., 1993).

Another method of enhancing photosensitivity is the flame brush technique which offers advantages compared to hydrogen loading, as the increase of photosensitivity is permanent. It can achieve this in 20 minutes through

repeatedly brushing a flame fuelled with hydrogen and a small amount of oxygen while reaching a temperature up to 1700 °C. However, the high temperature makes the fibre weaker and affects the long-term stability of the fibre. This method makes the core highly photosensitive by diffusing the hydrogen into the core very quickly and reacting with germanosilicate glass. In hydrogen loading, the hydrogen diffuses out and the fibre loses its photosensitivity. Compared to hydrogen loading, flame brushing can increase the photosensitivity of optical fibre by a factor greater than 10. However, both hydrogen loading, and flame brushing use the same techniques to enhance the photosensitivity. For this, they produce germanium oxygen deficient centres (GDOCs) as a result of a chemical reaction with hydrogen which is responsible for the photosensitivity.

As mentioned in the beginning of this Section, not only germanium but also europium (Hill et al., 1991), cerium (Broer, Cone & Simpson, 1991) and erbium-germanium (Bilodeau et al., 1990) exhibit photosensitivity; however, none of them shows photosensitivity strongly like germanium. Germanosilicate fibre has shown that it can have enhanced photosensitivity via additional various co-dopants. In particular, co-doping with boron has shown an increase of index change approximately 4 times larger compared to pure germanosilicate fibres (Williams et al., 1993). According to the experimental results, it was suggested that adding boron to the fibre doesn't enhance the photosensitivity by forming GDOCs as was the case for flame brushing and hydrogen loading. It is more likely due to the breaking of wrong bonds by UV light through photo-induced stress relaxation (Williams et al., 1993). Dianov et al. (1997) reported photosensitivity from germanosilicate fibre co-doped with nitrogen using a surface-plasma chemical-vapour deposition technique. They observed a larger photo induced refractive index change for nitrogen co-doped fibre treated with hydrogen loading compared to nitrogen free fibre. The resultant high photosensitivity in nitrogen doping is as a result of GDOCs formed in the glass.

### 2.3.2 CLASSIFICATION OF FIBRE BRAGG GRATINGS

There are many types of fibres and distinguishing them after FBG writing is a complex issue. Therefore, FBGs are categorized based on the photosensitivity and writing conditions such as continuous (CW) wave or pulsed wave, laser

power and wavelength. The following table shows the latest categorization of FBGs and their properties.

Table 2.3: Types of FBGs, their characteristics and properties ((Canning, 2008))

Grating type	Previous label (s)	Characteristics	Thermal resistance	Applications
<b>Type I</b>				
Type I	Type I	Simple grating writing in photosensitive doped fibres, mainly germanosilicate, including doped photonic crystal fibres [20]. Red shift in $\lambda_{\text{Bragg}}$ . Contributions from defect polarizability changes and structural change or densification. Latent sensitisation behaviour, crucial for grating growth, observed [21]. Stresses usually increase with irradiation – depends on fibre history	Stable to ~320 °C	Telecomm, sensing, bio-diagnostics, lasers
Type In	Type IIa, negative index gratings	Characteristic curve usually onsets after type I grating growth rolls over. Onset determined by fibre drawing history, composition, presence of H <sub>2</sub> , optical intensity, applied stresses and hypersensitisation of stresses [22]. Density change taken over by dilation. Blue shift in $\lambda_{\text{Bragg}}$ , or no shift, usually observed. Under continued exposure at high intensities, increased strains despite equilibration, can lead to eventual fracturing and type IH-like damage	In GeO <sub>2</sub> doped fibres, stable between 500-800 °C, depending on preparation and length required duration	High temperature, sensing, lasers
Type IH	Type I (H <sub>2</sub> )	Superficially similar to type I gratings but significantly enhanced index change in the presence of H <sub>2</sub> , large red shift in $\lambda_{\text{Bragg}}$ . Formed defect and hydrogen species give rise to polarizability changes which accounts for bulk of index change. Formation of OH at high temperatures enhances photosensitivity [23]. Stress increase of type I gratings is mitigated by OH dilation and through hydrogen bonding within the network.	< 320 °C for GeO <sub>2</sub> doped optical fibres, improved in non-germanosilicate fibres and when using shorter writing wavelength (e.g. 193 nm).	Telecomm, sensing, bio-diagnostics, lasers (most commonly used gratings)
Type IH <sub>p</sub>	Type Ia	With continued exposure bulk index change keeps rising although index modulation is overall small. Very large red shift in $\lambda_{\text{Bragg}}$ (> 10 nm, > 10 <sup>-2</sup> index change is possible). Similar properties to type In gratings suggests anisotropic stress equilibration through anisotropic OH formation occurs [25].	Up to 500 °C in GeO <sub>2</sub> doped fibre	Sensing, lasers

Type II <sup>hs</sup>	Hypersensitised	When initial seed exposure (either laser, thermal, or solar) is used to lock in the initial sensitisation phase of H <sub>2</sub> loaded fibres superior grating performances and more linear characteristic curves can be obtained [26-32]. Type In gratings possible in H <sub>2</sub> hypersensitised fibre [24].	No post-annealing required. Up to 500 °C stability, possibly more depending on host and preparation. In P <sub>2</sub> O <sub>3</sub> doped fibres useful operation up to 600°C obtained.	Telecomm, complex devices, long term temperature sensing, lasers (especially optimising gain), industrial fabrication based on linearised grating growth
Type I <sup>d</sup>	Densification gratings	Usually written just below the damage threshold of the glass. Enabled grating writing in single-material structured optical fibres [17], as well as the first DBR and DFB photonic crystal fibre lasers with no GeO <sub>2</sub> but instead Al <sub>2</sub> O <sub>3</sub> in the core [33-35]	Varies depending on the host composition and host thermal history. Can exceed 300-400 °C.	Sensing, lasers, structured fibre devices
<b>Type II</b>				
Type II	Type II, damage gratings	Gratings produced with intensity exceeding damage threshold of the glass leading to fracturing, void formation and/or filamentation. Using ultra short pulses with high peak intensity cascade ionisation and plasma generation and expand the events involved with change. Femtosecond gratings recently shown to fall into this category [36].	> 1000 °C [37] independent of host.	Moderate to high power fibre laser operation depending on dopant, ultra-high temperature sensing
<b>Regenerated gratings</b>				
Type R	Regenerated gratings	Gratings produced after annealing out type I gratings, usually regenerated at temperatures > 500 °C. Very new configuration with significant potential for optimisation. Similarities with type II gratings although reflectivities are weak and therefore comparable losses and scattering not observed. Can be repeatedly cycled to very high temperatures with no degradation.	> 1000 °C stability is related to softening point of core glass [47].	Ultra-stable grating operation, sensing or lasers

## 2.4 THEORY OF FIBRE BRAGG GRATINGS

As shown in Figure 2.5, the simplest Bragg grating is a periodic modulation of the refractive index along the core in a single mode fibre. These gratings are called uniform gratings due to their constant periodic planes which are perpendicular to the direction of light propagation. At each grating plane a fraction of propagating light scatters and as a result, the scattered light could transmit or reflect at grating planes. If the reflected rays are out of phase, they cancel each other due to destructive interference. When the reflected light rays from each grating plane are in phase, the reflected wave constructively interferes and back-reflects satisfying the Bragg condition. To satisfy the Bragg condition, requires both energy and momentum conservation. Energy conservation is given by the same amount of incident and reflected radiation as follows:

$$\hbar\omega_f = \hbar\omega_i \quad \text{Equation 2.7}$$

where  $\hbar$  is Planck's constant ( $\hbar = h/2\pi$ ) and  $\omega$  is angular frequency ( $= 2\pi f$ )

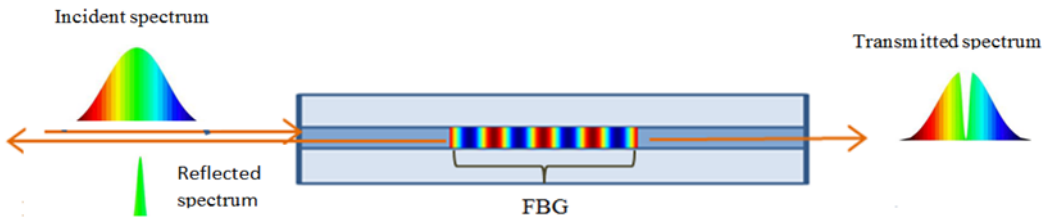


Figure 2.5: Transmission and reflection spectra due to FBG

Momentum conservation is given by the combination of incident ( $\mathbf{k}_i$ ) and grating wave vector ( $\mathbf{K}$ ) which is equal to that of the scattered radiation ( $\mathbf{k}_f$ ), as follows:

$$\mathbf{k}_i + \mathbf{K} = \mathbf{k}_f \quad \text{Equation 2.8}$$

The diffracted wave vector has an equal and opposite sign to the magnitude of the incident wave vector, and the direction of the wave vector  $\mathbf{K}$  is normal to the grating planes with a magnitude of  $2\pi/\lambda$ ; hence, *Equation 2.8* changes to *Equation 2.9*

$$2 \left( \frac{2\pi n_{eff}}{\lambda_m} \right) = \frac{2\pi}{\Lambda} \quad \text{Equation 2.9}$$

Rearranging of *Equation 2.9* is given by *Equation 2.10*:

$$\lambda_m = \frac{2n_{eff} \Lambda}{m} \quad \text{Equation 2.10}$$

where  $\lambda_m$  is the reflected wavelength of order  $m = 1, 2, 3, \dots$ ,  $\Lambda$  is the grating period ( $\Lambda_{pm}/2$ ) and  $n_{eff}$  is the effective mode index of the fibre. For a single mode fibre, the only mode propagating is  $LP_{01}$ . When  $m = 1$ , therefore, the equation above (Equation 2.10) becomes Equation 2.11.

$$\lambda_B = 2n_{eff}\Lambda \quad \text{Equation 2.11}$$

$\lambda_B$  is well known as the Bragg wavelength which relies on the main reflection of the gratings and the resulting condition is called the first order Bragg condition.

#### 2.4.1 FBG FABRICATION METHODS

There are number of FBG fabrication methods that have been reported for standard and complex gratings in optical fibres since 1978 (Hill, 2000): Bulk interferometer (Meltz, Morey & Glenn, 1989), the phase mask method (Hill et al., 1993), point by point writing (Malo et al., 1993), the Lloyd mirror interferometer (Limberger et al., 1993) and prism interferometer (Kashyap et al., 1990) are the best known. Among them, interferometric methods and phase mask methods have become more popular than others. The interferometric method uses a beam splitter to split the single UV beam and allow these beams to interfere at the fibre as shown in Figure 2.6 (a), while the phase mask method uses a continuous or pulsed source on a periodic phase mask (diffraction grating) to expose UV light as a periodic pattern on the optical fibre to fabricate FBG, as shown in Figure 2.6 (b).

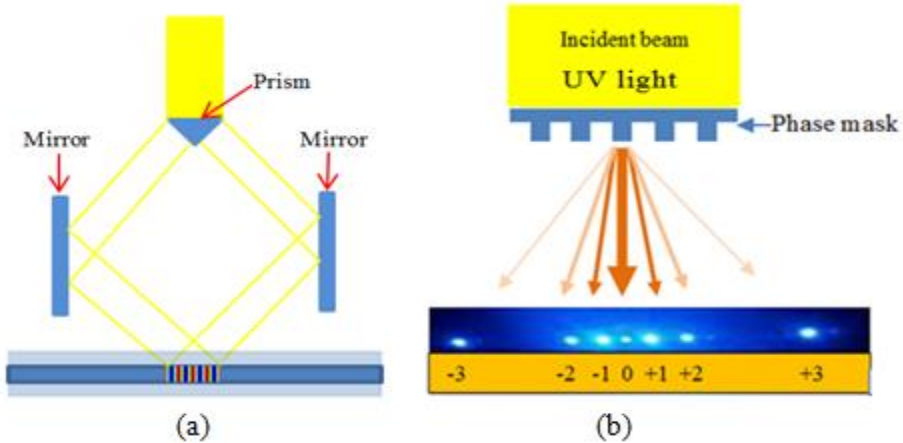


Figure 2.6: Optical system for interferometric inscription of FBGs (a) transverse holographic method and (b) phase mask method

In this thesis, the focus is FBG writing using a periodic phase mask in accordance with manufacturing details, as it is the most common method of FBG fabrication (and the assumed fabrication method for FBGs considered in this work). As shown in Figure 2.6 (b), the phase mask consists of lines and spaces, which are called diffractive gratings, arranged in a periodic manner. The periodic line and space (grating) is defined based on the FBG pattern which will be created in the silica fibre. When the UV light is incident on the phase mask, at each slit, the light is diffracted and forms an interference pattern as it is composed of an infinite number of gratings. As a result, it induces a periodic modulation of refractive index in the core area of photosensitive fibres, which is called a Bragg grating.

The history of diffraction gratings expands long back to 1785 when American astronomer David Rittenhouse explained diffraction of light using a simple grating having strung hairs between very fine screws of brass (Loewen & Popov, 1997). In the early years, gratings were produced manually by scratching a blank substrate using a ruler. However that method was not popular as it was very expensive, time consuming and also had poor resolution of a power spectrum of low intensity (Harrison, 1949). However, it only became practical from the early stage of 1800's with the reinvention of diffraction grating using grating ruling engine by Joseph von Fraunhofer. He later discovered the absorption lines in the solar spectrum using fine gratings which are now known as Fraunhofer lines. Demand for the gratings so produced was increased due to the use of spectroscopy. Some of those problems were mentioned, addressed by the grating ruled engine designed by incorporating temperature control and kinematic

isolation by Henry A. Rowland (1848-1901), who is known as the “father of modern diffraction grating”, and his successor at Johns Hopkins University. Their ruling engines produced most of the gratings (up to 7.5 inches (19.05 cm) in length) needed for the scientific community for nearly 50 years (Harrison, 1949). Then Michelson (1852-1930), was successful in producing larger gratings (10 inches) and improved resolution than Rowland’s. Most of the grating ruling engines’ problems such as error in the ruling motion and resolution were solved by Harrison and his team as their engine was equipped with interferometric position feedback control. It has become the standard practice in modern ruling engines since 1955 (Harrison & Loewen, 1976).

Although precise gratings were produced successfully there were number of obstacles of using grating ruling process. It was very time consuming due to its slow process (i.e. takes months to complete the gratings) and consequently it became more expensive. The lifetime of the tools of ruling engine left some doubts about the possibility of using them for lengthy writing procedures. The mechanical engine ruling process was also required environmental and vibration isolation (Loewen & Popov, 1997). Production of reflection gratings by the use of ruling engines was not successful due to the failure to produce high efficiency transmission gratings.

The concept of lithographic methods for gratings fabrications by Michelson has opened a new era for the fabrication industry. Today his Interference Lithography (IL) method is a widespread tool for grating fabrication. In the IL method, two coherent beams of light interfere in photoresist and produce fringe patterns consisting of high and low intensities of light, as shown in Figure 2.7.

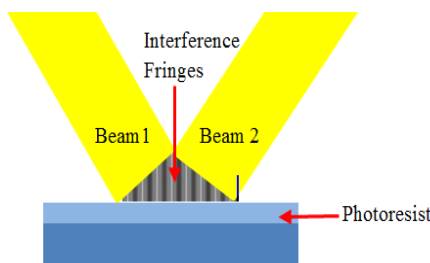


*Figure 2.7: Optical system for Interference Lithographic method*

These fringes turn into grating lines after wet development. Then this grating line structure is transferred into a substrate permanently by a chemical process called

chemical etching. The process of IL was later improved with the development of lasers and high-quality resist. There are number of advantages of using this new technique. The fabrication process is very fast compared to the ruling method and produces all the grooves simultaneously in a single exposure. It improves the quality of the groove profile; hence, it increases the performance with high diffraction efficiency. As it uses light for fabrication, the system becomes static. Therefore, there are no spectral defects and environmental issues as reported in the ruling method. It has become a more powerful tool for fabrication as well as more economical as it has been used in conjunction with semiconductor technology over the past decades. Today, the combination of semiconductor technology, etching technology and holographic technology are capable of producing high quality and high efficiency transmission gratings.

This study has used the fabrication of FBG pattern using fused silica transmission gratings. Two methods are used to fabricate the fused silica in the manufacturing process:

1. Grating patterning in photoresist: Two methods can be used to patterning gratings in photoresist: conventional holographic method and holographic stepper method. The conventional holographic method uses two coherent collimated light beams that interfere at the photoresist area which is on a fused silica substrate. With the light exposure, the grating profile is developed in a photoresist (polymer), as shown in Figure 2.8. The other method is a combination of holographic method with semiconductor technology which is capable of producing high quality gratings with low production cost. The advantage of this method is the use of a semiconductor material instead of polymer materials, which are more stable.

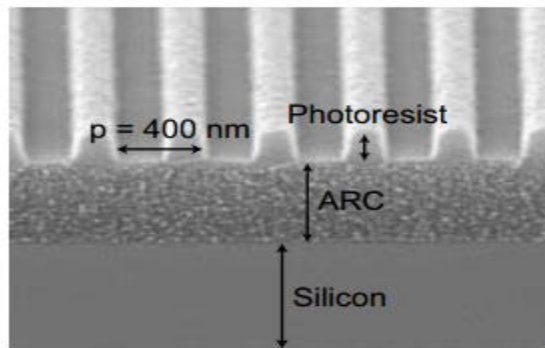


*Figure 2.8: Image of 400 nm grating in photoresist Transfer the photoresist grating pattern into substrate (fused silica) - (Chen & Schattenburg, 2004)*

2. Transfer the photoresist grating pattern into substrate (fused silica) - In this method, the grating pattern is produced by means of available methods to produce a grating pattern as described above. The produced grating pattern is then transferred into bulk fused silica, as shown in Figure 2.9, by semiconductor etching technology. The advantages of using fused silica as the substrate are due to its very low absorption of light, dielectric property and the ability to use it in harsh environmental conditions.

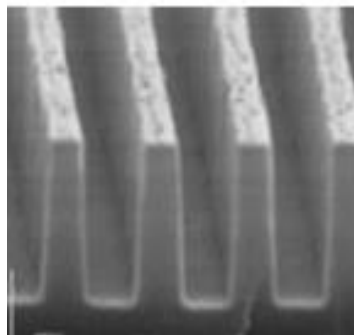


*Figure 2.9: Image of Scanning Electron Microscopy of 400 nm grating in fused silica (Buchwald, 2007)*

#### 2.4.2 THEORY OF FBG FABRICATION TECHNIQUE BY A PHASE MASK

As shown in Figure 2.9, the phase mask is a one-dimensional (1-D) array of a periodic-relief pattern of period  $\lambda_{pm}$  which is etched into fused silica. In the manufacturing process, it is designed to suppressed the zeroth and higher orders, except  $\pm 1$  orders, while maximizing these in order to produce standard FBGs with grating period  $\lambda_{pm}/2$ . Figure 2.10 shows the arrangement of a phase mask to produce a first order diffraction pattern and its fringe patterns on optical fibres at normal incidence. Figure 2.10 (a) shows a standard FBG produced by

interference of  $\pm 1$  orders while Figure 2.10 (b) shows a FBG formed by interference of number of diffraction orders including  $\pm 1$  orders.

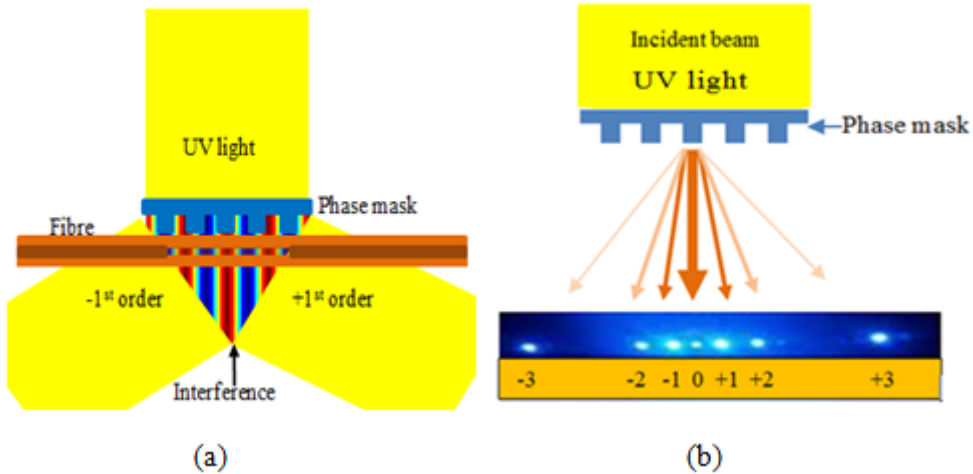


Figure 2.10: FBG writing method using phase mask (a) Interference of first order diffraction behind phase mask by forming a uniform grating structure (b) Interference of higher orders diffractions including zeroth order by forming a complex FBG structure

#### 2.4.3 INDUCED BRAGG PERIOD, INDEX OF REFRACTION CHANGE AND REFLECTANCE

As this project considers only FBG fabricated using the phase mask technique, the essential features of the technique will be presented. A uniform or ideal grating as shown in Figure 2.5 is a result of the interference of  $\pm 1$  order diffracted beams of an ideal phase mask. In uniform gratings, the grating period becomes  $\Lambda$  which is half of the phase mask period ( $\Lambda_{pm}$ ). However, if FBGs were fabricated using multiple phase mask orders, the grating structure becomes complex, as further discussed in the next section.

A Bragg grating is a periodic refractive index change in the core of the optical fibre. In a uniform grating (Figure 2.5), the induced index change is periodic. If the core index of refraction is  $n_{co}$ , the refractive index profile of FBG can be expressed by *Equation 2.12*.

$$n(z) = n_{co} + \Delta n \left( 1 + \cos \left( \frac{2\pi z}{\Lambda} \right) \right) \quad \text{Equation 2.12}$$

Where  $\Delta n$  and  $z$  is the amplitude of the average perturbation of refractive index and distance along the fibre longitudinal axis, respectively. The uniform periodic index change relates to *Equation 2.12*, and is illustrated in Figure 2.11.

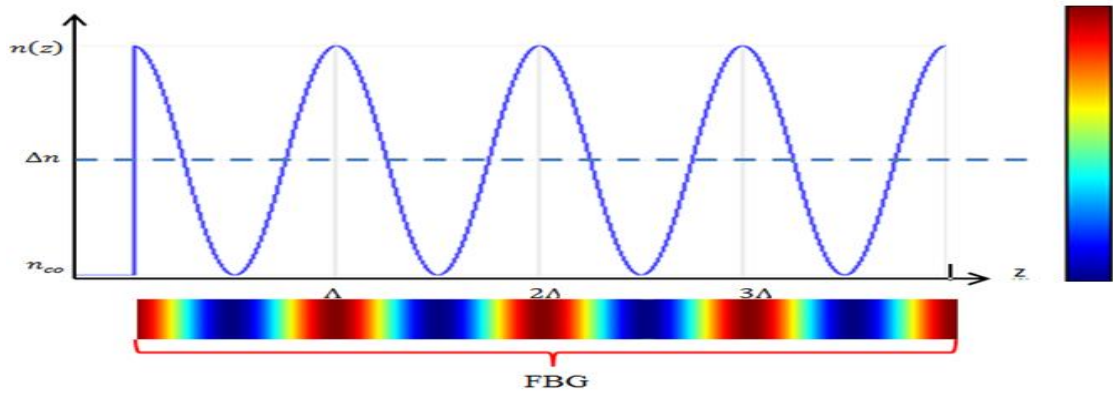


*Figure 2.11: The induced index changes along the longitudinal axis of fibre core to a FBG - the colour spectrum shows variation of index change in FBG region*

#### 2.4.4 GRATING FORMATION WITH MULTIPLE PHASE MASK ORDERS

The ideal phase mask is designed to produce uniform FBGs patterns suppressing zeroth order diffraction and maximizing first order diffraction. As already noted the zeroth order is not fully suppressed; a few percent (3%) transmits while each of the first orders has nearly 35% of total transmitted power. Therefore, the resultant FBG pattern is not purely uniform as it results from the superposition of multiple interference patterns. Various studies have been conducted experimentally and numerically to investigate the contribution of other orders in addition to the first orders. Dragomir et al. (2003) used Differential Interference Contrast (DIC) microscopy to obtain non-destructive images of Type I FBG fabricated using the phase mask method. These images confirmed the formation of a complex structure that is due to the interference of various diffraction orders. These results are depicted in Figure 2.12 and Figure 2.13 in which Dragomir (2004) and Rollinson et al. (2005) reported DIC images of FBGs.

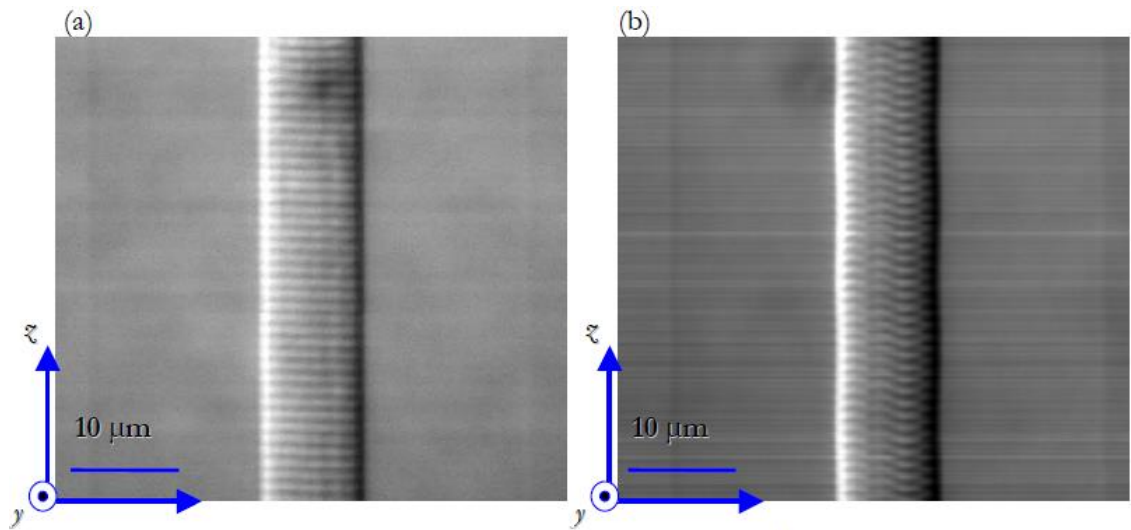


Figure 2.12: DIC images of the fibre core containing Bragg grating, recorded for two different fibre orientation (a) the images was taken from a direction parallel to the writing UV laser beam and (b) after rotating 90 degrees from (a) (Dragomir, 2004)

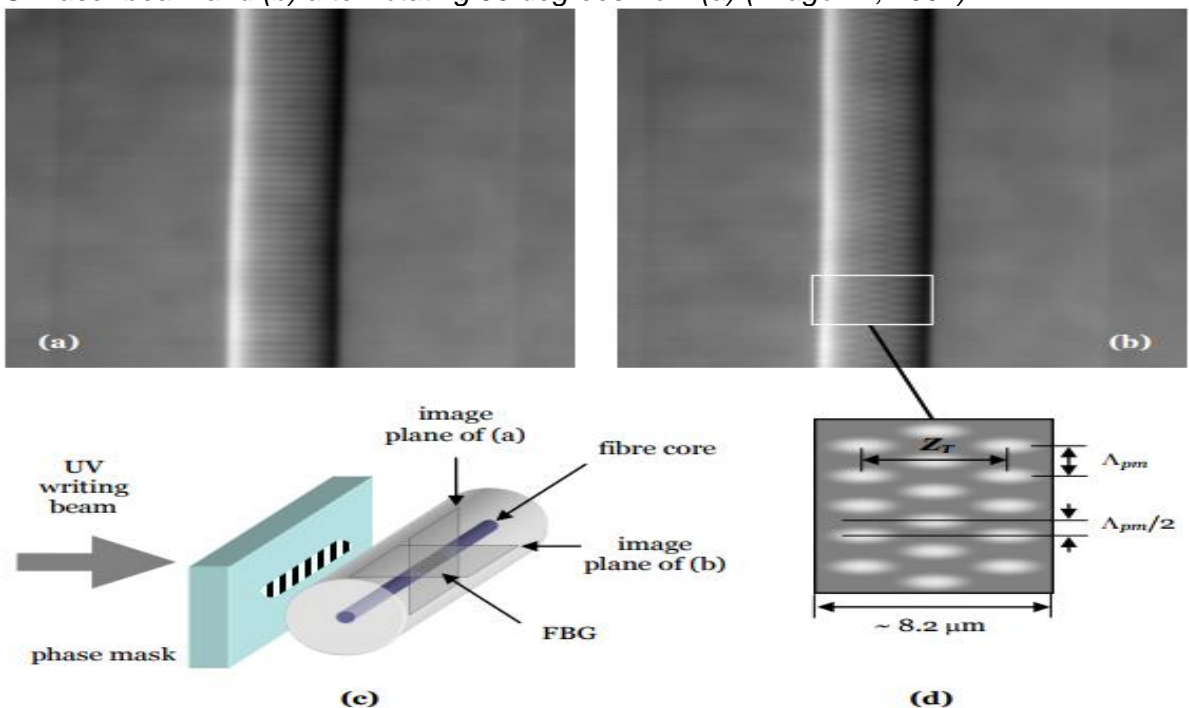
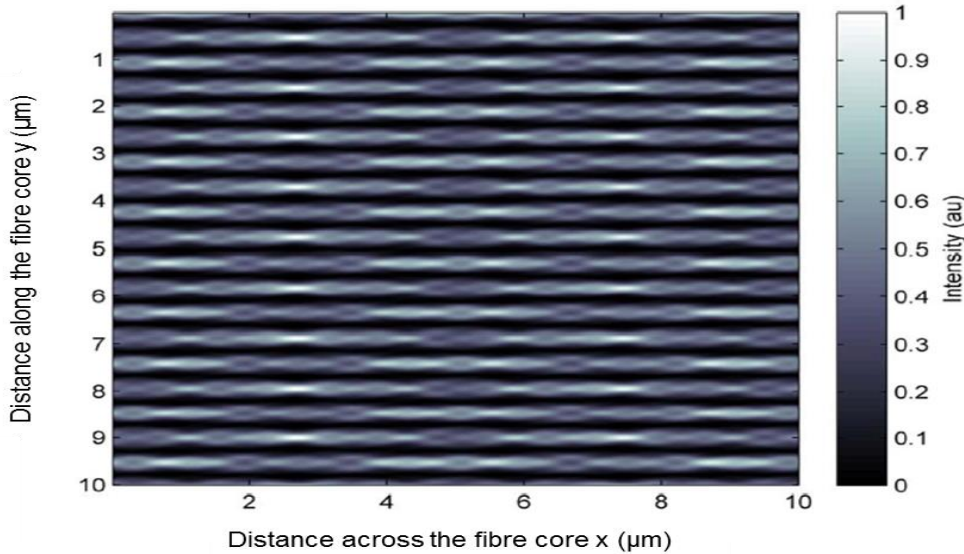


Figure 2.13: DIC microscopy images of FBG in core region of Type 1 fibre at different orientation to the writing beam (a) Images of fibre orientation is perpendicular to the writing beam (b) Images of fibre orientation is parallel to the writing beam (c) schematic diagram of writing technique and image planes orientation to the writing beam (d) Schematic diagram of (b) showing the interleaving planes belongs to index modulation of  $\Delta_{pm}$  and  $\Delta_{pm}/2$ ;  $Z_T$  is Talbot length (Rollinson, 2012)

Although it is said that the zeroth and higher order are suppressed to maximize the first orders it is impractical to eliminate them entirely in the manufacturing process. Generally the phase masks for FBG fabrication manufactured with zeroth order transmit less than 3% of the diffracted waves, while first orders

transmit more than 35% each and the rest of the transmission is via the other possible higher orders (Othonos & Kyriacos, 1999). The possibilities of fringe formation by other orders except  $\pm 1$  orders have resulted in concern about how fabrication processes could impact on spectral properties. Investigation of the real structure of FBG patterns have been reported via various approaches such as: numerical analysis (Dyer, Farley & Giedl, 1995; Kouskousis et al., 2013; Mills et al., 2000; Tarnowski & Urbanczyk, 2013), experimental analysis (Rollinson et al., 2005) and microscopic analysis (Dragomir et al., 2003; Goh et al., 2014; Kouskousis, 2009; Yam et al., 2009). These analyses show how the existence of a complex FBG structure is as a result of the contribution of multiple orders and their interference. Figure 2.14 shows the modelled refractive index variation in the fibre core obtained by Kouskousis et al. (2013) considering interference of  $0 - \pm 4^{\text{th}}$  orders. According to these analyses, it was observed and confirmed that the complex structure includes multiple periodic structures at certain distances from the phase mask which is due to the Talbot effect (discussed in the subsequent paragraph). Although the existence of complex FBG structures and how these relate to the resultant spectrum has been considered, there is need for more extensive modelling to improve our understanding.



*Figure 2.14: Modelled intensity variation in the core area of the fibre due to contribution of multiple diffraction orders from phase mask fabrication (Kouskousis et al., 2013)*

As shown in Figure 2.13 (b), the complex structure contains replicates of structures at multiples of defined distances from the phase mask due to the Talbot effect, which was discovered by Talbot in 1836. This effect has also been

observed in atom optics. As a result of the fundamental Fresnel diffraction effect, it has gained a great attention over wide range of applications such as real time data acquisition, generation of ultra-high speed tuneable pulse source, determination of dispersion parameters of optical fibre links and a number of spectroscopic techniques (Chavel & Strand, 1984; Chen & Azana, 2005; Guigay et al., 2004; Liu, 1988a, 1988b; Mehta et al., 2006). As a result of near field diffraction and when a plane wave transmits through periodic structure, the resultant wave-front replicates the periodic structure at a certain distance. That distance is called the Talbot length (Talbot, 1836). The phenomenon of a self-imaging distance was first defined in theoretically by Rayleigh (1881) as given by:

$$Z_T = \frac{\lambda}{1 - \sqrt{1 - \lambda^2/\Lambda_{pm}^2}} \quad \text{Equation 2.13}$$

Later he simplified *Equation 2.13* considering the relation between  $\Lambda_{pm}$  and  $\lambda$  (when wavelength is considerably small); the result was *Equation 2.14* as given below:

$$Z_T = \frac{2\Lambda_{pm}^2}{\lambda} \quad \text{Equation 2.14}$$

Measurement of the Talbot length using the equation above became popular and position of Talbot planes were calculated using Fresnel-Kirchhoff diffraction and Fourier optics. However, the difficulty of measuring all Talbot planes became a disadvantage of this methodology. That was overcome by Latimer (Latimer, 1993a, 1993b, 1993c) by introducing these patterns as a multiple-slit diffraction pattern produced by conventional mechanism instead of Fourier images of the gratings.

Investigation of the Talbot effect has been further established with finite element analysis and scalar theory analysis of Fresnel-diffraction. Those analyses provide the information of the amplitude and phase. The experiments and simulation were performed to investigate the effect of exposure condition of laser confirming the deviation of the expected grating structure due to the contribution of other orders (Dyer, Farley & Giedl, 1995). Direct imaging of Talbot patterns using tapered optical fibre to the tip by Mills et al, who first used an imaging technique, has

further confirmed the theoretical models based on diffraction theory (Mills et al., 2000). They also explained the reason to have repeated lengths is a result of the interaction of individual diffraction orders. Mills' further work on scanning the intensity pattern along the optical fibre produced results that were compatible with X-ray diffraction theory, which is used to describe the electric pattern field behind the phase mask. According to his explanation, the Talbot length has been simplified, as in *Equation 2.15*, when the numbers of diffraction orders are small:

$$Z_T = \frac{2\pi}{[(k^2 - m^2 G^2)^{1/2} - (k^2 - n^2 G^2)]} \quad \text{Equation 2.15}$$

where  $m$  and  $n$  are integers representing the diffraction orders  $m < n$ , and  $G$  is the unit reciprocal lattice vector which can be calculated using  $2\pi/\Lambda_{pm}$  of the phase mask with periodicity  $\Lambda_{pm}$ .

#### 2.4.5 INDUCED REFLECTANCE AND SPECTRAL CHARACTERISTICS

The reflectivity of a grating which has constant modulation amplitude and period was explained using coupled mode theory by Lam and Garside (1981). Using coupled mode theory, which is more popular for describing the behaviour of Bragg gratings, they obtained quantitative information about the spectral dependence and diffraction efficiencies of FBGs. Therefore, the reflectivity of a uniform Bragg grating can be expressed by

$$R(l, \lambda) = \frac{\Omega^2 \sinh^2(sl)}{\Delta k^2 \sinh^2(sl) + s^2 \cosh^2(sl)} \quad \text{Equation 2.16}$$

where  $R(l, \lambda)$  is the reflectivity of a Bragg grating which is a function of wavelength  $\lambda$  and grating length  $l$ .  $\Delta k$  and  $k$  are the detuning wave vector and propagation constant, which are given by  $k - \pi/\lambda$  and  $2\pi n_0/\lambda$  respectively.  $\Omega$  is the coupling coefficient and is given by *Equation 2.17*:

$$\Omega = \frac{\pi \Delta n}{\lambda} M_p \quad \text{Equation 2.17}$$

where  $M_p$  is the power confinement factor of the fibre core and it is expressed as:

$$M_p = 1 - V^{-2} \quad \text{Equation 2.18}$$

where  $V$  is the normalized frequency of the fibre as given by Equation 2.4. ‘ $s$ ’ can be obtained by the following equation as  $\Omega$  and  $\Delta k$  are already known:

$$s^2 = \Omega^2 - \Delta k^2 \quad \text{Equation 2.19}$$

At the Bragg wavelength,  $\Delta k$  becomes zero. Therefore *Equation 2.16* can be written as

$$R(l, \lambda) = \tanh^2(\Omega l) \quad \text{Equation 2.20}$$

where  $l$  is the length of FBG which was inscribed in an optical fibre as previously shown in Figure 2.5.

As the reflectivity is a function of grating length, an increase of the grating length increases the reflectivity. Reflectivity is also dependent on the coupling constant. Therefore, an increase of the induced index change increases the reflectivity. When broadband light propagates through the fibre having a uniform FBG, the resultant reflection peak or transmission dip is observed at the same  $\lambda$ , as shown by Figure 2.15 (a), and Figure 2.15 (b), respectively.

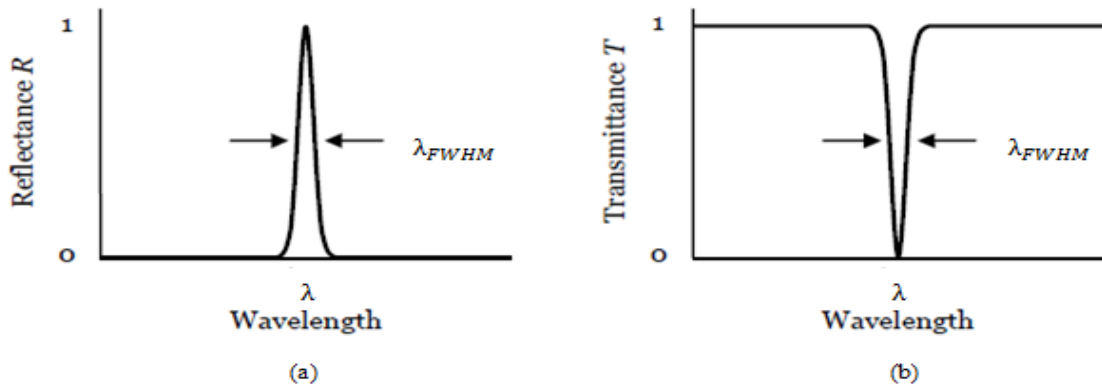


*Figure 2.15: Reflection (a) and transmission (b) of uniform Bragg grating*

At half of the maximum of reflectance or transmittance, the grating spectral width is defined as the Full Width at of Half Maximum ( $\lambda_{FWHM}$ ), and can be calculated using (Othonos & Kyriacos, 1999).

$$\lambda_{FWHM} = \lambda_B s \sqrt{\left(\frac{\Delta n}{2n_{eff}}\right)^2 + \left(\frac{1}{N}\right)^2} \quad \text{Equation 2.21}$$

where  $\lambda_B$ ,  $\Delta n$ ,  $n_{eff}$  and  $N (= L_{FBG} / \Lambda)$  are the Bragg wavelength, amplitude of the induced RI of the fibre, effective mode index and number of grating planes respectively.  $s$  is 1 for strong grating with reflectivity close to 100% and 0.5 for weaker gratings. Here  $s$  is assumed as 1 for simulations.

Therefore, in single mode operation where  $V < 2.405$  there is only one reflection peak expected. However, the observations of more reflection peaks other than the expected peak have been reported. In 1993, it was first reported by Xie et al. (1993) and they reported the second order reflection at  $(1/2)\lambda_B$  together with first order reflection from fibre Bragg gratings written in germanosilicate fibres doped with various dopants. It was suggested that the second order reflection is a result of a saturation effect. In 1997, the second order Bragg reflection at  $(2/3)\lambda_B$  and the other reflections at shorter wavelengths were reported by Hill & Meltz (1997). Due to saturation effects, the refractive index variation along the core flattened with time of pulse exposure by changing the sinusoidal variation. The sharper transmission dips at wavelengths of 1535, 1030, 770 and 629 nm produced using a phase mask of grating period  $1.06 \mu\text{m}$  were observed and reported by (Malo et al., 1993), providing compelling evidence to the existence of other harmonics. As the phase masks are designed to maximize the first order diffraction by inscribing the FBG planes with half of the phase mask period, the authors suggested that the extra reflections are the result of photo imprinted grating with a period of the phase mask. The microscopic images of Type II gratings showed that the gratings with period equal to the phase mask period is in good agreement with the above suggestion (Rollinson, 2012). Smelser, Grobnic & Mihailov (2004) analysed the interference pattern formed by a phase mask of grating period  $3.212 \mu\text{m}$  using a pulsed IR source. The resultant spectrum showed the spatial separation of first orders from the zeroth and second orders is 1.3 mm, further evidence to the existence of other harmonics orders. Yam et al. (2008) also observed the growth of a number of peaks at  $(2/3)\lambda_B$  as a function of time using a chirped FBG. He also suggested that the resultant peak at  $(2/3)\lambda_B$  is due to properties of phase mask. Rollinson (2012) also reported the existence of other harmonics according to the results obtained for an experiment conducted using Type I and II gratings which were written using the phase mask technique. She investigated the various FBGs inscribed in different fibre types under different writing condition using the

phase mask method. The results also showed how the phase mask properties result in more harmonics than expected.

## 2.5 SUMMARY

The main purpose of this chapter was to introduce optical fibre, FBGs and their characteristics. It discussed the requirements for light propagation in a single mode fibre and demonstrated a number of modes could arise for propagating light due to normalized frequency value, behaving as a multimode or single mode fibre. Furthermore, it discussed FBG structures, their spectral characteristics and the formation of FBGs in an optical fibre due to the photosensitivity effect. It then described the history of the formation and evolution of the concept of FBGs. The chapter then described newer classifications of fibre Bragg gratings due to their thermal resistance and characteristics compared to older classifications. This was followed by a discussion of the theory of fibre Bragg gratings, the Talbot effect and FBG spectra in detail using proper equations. Finally, an extensive review was given to literature findings of complex grating considering the experimental evidence and analytical data obtained.

The theoretical and experimental description in this chapter inform the modelling of complex FBG structure using phase mask method in single mode fibre SMF-28 in Chapter 4 and further investigate the Bragg grating periods, number of harmonics and their strength, saturation effect and resultant spectra at different wavelengths.

## **CHAPTER 3: Pressure measurement using FBGs**

### **3.1 OVERVIEW**

The main focus in this chapter is the use of FBGs as pressure sensors describing those reported to date and their limitations. The various ways in which pressure may be exerted on an optical fibre such as uniform pressure and transverse compressive load, is discussed. It also provides a detailed literature review into the cause of non-linear behaviour in such sensors due to birefringence effects and the effect of material properties on pressure sensitivity. It explains in detail the sensitivity measurement techniques with the help of the appropriate equations which lead to FEA modelling in Chapter 5.

### **3.2 FIBRE BRAGG GRATING PRESSURE SENSORS**

Pressure can be exerted on a FBG as a uniform pressure, or via transverse compressive load, longitudinal tensile force or longitudinal compressive force. Pressure sensing can be mainly categorized into direct sensing using a bare FBG, and indirect sensing by embedding the FBG into a suitable material (Xu et al., 1993; Yunqi et al., 2000). Many methods have been investigated to improve pressure sensitivity. Additionally, mechanical amplifiers have been introduced using force summing devices including a glass bubble house (Xu, Geiger & Dakin, 1996) and a piston-based system (Correia et al., 2010). In a piston-based system, the applied load transfers the load onto the fibre as an axial strain that changes the properties of the FBG, which is well known, as strain or load sensors have been investigated extensively (Hill & Meltz, 1997). In contrast, Zhong et al. (2015) demonstrated an inflated long period fibre grating inscribed in a pure-silica Photonic Crystal fibre (PCF) for high sensitivity gas pressure sensing applications. They identified the method used is a way to a promising gas pressure sensor in which the achieved pressure measurement range was up to 10MPa.

Table 3.1 summarizes the pressure sensitivity of FBG-based sensors on bare or polymer coated fibres and mechanical or force multipliers reported by various authors, expressed as nm of Bragg wavelength shift per MPa, for the indicated

ranges. The cause of sensitivity variation in Table 3.1 is further discussed in upcoming sections.

*Table 3.1: Summary of FBG-based pressure sensors, in order of pressure sensitivity for bare/polymer coated/mechanical/force multipliers*

FBG Type/Novelty		Sensitivity  nm/MPa	Range (MPa)	Authors
<b>Bare/Polymer coated</b>	Standard/bare	0.003	0 - 70	(Xu et al., 1993)
	Polymer coated/temperature and pressure	0.08	0 - 10	(Liu et al., 2000)
	Polymer coated/aluminium cylinder	5.28	0 - 0.44	(Zhang et al., 2001)
	Polymer coated/copper cylinder	4.09	0 - 0.44	(Liu et al., 2007)
	Standard/polymer filled casing	8.7	0 - 0.276	(Ahmad et al., 2008)
	Long period grating	0.051	0 - 0.1	(Bock et al., 2007)
	Photonic crystal fibre	2.65	0 - 0.6	(Yan, Ferraris & Reynaerts, 2011)
	Photonic crystal fibre	9.08	0 - 0.1	(Yan et al., 2010)
<b>Mechanical/ Force Multipliers</b>	Standard/bare/integrated diaphragm	0.001-0.003	0 - 70	(Allwood et al., 2015; Huang et al., 2014; Pachava et al., 2014; Vorathin et al., 2018b; Zhao et al., 2018)
	Polymer coated/temperature and pressure	0.08-0.75	0 - 10	(Bhowmik et al., 2015)
	Polymer coated/aluminium cylinder	5.28	0 - 0.44	(Vorathin et al., 2018a)
	FBG and metal bellows	9.06	0- 40	(Pachava et al., 2015)
	FBG and a Bourdon tube	6.69	0-100	(Srimannarayana et al., 2014)

### 3.2.1 UNIFORM PRESSURE

In 1993, the first in-fibre grating high pressure sensor was reported by (Xu et al.). They observed a 0.22 nm shift in the wavelength reflection peak at 70 MPa of uniform pressure on bare fibre, having a sensitivity of 3 pm/MPa. It showed a low sensitivity response at high pressure, and therefore the suitability of FBGs for lower pressure sensing applications was questioned. It was also suggested that temperature compensation was required to correct for temperature changes in the grating (Xu et al., 1993). Since an enhanced pressure sensitivity is highly desirable, a glass-bubble house was introduced as a mechanical amplifier. It enhanced the pressure sensitivity, reducing the thermal crosstalk by more than a factor of 4 by having similar thermal expansion coefficients for the fibre grating

and the glass bubble, although the pressure range was reduced. The pressure sensitivity became 20 times the value for bare fibre, i.e. about 0.4 nm wavelength shift at 14 MPa (Xu, Geiger & Dakin, 1996). In both instances they observed a linear behaviour of the wavelength shift against applied pressure (0 - 14 MPa (Xu, Geiger & Dakin, 1996) and 0-70 MPa (Xu et al., 1993).

Other methods have also been investigated. For example, Bock investigated a high pressure polarimetric sensor by using birefringent optical fibre which measured up to 200 MPa, but also identified that temperature drift was a major drawback of the sensor in enhancing pressure sensitivity (Bock, 1990). To improve sensitivity, several techniques such as dual grating techniques (James, Dockney & Tatam, 1996) and dual wavelength techniques (Xu et al., 1994) have been proposed to separate thermal effects from mechanical effects. In a dual grating technique, two FBGs in different diameters, which had close Bragg wavelengths were placed on either side of the splice and was able to measure temperature and strain independently. In the dual wavelength technique, two different wavelengths were observed by using a superimposed fibre grating. The ratio of those wavelengths was able to provide the strain and temperature successfully.

Low gauge pressure measurement, i.e. near 2 *atm* (200 kPa), becomes more challenging according to the literature. Bal et al. (2010) conducted experiments below 1 *atm* and observed a 0.004 nm wavelength shift due to a pressure change from 1.9 to 3 kPa. Furthermore, they suggested that the wavelength shift can be enhanced by a specialised coating material even though the wavelength shift is small. They investigated the pressure response up to 12 kPa for different FBG lengths and noted that the length of the FBG and the strength of the index of refraction modulation did not affect the pressure sensitivity. Ultimately they recommended the FBG to be used for low pressure measurements even though the graph for wavelength shift vs. applied pressure was non-linear (Bal et al., 2010). Additionally, Bal et al. (2011) observed non-linear responses below 2 *atm*. These non-linear responses are not understood and require further research. According to Bal et al. (2011) and Bock (1990) this could be a result of the way in which the FBG is suspended in the pressure chamber. In other work, Hsu et al. (2006) used a temperature compensation strategy via biomaterial coating

which produced axial strain on a FBG when subjected to uniform elevated pressure with a linear response below 3 atm.

### 3.2.2 TRANSVERSE COMPRESSIVE LOAD

Extensive research has been conducted on the effect of transverse load on FBGs in which some experiments have shown induced birefringence at higher loads (Abe et al., 2003; Correia et al., 2007; Correia et al., 2010; Doyle et al., 2002; Mastro, 2005; Wagreich et al., 1996). Birefringence occurs when the light propagates anisotropically through the material due to the existence of two indices of refraction. The induced birefringence effect in FBGs inscribed in standard fibres was first investigated by Wagreich et al. (1996), with up to 90 N loads on a 2.5 cm length of low birefringence FBG. As the load was increased up to 40 N, broadening of the reflection spectrum was observed. Above 40 N, the reflection peak in the spectrum of the FBG was split into two. It was noted that the applied stress causes a difference in the wavelength in the x and y directions due to the magnitudes of the stress-optic coefficients and the Poisson's ratio of the silica fibre (Wagreich et al., 1996). Mastro (2005) reported that the wavelength shift of FBGs can be measured with great sensitivity when an optical fibre is loaded in the axial direction. However, the reflection spectra of FBGs undergo broadening and splitting due to the induced birefringence when it is loaded from an off-axis direction. Thus, broadening and splitting of FBG signals create problems for tracking an actual spectral peak (Mastro, 2005).

Birefringence occurs intrinsically in polarisation maintaining optical fibre, due to the manufacturing process. FBGs in such fibres exhibit two independent spectral peaks without experiencing external forces (Doyle et al., 2002; Mastro, 2005). (Abe et al., 2003) observed broadening and then splitting of one of the spectral peaks into two when the load increased but it was unclear why this did not occur for both peaks. Furthermore, Udd et al. (2000) reported that an undistributed load causes peak splitting of the reflection spectrum. They showed that the separation of peaks widened as the load increased, whereas Abe et al. (2003) showed the opposite. However, Bjerkan, Johannessen & Guo (1997) observed non-linear responses in the region above 0.5 N/mm in the graph of wavelength change vs. applied force; the birefringence effect was linear up to 0.5 N/mm

for specific coating materials, whereas it was nonlinear with different coating materials at higher loading. Lawrence et al. (1999) observed the same response at higher load levels when the angle of the applied load was not aligned with the intrinsic polarization axis of the fibre. They suggested that the nonlinearity may have been caused by the rotation of the polarization axis due to the external loading although bifurcation of the reflection spectrum was not reported (Lawrence et al., 1999). Barlow & Payne (1983) have shown that the wavelength dispersion of the stress-optic coefficient can affect birefringent fibres and devices significantly. Paul et al. (2005) showed that the wavelength responses of FBG-based strain sensors are highly dependent on the pressurizing media, its configuration and the contact conditions.

### **3.3 REFRACTIVE INDEX VARIATION AND STRESS VARIATION WITH PRESSURE**

Mastro (2005) studied the stress and the changes in the index of refraction in the x and y directions under transverse load in ordinary fibres. The study noticed stress changes were dependent on the load point where the stress is higher at the points closer to the load and lower at the points further from the load point. At the same time, Mastro (2005) observed changes of refractive index along the same axis. More Bragg wavelengths were observed rather than a single wavelength, which is due to broadening and then splitting of the FBG spectra. This investigation was wholly based on transverse load at a single point, and hence further research is required to explore multiple axis loading scenarios. Abe et al. (2003) reported that the splitting of the spectrum was caused by the variation of stress and the index of refraction in the birefringent fibres. Espejo & Dyer (2007) showed that the stress is higher at the edges of the FBG and lower in the centre due to the bending effect. Furthermore, Wade et al. (2011) investigated the effect of bending on FBG spectra, showing a clear shift of wavelength when they are bent into different diameters. They suggested that the structure of the refractive index may depend on bending; hence further investigations are required. In addition, there are some significant effects on the variation of refractive index and strain when FBGs experience axial and radial pressures (Chuang et al., 2010; Shang & Lin, 2010). These axial and radial

pressures affect the accuracy of measurements of axial strain and refractive index changes; this also warrants further investigations (Shang & Lin, 2010).

### 3.4 MATERIAL PROPERTIES

The fibre optic material plays a key role in determining pressure sensitivity; two ways in which this occurs have been identified. One is to use a polymer coating on a silica fibre, while the second uses a polymer as the core material. It has been reported that the low pressure sensitivity of bare glass fibre can be improved by a factor of 40 by coating the fibre with a polymer of low bulk modulus, but the observed enhancement was only 30 (Hill & Meltz, 1997). Bjerkan, Johannessen & Guo (1997) noted that the coating material caused a non-linear response at higher loads. Moreover, Gianino & Bendow (1981) reported that there was difficulty in applying a uniform diametral stress (load or force to the point where a material object is split in half) to a fibre that had a coating. However, it was stated that a uniform diametral stress can be applied on the FBG by using a thin hermetic coating. As an alternative, Prabhugoud & Peters (2007) proposed that the performance of FBG sensors can be improved by reducing the cladding diameter.

Toroghi et al. (2006) reported that the pressure response increased while the temperature response decreased, when a fibre is coated with a thick layer of polymer. It was shown that the effect of pressure and temperature depends on the selection of polymer coating, polymer material and geometrical parameters (Toroghi et al., 2006). To enhance the pressure sensitivity, the coating material requires a low Young's modulus and low Poisson's ratio of the polymer material (Shang & Lin, 2010). The study of Bennett, El-Sherif & Froggatt (2001) has shown that a greater sensitivity to transverse load occurs when a FBG is embedded in a low bulk modulus epoxy. It was also stated that a repeated transverse load on an embedded FBG decreases the sensitivity of the signal due to the degrading interface between the material and the epoxy. Due to the epoxy matrix, stress acts on a FBG in all directions rather than a single point. Therefore, the FBG Bragg wavelength was shifted during transverse loading by changing the index of refraction and periodicity. It has also been shown that the response of the FBG

signal depends on the core geometries and numerical apertures of FBGs (Bennett, El-Sherif & Froggatt, 2001).

Polymer optical fibre (POF) FBGs have gained interest for sensing applications, as its low Young's modulus with higher strain creates a much higher sensitivity than for silica fibres (Peng, 2002). In addition, polymer optical fibres, exhibiting high fracture toughness, high deformation, large yield strain, high flexibility in bending and potential negative thermo-optic coefficient, have several advantages over silica fibre. It has been stated that the sensitivity can be improved by 22% compared to that for silica fibre for the same Bragg wavelength (Peng, 2002). However, FBGs in polymer fibre can be erased by thermal exposure, the reason for which is not yet understood (Liu, Liu & G.D., 2005; Peters, 2011). POF gratings were subjected to considerable strain which showed their potential as strain sensors due to their large wavelength tunability that arises from the properties of the polymer (Xiong et al., 1999). Yuan et al. (2011) observed a linear response of the wavelength shift without peak splitting at high loadings and higher temperatures without hysteresis. They suggested that the high material loss (high attenuation) could be overcome by using short lengths of POF or microstructured POF in future applications.

Another issue is that some of the reported material values for Young's modulus and Poisson's ratio of silica optical fibres vary widely when comparing experimental values with theoretically calculated values. As already noted, the first in-fibre FBG high pressure sensor was reported by Xu et al. (1993). They measured a  $-1.98 \times 10^{-6}$ /MPa fractional wavelength shift in the wavelength reflection peak for up to 70 MPa of uniform pressure. However calculated theoretical magnitudes of the fractional wavelength shift using accepted mechanical parameters of optical fibres are significantly larger (Bertholds & Dandliker, 1988; Hocker, 1979); better agreement has been reported (Budiansky et al., 1979), but in this case the Poisson's ratio was about 50% greater than the accepted value (El-Diasty, 2000). The following table lists the calculated fractional wavelength shift based on the material values that have been reported, showing the need for better understanding of material values.

Table 3.2: Reported material values for the silica fibre and the calculated pressure sensitivity

Quantity	Symbol	(Hocker, 1979)	(Bertholds & Dandliker, 1988)	(Budiansky et al., 1979)	(Leduc et al., 2013)
Young's modulus	$E$ (GPa)	70	70	62	75.3
Poisson's ratio	$\nu$	0.17	0.16	0.24	0.19
Effective refractive index	$n_{eff}$	1.465	1.465	1.460	1.447
First strain optic coefficient	$P_{11}$	0.121	0.113	0.130	0.113
Second strain optic coefficient	$P_{12}$	0.270	0.252	0.280	0.252
Pressure sensitivity	$\frac{\Delta\lambda_p}{\lambda_B \Delta P}$ (/MPa)	$-2.74 \times 10^{-6}$	$-3.28 \times 10^{-6}$	$-2.22 \times 10^{-6}$	$-2.92 \times 10^{-6}$

### 3.5 BRAGG WAVELENGTH MONITORING; EXPERIMENTAL AND THEORETICAL

The basic operation of FBGs is based on a wavelength shift due to a change in material and physical properties when subject to pressure, strain, temperature, etc. (Kersey et al., 1997). As FBGs are a spectrum filter when a broad band of light propagates through the fibre by virtue of the Bragg's condition a narrow spectrum is reflected, whilst the rest is transmitted. The transmitted or reflected spectrum can be monitored by a wavelength monitoring system such as an optical spectrum analyser (OSA). Figure 3.1 illustrates the wavelength monitoring system of FBGs sensors.

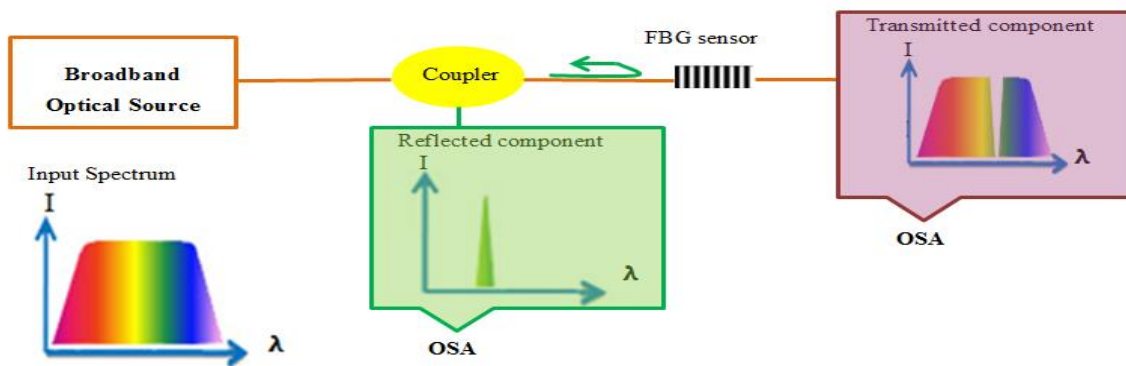


Figure 3.1: Schematic diagram of typical FBG sensing system

As mentioned in Section 1.3 the Bragg grating wavelength depends on the effective index of refraction and the periodicity of the grating. Any material and/or

physical property changes result in a wavelength shift from the initial value. Hence the sensitivity of the FBGs is defined via the related parameter (e.g. pressure, temperature). For example, the grating spacing and the index of refraction changes if an optical fibre undergoes thermal expansion. Strain effects such as longitudinal or transverse strain affect the fractional change in the grating pitch due to physical elongation of the sensor. It induces stress, thereby changing the index of refraction which could lead to birefringence in the two eigenaxes of the fibre core. When FBGs experience elevated pressure, the grating pitch is compressed and this changes the Bragg condition.

The relationship between a change in the Bragg wavelength due to strain, stress, temperature and uniform pressure is discussed below.

The strain or temperature,  $T^f$  response relative to a reference temperature,  $T_0^f$  of the Bragg wavelength along the  $x$ - and  $y$ - eigenaxis when light propagates along the  $z$  direction in unbounded optical fibre has been described by the following equations (Sirkis, 1993).

$$\lambda_{Bx} = \lambda_{Bx}^0 \left\{ 1 + S_z^f - \frac{1}{2} n_0^2 [p_{11} S_z^f + p_{12} (S_z^f + S_y^f)] + \xi T^f \right\} \quad \text{Equation 3.1}$$

$$\lambda_{By} = \lambda_{By}^0 \left\{ 1 + S_z^f - \frac{1}{2} n_0^2 [p_{11} S_z^f + p_{12} (S_z^f + S_x^f)] + \xi T^f \right\} \quad \text{Equation 3.2}$$

Where  $p_{11}$  and  $p_{12}$  are the first and second strain optic coefficients for parallel and perpendicular stresses respectively.  $\lambda_{Bx}^0$  and  $\lambda_{By}^0$  are denoted for Bragg wavelengths for the  $x$  and  $y$  directions without strain variation at the reference temperature  $T_0^f$ . The superscript,  $f$ , indicates that the strain and temperature refer to the optical fibre. The thermo-optic coefficient is represented by  $\xi$  and  $S_i^f$  ( $i = x, y, z$ ) are the strain component along the  $x$ ,  $y$  and  $z$  axes.

When stress is applied to an isotropic material, the indices of refraction in the plane of polarization change, and hence the material becomes anisotropic. The change in refractive index due to stress is derived from *Equation 3.1* and *Equation 3.2* and is given by *Equation 3.3* and *Equation 3.4* as follows:

$$(\Delta n_{eff})_x = -\frac{n_0^3}{2E} \{(p_{11} - 2v p_{12}) \sigma_x + [(1-v)p_{12} - v p_{11}] (\sigma_y + \sigma_z)\} \quad \text{Equation 3.3}$$

$$(\Delta n_{eff})_y = -\frac{n_0^3}{2E} \{(p_{11} - 2v p_{12}) \sigma_y + [(1-v)p_{12} - v p_{11}] (\sigma_x + \sigma_z)\} \quad \text{Equation 3.4}$$

Where  $E$  and  $\nu$  are the Young's modulus and Poisson's ratio of the fibre and  $\sigma_x, \sigma_y$  and  $\sigma_z$  are the stress components in the  $x, y$  and  $z$  direction respectively and  $\sigma_x$  and  $\sigma_y$  are given by the following Equations:

$$\sigma_x = \frac{2F}{\pi h D} \quad \text{Equation 3.5}$$

$$\sigma_y = \frac{6F}{\pi h D} \quad \text{Equation 3.6}$$

Where  $F$  is the applied force,  $D$  is the diameter of optical fibre and  $h$  is the length of the stress plane.

When a load is applied such as a point load or edge load on low or non-birefringent single mode fibre in the transverse direction, the fibre will be deformed by reducing the fibre diameter along the applied directions while increasing the length in the perpendicular direction. Hence, stress is induced due to strain changes. Due to this induced stress the index of refraction is changed which causes a birefringent effect in the fibre. The change in wavelength along the 2 eigenaxes due to transverse strain is given by the following equations (Wagreich et al., 1996):

$$\Delta\lambda_{Bx} = -\frac{1}{2}\lambda_{Bx}n_0^2(p_{11}\varepsilon_{xx} + p_{12}\varepsilon_{yy}) \quad \text{Equation 3.7}$$

$$\Delta\lambda_{By} = -\frac{1}{2}\lambda_{By}n_0^2(p_{11}\varepsilon_{yy} + p_{12}\varepsilon_{xx}) \quad \text{Equation 3.8}$$

Where  $\varepsilon_{xx}$  is the strain along the  $x$  and  $\varepsilon_{yy}$  is the strain along the  $y$  direction. The plane strains along both directions can be calculated using Hooke's law.

$$\varepsilon_{xx} = \frac{1+\nu}{E}(\sigma_{xx}(1-\nu) - \nu\sigma_{yy}) \quad \text{Equation 3.9}$$

$$\varepsilon_{yy} = \frac{1+\nu}{E}(\sigma_{yy}(1-\nu) - \nu\sigma_{xx}) \quad \text{Equation 3.10}$$

In summary, these equations can be used to calculate stress (*Equation 3.5*, and *Equation 3.6*) and strain (*Equation 3.9* and *Equation 3.10*) manually. Hence wavelength shifts (*Equation 3.7* and *Equation 3.8*) and refractive indices can be calculated. As the analysis in this thesis is carried by using FEA, the stress and strain values are directly imported from the simulation without manual calculation. Therefore the wavelength shift was calculated using *Equation 5.6* and *Equation 5.7*, as presented in Chapter 5.

When a FBG is subjected to uniform pressure, the wavelength shift can be calculated using *Equation 3.11* (manually).

$$\Delta\lambda_P = \lambda_B \left[ -\frac{(1-v)}{E} + \frac{n^2}{2E}(1-2v)(2p_{12} - p_{11}) \right] \Delta P \quad \text{Equation 3.11}$$

A FEA model has been developed to analyse the pressure sensitivity by using strain variation in the axial and radial direction. Hence the wavelength shift was analysed using *Equation 5.10* (see Chapter 5) instead of using *Equation 3.11*.

### 3.6 SUMMARY

This chapter focused on an understanding of the behaviour of a FBG based strain sensor and considered how pressure sensitivity of uniform pressure sensors may be enhanced. At the beginning of the chapter, a discussion was given on the history of FBG based pressure sensors and different techniques applied to measure pressure sensitivity of FBGs. It then continued to discuss the effect of different ways that pressure may be exerted on fibres such as transverse load followed by a report of non-linear responses of certain sensors and stress and refractive index variation on the fibre due to applied pressure. Lastly, the material influence was considered for the discussion and its effect on FBG sensors was further explained. It further explained the calculation of Bragg wavelength changes due to stress, strain and refractive index changes, which underpin the FEA model described in Chapter 5.

## **CHAPTER 4: Finite Element Analysis (FEA)**

### **4.1 OVERVIEW**

The core objective of this chapter is to provide information on Finite Element Analysis (FEA) modelling of optical fibres, fibre Bragg grating structures and their spectrum using the *wave optics* module in the software package COMSOL Multiphysics simulation software. FEA is performed to determine the occurrence of modes in single mode fibre (SMF-28) for comparison to establish its usefulness in solving optical waveguide problems. This chapter will mainly investigate the behaviour of complex FBG structures using spectral FEA and FFT analysis to compare with theoretical, simulated and previously reported experimental results.

In supporting FEA modelling, this will discuss and provide in detail:

- The selection of coordinate systems for 2-D and 3-D geometric modelling
- The selection of materials and their properties
- Physics setup
- Mesh arrangement
- Study setup and
- Analysis methodologies

### **4.2 WHY FINITE ELEMENT ANALYSIS (FEA)?**

Today, computer aided FEA software has become a key component in most engineering fields such as production markets, to design products for consumer demand and needs, weather forecasting in meteorology, infrastructure development such as building and bridge designing in civil engineering, vehicle and aircraft production to analysis problems such as crash investigation, heat transfer, fluid mechanics and material flow. The main advantage of the FEA method is using numerical methods to solve complex problems as most of the problems can't be solved analytically using numerical equations. In production markets FE modelling is more popular due to cost effectiveness, time management, effective design capability, inexpensive in materials used, safe under extreme operating conditions and so an actual test might be unnecessary.

There are number of FEA software packages: examples include COMSOL, ANSYS, NASTRAN and ADINA available in the current market for different purpose in research and engineering fields. For this study, the analysis was performed using COMSOL software.

COMSOL is designed to address real-world problems in engineering and scientific fields. These problems are a combination of different sciences. COMSOL is Multiphysics software which has different scientific modules such as acoustic, fluid flow, structural mechanics, chemical reaction, heat transfer, wave optics, mechanics, etc... Therefore, it provides more opportunities for users to address a problem by combining the required physics modules, making it easier and more creative over other available software. The user has complete control of their design; this is other major advantage of the software. The recent use of software in NASA applications has proven the advancement of the software in engineering applications (Kanakaraj, Lhaden & Karthic, 2015; Rivera et al., 2010; Starinshak, Smith & Wilson, 2008). Therefore, the advancement in the software lead to use FEA in this project to save effort in useless or unrewarding experiment, and that avoided by undertaking a laborious program of fibre coating exercise (Zheng, 1986).

In this study COMSOL Multiphysics software with the *structural mechanics* module and the *wave optics* module was used for structural mechanics and optics simulations. The *wave optics* module was used to model normal FBG patterns to understand the grating formation produced by a phase mask and its reflection spectra. This will help to improve the quality of the phase mask in the manufacturing process and help researchers and engineers in employing the behaviour of its resultant FBG and its spectrum for sensing purposes. For pressure sensing, to enhance the sensitivity, different polymer coating materials have been analysed with the help of the *structural mechanics* module in COMSOL. Finally, the *structural mechanics* and *wave optics* modules were used for multiphysics simulation to study and confirm the nonlinear behaviour of strain and pressure sensing, which have been reported experimentally.

## 4.3 INTRODUCTION (HISTORY) OF FINITE ELEMENT ANALYSIS (FEA)

The FEA is a numerical method of solving problems of engineering and applied science using partial differential equations. The era of FEA began with introducing the concept of spatial discretization for the solution of a torsion problem by the New York University mathematician, Professor R.L. Courant, in 1941 (Pelosi, 2007). Courant introduced discretization by a set of triangles which he addressed as “elements”. In 1956, Ray W. Clough, Jr. who introduced the term “finite element”, and his colleagues from University of California, published FEA as a natural extension of matrix analysis (Clough, 1980). Later, they applied the FEA method for creating a plate structure for aircraft in the aerospace industry successfully. It grew from the aerospace industry to structural engineering areas as a useful solution for problems where analytical solutions cannot be obtained with such complicated geometries, dissimilar material properties and loading, etc. In the electrical engineering field, FEA design was first reported in the 1960s (Pelosi, 2007). The interest in using FEA for modelling in optical fibre technology was reported since 1986 (Zheng, 1986). FEA has become more popular and a practical and technical tool in conjunction with the development of digital computers since 1960. Today, FEA computational software applications can be found in various engineering fields such as mechanical, aerospace, civil, and automotive and they are finding a broader range of uses in analysing heat transfer, electromagnetic fields, fluid flow, acoustics, biomechanics, etc.

### 4.3.1 FINITE ELEMENT ANALYSIS (FEA)

FEA is a computational technique for performing analysis of boundary value problems. These boundary value problems such as electromagnetic, fluid flow, structural mechanics, and thermodynamics can be expressed by combining the governing equations (e.g. differential equations) and boundary conditions as shown in Figure 4.1.

Boundary value problem → Governing equation (differential equation) + Boundary Conditions

Figure 4.1: Representation of Boundary Value Problem

The boundary conditions can also be represented by mathematical equations. Although boundary value problems can be represented by a number of equations, the problem arises with solving those equations manually due to their complexity. It can be obtained by approximating the solution by using FEA. FEA uses a set of simultaneous algebraic equations to represent the problem as follows.

$$[K]\{u\} = \{F\} \longrightarrow \text{Action}$$

Equation 4.1

To clarify, an example of equation is given here: if the action is a force or pressure and the properties are physical properties of geometry and material properties, then the behaviour is calculated using this information. As the property and action are known, the behaviour can be evaluated, simplifying to the following equation which is produced by a matrix inversion method.

$$\{u\} = [K]^{-1}\{F\}$$

Equation 4.2

However, the solving of the above equation becomes more difficult when it is applied on the entire geometry of a complex structure. However, this complex analysis can be turned into a simple analysis with the use of FEA. FEA is a volume discretization method that divides the whole problem (object, Figure 4.2 (a)) into an equivalent system of many smaller units or body parts which are called finite elements (e.g. Figure 4.2 (b)). The shape of these elements mostly depends on the dimension of the original object. The dimensions of the original object can be 1-D, 2-D or 3-D. If it belongs to a 1-D domain, the element can be represented by a line. In a 2-D problem, the element shapes become triangular or rectangular shapes, whereas in a 3-D situation, the element shapes are tetrahedral blocks, rectangular blocks or triangular prisms (pentahedron). These elements are interconnected with another two or more elements at points, which are called nodes or nodal points, and boundary lines or surfaces, as shown in Figure 4.2.

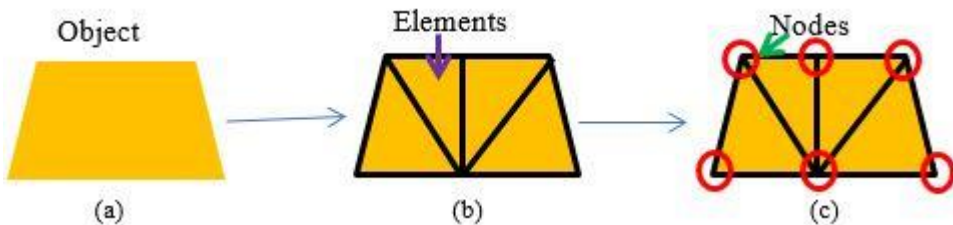


*Figure 4.2: Schematic diagram of volume discretization method in FEA (a) the object which represent the problem (b) the object is divided into number of small units which is called elements (c) elements are a combination of points and lines or surfaces*

At every node, the field variables, which are explained as dependant variables of differential equations, must be calculated. The field variables over an element are interpolated by a polynomial equation. In connecting nodes, each adjacent element shares the degree of freedom which is equal to the product of the number of nodes and the values of field variables. The final result for a desired study will be given by obtaining a set of simultaneous algebraic equations on each element of the problem to be solved and summing over the entire volume.

In FEA, the computational space, called the model domain, is divided into a finite number of subdomains. There are number of advantages of using subdomains. Subdomains can represent complex geometry and different material properties more accurately. They will divide the original problem into a smaller set of problems; hence the problem can be configured in a way so that more information is collected. This will lead to solving the problem easily as FEA software is capable of mesh generation and have programmes with in-built algorithms. Then equations are applied to each subdomain related to the problem analysis and will sum over the entire mesh which is decided considering the domain structure.

In general, there are three major processes in FEA. They are pre-processing, solution and post processing. In pre-processing, a Finite Element model is built by the user. Then numerical analysis is conducted using computers to find solutions, which is the second phase. At the finish a user can see the results by viewing on the screen or printing which is called post processing step. The following flow chart illustrates the FEA process (see Figure 4.3).

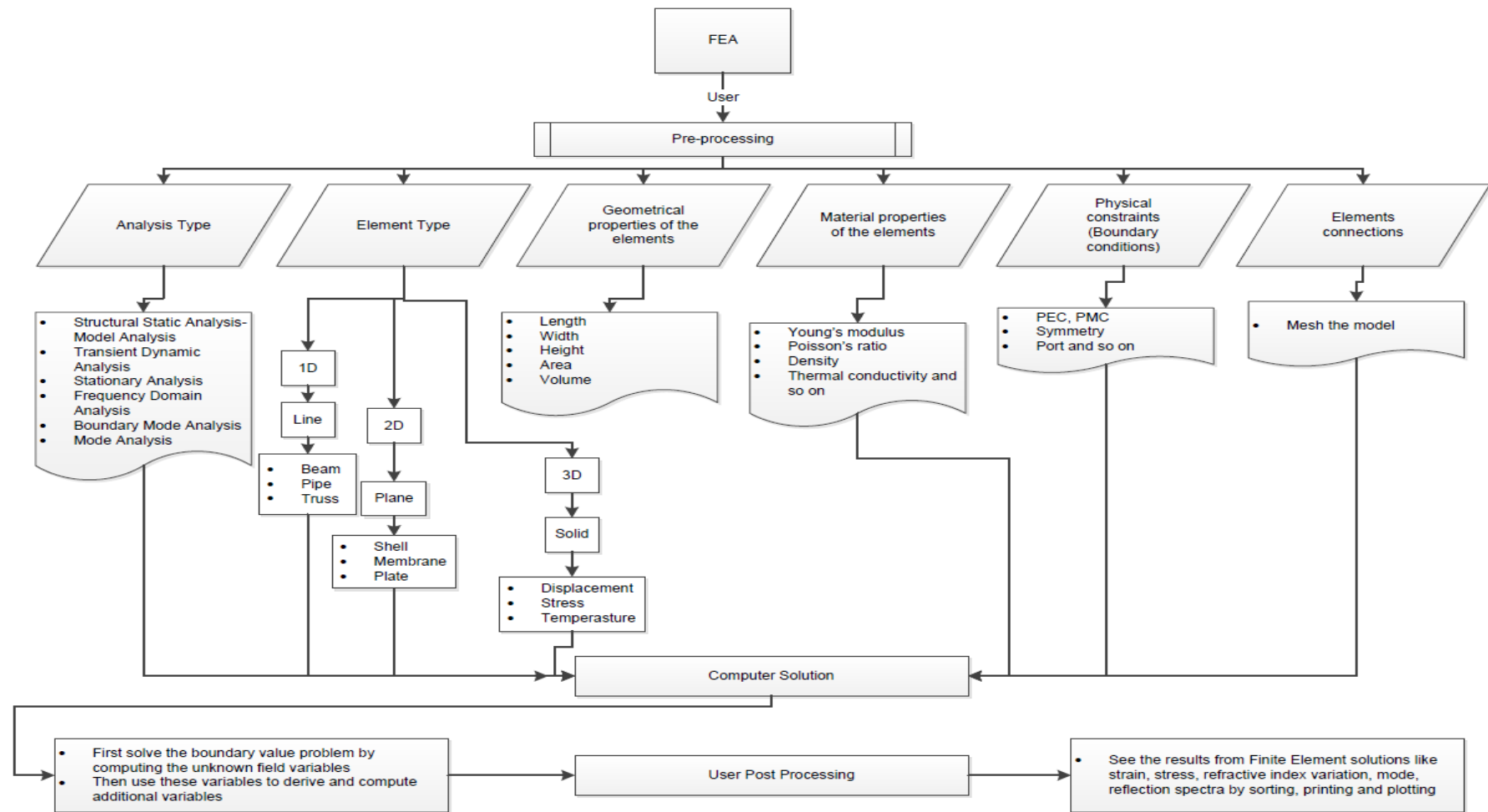


Figure 4.3: Flow chart of FEA process

Although FEA is the most popular method for solving complex problems some issues have been identified. FEA produces only an approximate solution and not the exact solution; therefore, inherent errors exist. Those errors may have occurred during FEA formulation or FEA while computing. Also, the mistakes made by users such as: defining the wrong element type, inconsistent unit use, and insufficient boundary conditions can be disastrous in field applications. Therefore, particular care has to be given to minimize the errors so that, optimum results can be obtained for the analysis of any field problem.

In this study, FEA has been performed targeting two main aims. They are:

1. Computational modelling of FBG refractive index patterns using multiple phase mask orders and analysis of their spectra at various wavelengths.
2. Computational modelling of the pressure sensitivity of an FBG within an optical fibre having different coating materials, and to obtain an optimum coating material based on the results

#### **4.4 FINITE ELEMENT ANALYSIS OF MODES IN OPTICAL FIBRES AT $\lambda_B$ , $2\lambda_B$ AND $(\frac{2}{3})\lambda_B$**

Single mode fibre SMF-28 has been chosen for simulation and experiment for this study. The properties of SMF-28 fibre considered are listed in Table 2.1. In order to confirm the mode propagating through this single mode fibre, FEA analysis was performed using the values in Table 2.2: Physical and material properties of SMF-28 (FEA simulation).

A 2-D cross section of a fibre end-face has been considered to observe the allowed modes in the fibre, as shown in Figure 4.4. Refractive indices of cladding (1.4447) and core (1.4504) are introduced (values derived using Table 2.1) and wavelength of operation was set to 1550 nm ( $\lambda_B$ ). The computational result was undertaken in COMSOL software, using mode analysis, under study node. The model has followed Step-index Fibre simulation in COMSOL (COMSOL Inc, n.d.).

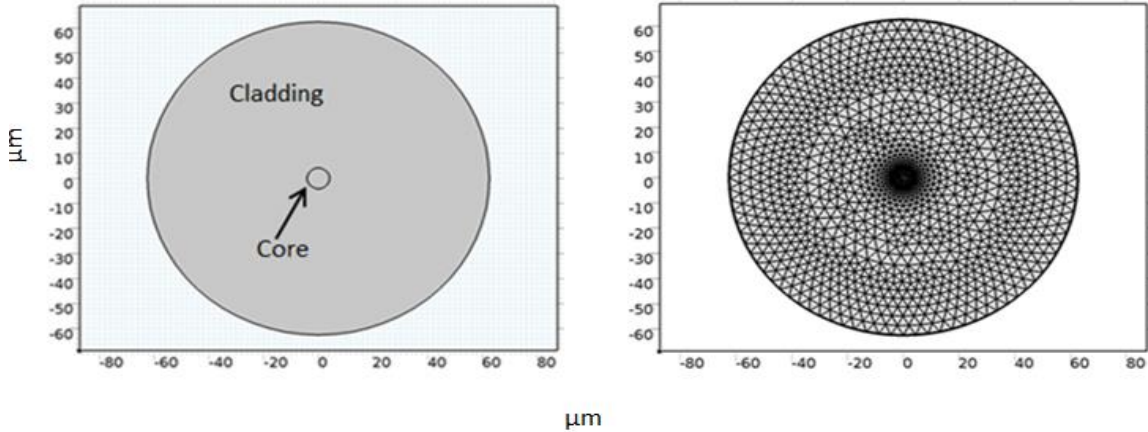


Figure 4.4: End face of optical fibre of SMF-28 and its mesh diagram

The same analysis was performed to find the number of modes in SMF-28 by changing the wavelength to  $2\lambda_B$  and  $(\frac{2}{3})\lambda_B$ . In the first two cases ( $\lambda_B, 2\lambda_B$ ), the calculated  $V$  values are 2.1561 and 1.0780 respectively. Therefore, they satisfy the single mode condition ( $V < 2.405$ ). At  $(\frac{2}{3})\lambda_B$  the  $V$  value is 3.2341 ( $V > 2.405$ ), which was previously shown as a vertical red line in Figure 2.4. Therefore, it should behave like multimode fibre allowing more modes to propagate: i.e. 4 modes are expected. The analysis results for different wavelengths are given a brief description in the following sections.

#### 4.4.1 MODES AT $\lambda_B$ AND $2\lambda_B$

To analyse the number of modes guided through SMF-28, a cross section of the x-y plane (end view of optical fibre), as shown in Figure 4.4, was created. According to Maxwell's equations, the wave propagation in the z direction is be given by

$$\mathbf{E}(x, y, z, t) = \mathbf{E}(x, y)e^{j(\omega t - \beta z)} \quad \text{Equation 4.3}$$

where  $\omega$  is the angular frequency

An eigenvalue equation for the electric field  $\mathbf{E}$  is obtained by deriving the Helmholtz equation (Equation 4.4) which is solved for an eigenvalue of wavelength (Equation 4.5)

$$\nabla \times (\nabla \times \mathbf{E}) - k_0^2 n^2 \mathbf{E} = 0 \quad \text{Equation 4.4}$$

$$\lambda = -j\beta \quad \text{Equation 4.5}$$

For a confined mode, there is no energy flow in the radial direction. Therefore, as expected, in the cladding region (see Figure 2.1), there is an evanescent field as shown in Figure 4.5, in which the electric field is observed to decay exponentially in the  $\pm x$ -direction.

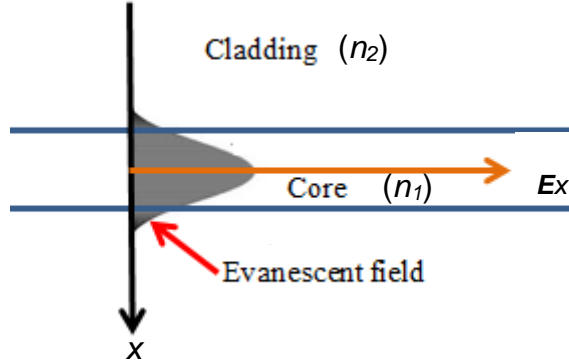


*Figure 4.5: Electrical field profile across optical fibre for a guided mode*

To satisfy mode propagation in the core region, the following conditions are required

$$n_2 < n_{eff} < n_1$$

where  $n_{eff}$  is the effective mode index and is given by

$$n_{eff} = \frac{\beta}{k_0} \quad \text{Equation 4.6}$$

Simulations were carried out for different wavelengths. The results, such as effective mode indices and mode shapes at different wavelengths, are discussed below.

Firstly, the two surface graphs (Figure 4.6 (a) and Figure 4.7 (a)) show the fundamental propagation mode within the fibre in terms of the electric field  $\mathbf{E}(x,y)$  for  $\lambda_B$  and  $2\lambda_B$ , respectively. The corresponding line graphs (Figure 4.6 (b) and Figure 4.7 (b)) represents the intensity variation across the fibre, at  $(x, 0)$  in each case.

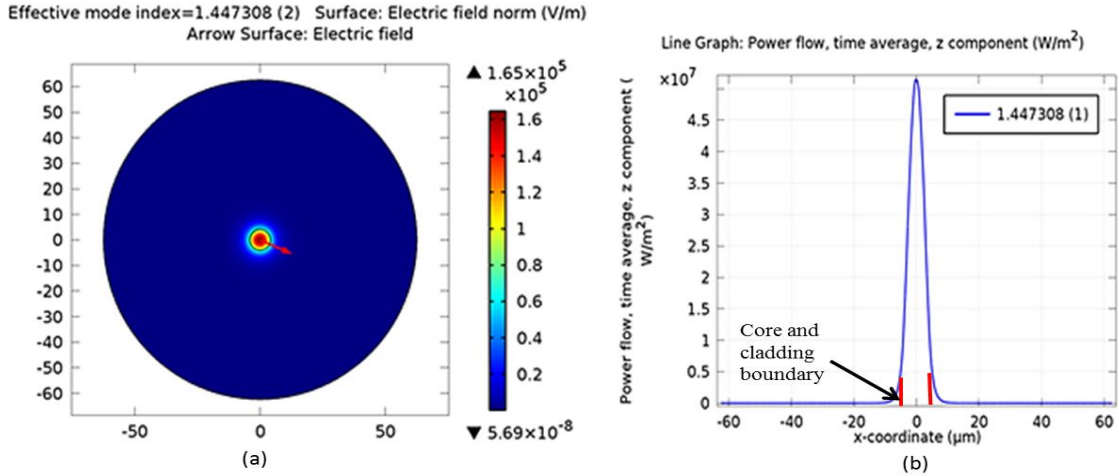


Figure 4.6: (a) Electric field variation of  $HE_{11}$  in the fibre surface and (b) Intensity variation along  $z$  direction across fibre core (b) at  $\lambda_B$

According to Figure 4.6 (a), the effective mode index is 1.4473 at  $\lambda_B$ , with most of the light confined to the core region. Figure 4.6 (b), showing a line graph of intensity variation across the fibre, also shows the concentration of light only in the core region, and resembles Figure 4.5. The simulation result provides only one value for the effective mode index; hence, it confirms the guidance of one mode ( $HE_{11}$ ) at  $\lambda_B$ .

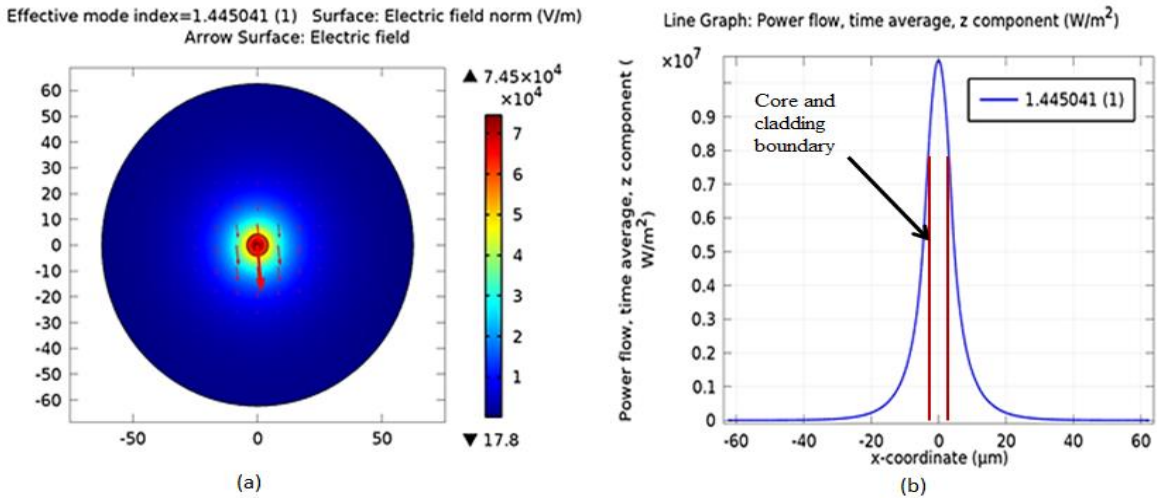


Figure 4.7: (a) Electric field variation of  $HE_{11}$  in the fibre surface and (b) intensity variation along  $z$  direction across fibre core at  $2\lambda_B$

For the wavelength  $2\lambda_B$ , the effective mode index was obtained as 1.44504 which is less than the value at  $\lambda_B$ . As given in Figure 4.7 (a), the electric field normalization diagram shows that the light is not only travelling through the core region but also in the cladding area. Figure 4.7 (b), shows a significant increase

of optical power within the cladding area, compared to the results obtained for  $\lambda_B$ . Similar to  $\lambda_B$ , there is only one effective mode index value given for  $2\lambda_B$ ; hence, at this wavelength there is also just one mode propagating ( $HE_{11}$ ).

#### 4.4.2 MODES AT $\frac{2}{3}\lambda_B$

Four modes were obtained, and the surface diagrams (Figure 4.8 to Figure 4.11) show the electric field normalization and their electric field ( $E_x$ ) component in each case.

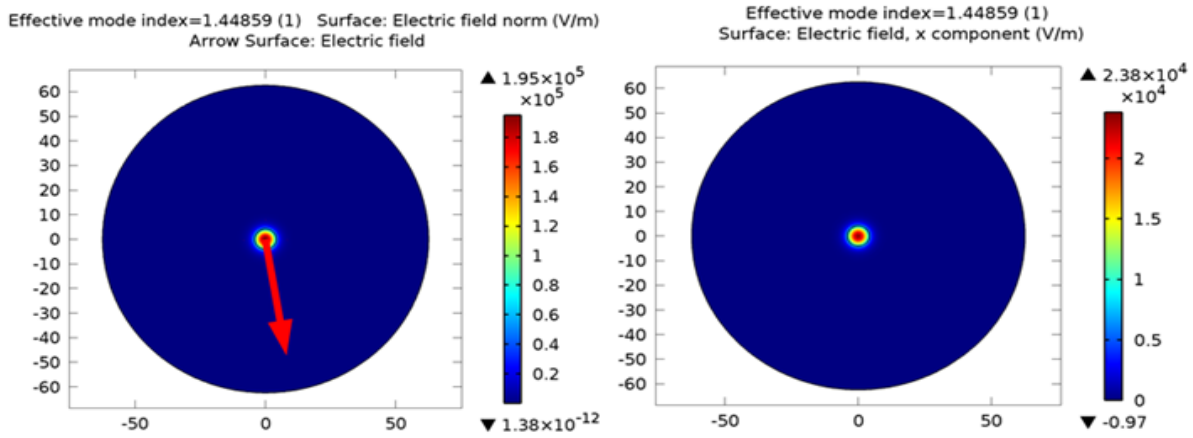


*Figure 4.8: Electric field variation of  $HE_{11}$  in the fibre surface and electric field variation along x direction across fibre core at  $(\frac{2}{3})\lambda_B$*

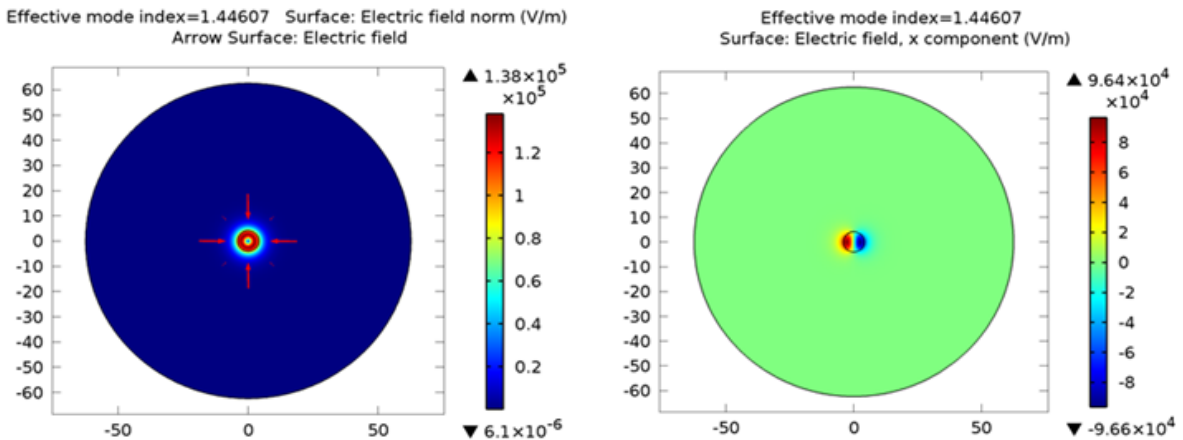


*Figure 4.9: Electric field variation of  $TM_{01}$  in the fibre surface and electric field variation along x direction across fibre core at  $(\frac{2}{3})\lambda_B$*

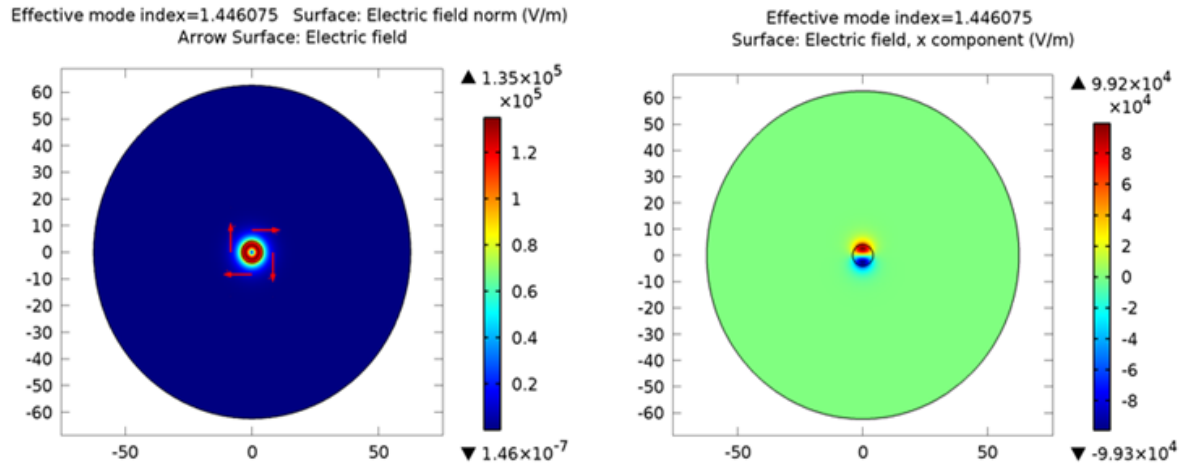


*Figure 4.10: Electric field variation of  $TE_{01}$  in the fibre surface and electric field variation along x direction across fibre core at  $(\frac{2}{3})\lambda_B$*

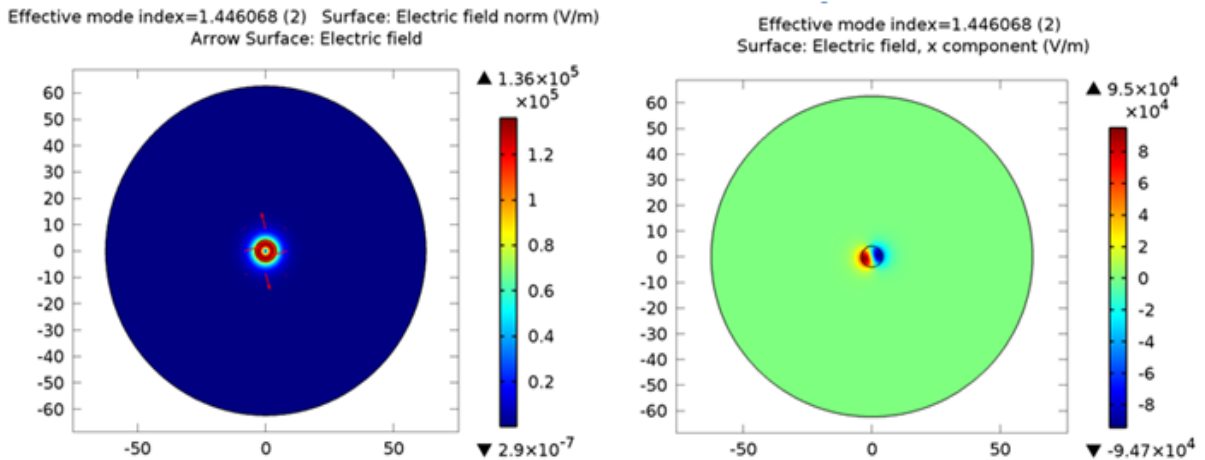


*Figure 4.11: Electric field variation of  $HE_{21}$  in the fibre surface and electric field variation along x direction across fibre core at  $(\frac{2}{3})\lambda_B$*

According to the simulation, the given effective mode indices are 1.44859, 1.44607, 1.46075 and 1.446068, for these modes ( $HE_{11}, TM_{01}, TE_{01}$  and  $HE_{21}$ ) propagating in the optical fibre. Therefore, at  $(\frac{2}{3})\lambda_B$ , an optical fibre behaves like a multimode fibre allowing more than one mode to propagate. The following diagram (Figure 4.12) shows the field variation across the fibre (along the x direction) for each of these modes. The results confirm that the light is guided through the core with some penetration into the cladding region in each case.

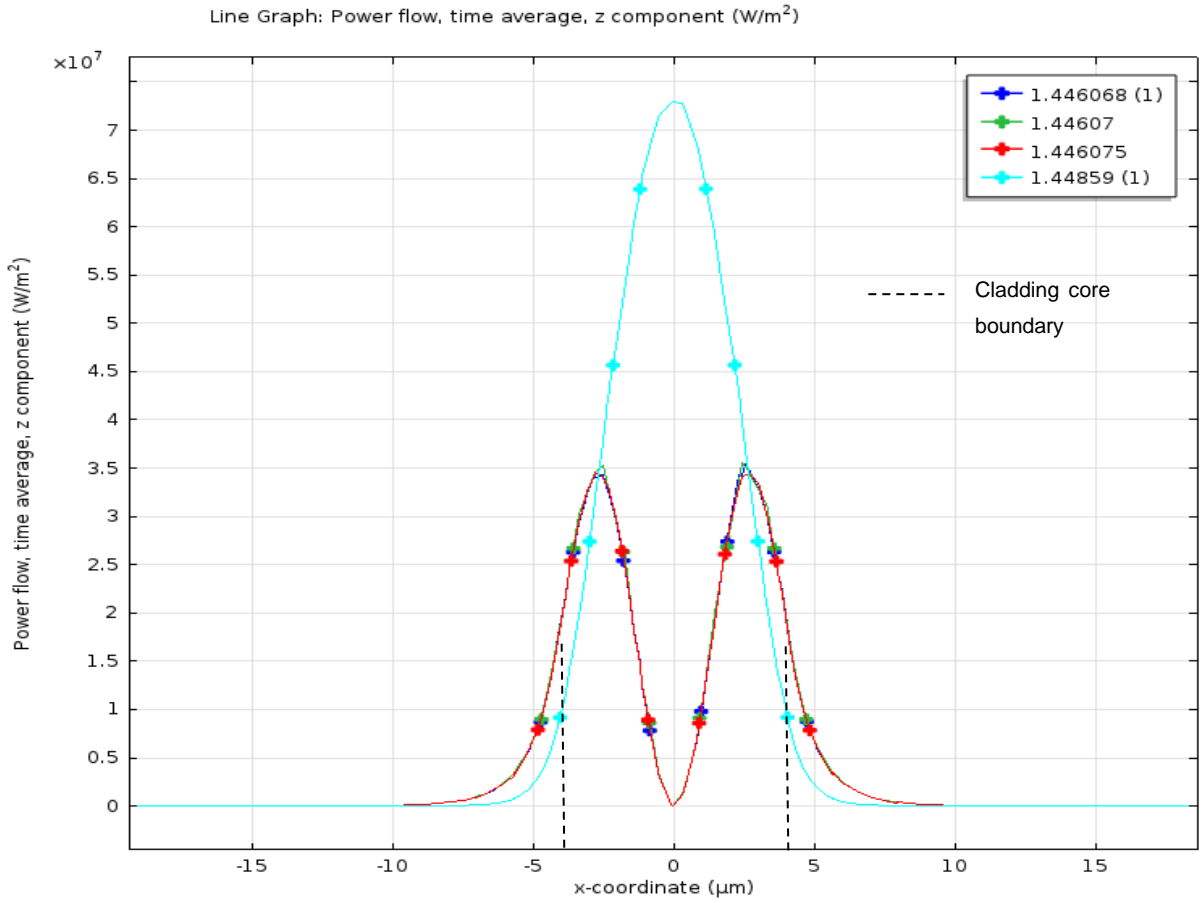


Figure 4.12: Electric field variation of each mode in the fibre surface x direction across the fibre core at  $(\frac{2}{3})\lambda_B$

#### 4.5 COMPUTATION MODELLING OF FBG AND THEIR SPECTRA

This will be focused on the simulation of FBG refractive index patterns according to the phase mask details given in Section 2.4.2. The resultant intensity variation at different sections of the core line will be discussed and FFT analysis will be performed to obtain the periodicities along the fibre core (Section 4.6). Finally, simulations are performed to find the reflectivity (as discussed in Section 2.4.5) and number of peaks produced at different wavelengths when broadband light is propagating through it (Section 4.7). Thus, computational modelling was performed via:

1. FEA on complex FBGs formation by illumination of a phase mask by UV light
2. FEA on wave spectrum produced by the complex FBG (obtained in (1))

#### 4.5.1 FEA ON COMPLEX FBG FORMED BY PHASE MASK UNDER UV ILLUMINATION

The computational modelling was undertaken by considering the real scenario of FBG fabrication using the phase mask method. In order to achieve that, the parameters of the phase mask given by manufacturers have been chosen compatible with the experimental results reported by Kouskousis (2009) and Rollinson (2012). So the complex FBG structure is simulated using an UV laser which is operated at 244 nm wavelength ( $\lambda$ ) with 106 mW of operating power ( $P_{in}$ ) and a 1 mrad beam divergence ( $\theta$ ). The following physical parameters of the phase mask, as shown in Figure 4.13, were used to model the phase mask structure in accordance with manufacturing details.

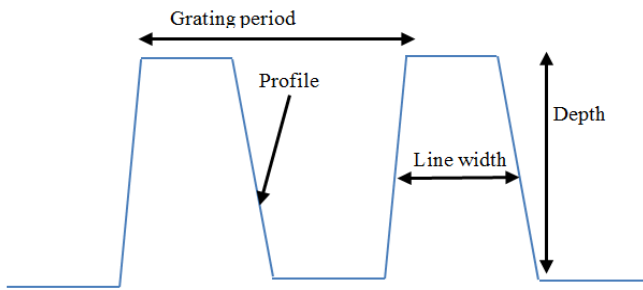


Figure 4.13: Schematic diagram of phase mask structure

The parameters (provided by Ibsen Photonics) of phase mask structure are listed in Table 4.1:

Table 4.1: Parameters and values for the simulation\*

Parameter	Value
Grating period ( $d$ ) (the distance between equally spaced grating grooves or lines depth)	1066 nm
wavelength ( $\lambda$ )	244 nm
Refractive index of air ( $n_a$ )	1
Refractive index of fused silica ( $n_b$ )	1.488 (Equation 4.10)
Etch depth (the height of the grating grooves)	250 nm
Duty cycle (given by: line width/grating period)	44%
Line width of phase mask (the width of grating grooves)	$4.6904 \times 10^{-7}$ m
Height of silica substrate	100 $\mu$ m
Height of the core of fibre	8.2 $\mu$ m
Height of the cladding of the fibre	125 $\mu$ m

\* Grating profile is the shape of the grating grooves (rectangular, sinusoidal, trapezoidal, etc.) and it is assumed that the grating profile is rectangular for this modelling

As shown in Figure 4.13, the phase mask consists of equally spaced multiple grooves. When a laser beam is incident on the phase mask, it will diffract and

separate into discrete multiple beams. Simultaneously, the separated beam will be dispersed by the gratings, satisfying *Equation 4.7*.

$$m\lambda = \Lambda \cdot (\sin\theta_i + \sin\theta_D) \quad \text{Equation 4.7}$$

Where  $m$ ,  $\lambda$ ,  $\Lambda$ ,  $\theta_i$  and  $\theta_D$  represent the  $m$ 'th order of diffraction, wavelength of illumination, grating period of phase mask, incidence angle of illumination and diffraction angle of illumination of  $m$ 'th order respectively (refer Figure 4.14 for diagrammatic representation).

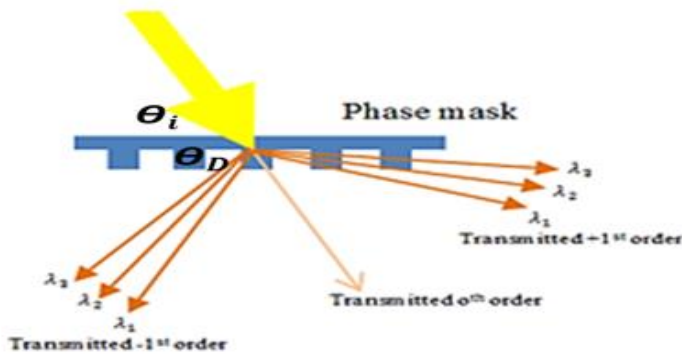


*Figure 4.14: Schematic diagram of beam splitting at phase mask with respect to the angle of incident*

When the angle of incidence is normal to the phase mask, as shown in Figure 2.10, *Equation 4.7* simplifies to *Equation 4.8*.

$$m\lambda = \Lambda \times (\sin\theta_D), m = 0, \pm 1, \pm 2, \pm 3, \dots, \pm n \quad \text{Equation 4.8}$$

If  $\theta_D \rightarrow 90^\circ$ ,  $\sin\theta_D \rightarrow 1$  Hence,

$$|m_{max}| = \Lambda/\lambda \quad \text{Equation 4.9}$$

The above equation (*Equation 4.9*) can be used to calculate the largest possible diffraction order which exists because of phase mask diffraction. The resultant interference pattern produced by the diffracted light of TE illumination will be discussed in subsequent sub-sections.

#### a) Physical domain of the model

The model has been formulated using the *Wave Optics* module of COMSOL. The 2-D cross section in Figure 4.15 represents the scenario of FBG fabrication using

the phase mask method. Phase masks consist of an array of gratings. Modelling of an exact phase mask is a time and memory consuming task due to the large number of individual gratings required to produce interference patterns in a three-dimensional (3-D) domain using computer software. Therefore, 2-D modelling of the phase mask structure was constructed as if it were an array of 1-D gratings. Although an optical fibre is a cylindrical object, previous studies have applied 2-D cross sections and confirmed no significant variation for results (Tarnowski & Urbanczyk, 2013). A unit cell of gratings within a phase mask was devised for the model. It was assumed that a laser beam of 244 nm wavelength was incident on a fused silica grating of refractive index 1.488. The refractive index value was calculated using *Equation 4.10* when the etched depth and incident wavelength are known.

$$d \cdot (n - 1) = \lambda/2 \quad \text{Equation 4.10}$$

Where  $d$ ,  $n$  and  $\lambda$  are etch depth, refractive index of fused silica and wavelength of the incident beam, respectively (Kashyap, 1999).

The computational design considers parameters and values as shown in Table 4.1. The propagated beam through a unit cell diffracts and then interferes behind the phase mask, resulting in a complex FBG pattern, as discussed in Section 2.4.2. For all calculations, the axis of the optical fibre was placed 72.5  $\mu\text{m}$  away from the phase mask, as shown in Figure 4.15, in accordance with typical experimental arrangements, which optimises the interference pattern in the fibre core. The 10  $\mu\text{m}$  air gap ensures that no damage to the phase mask structure can occur through contact with the fibre.

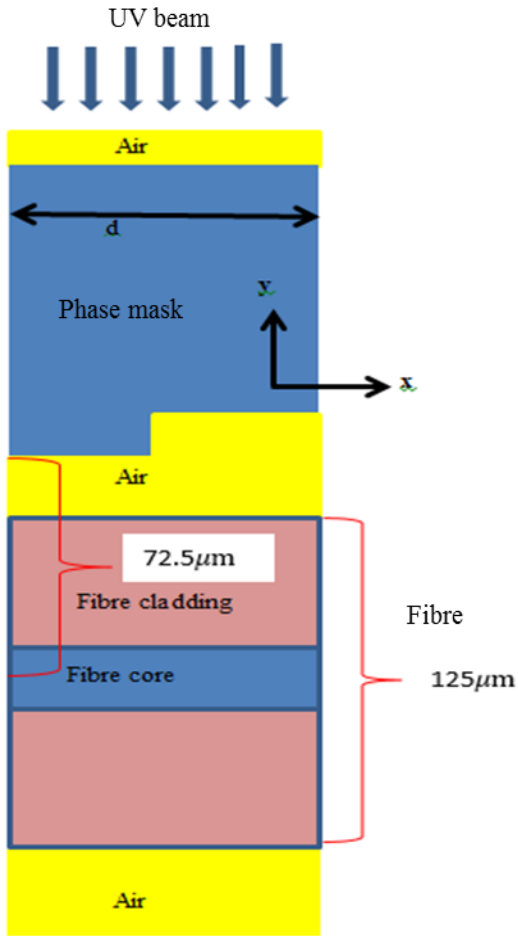


Figure 4.15: Schematic diagram of FBG writing process using phase mask method for a unit cell

### b) Mathematical Model

The wave optics module in COMSOL software uses Maxwell's vector wave equations to solve electric and magnetic field problems. Hence the current study applies Maxwell's equations in each node of the Finite Element model. The governing equations of the model are given by *Equation 4.11* and *Equation 4.12*.

$$\nabla \times \mu_r^{-1}(\nabla \times \mathbf{E}) - k_0^2 \left( \epsilon_r - \frac{j\sigma}{\omega\epsilon_0} \right) \mathbf{E} = 0 \quad \text{Equation 4.11}$$

$$k_0 = \omega \sqrt{\mu_0 \epsilon_0} \quad \text{Equation 4.12}$$

where  $\mu, \epsilon, \sigma, \omega, k, E$  are permeability, permittivity, conductivity, angular frequency, wave number and electric field amplitude respectively. In this study, it is assumed that  $\mu_r^{-1} = 1$ ,  $\sigma = 0$ ,  $\epsilon_r = n^2$  with  $n$  being the refractive index of the material.

Maxwell's equations have been solved for each sub domain which consists of different but linear refractive indices. Hence *Equation 4.11* converts to the equation:

$$\nabla \times (\nabla \times \mathbf{E}) - k_0^2 n^2 \mathbf{E} = 0 \quad \text{Equation 4.13}$$

According to *Equation 4.13*, the refractive index in each domain has a real value, i.e. there is no electromagnetic loss in the subdomains. This study has been performed for a *TE* polarized wave, and hence  $\mathbf{E}_x$  and  $\mathbf{E}_y$  become zero throughout the geometry and only  $\mathbf{E}_z$  is needed to solve for  $\mathbf{E}_z$  which can be achieved by solving for the out of plane vector. As shown in the physical structure (Figure 4.15), the model domain is a combination of 7 subdomains. Therefore, it is necessary to introduce proper boundary conditions to complete the mathematical model.

### c) Boundary conditions

As mentioned in Section 4.5.1 (b), the mathematical model cannot be completed without boundary conditions. It is necessary as well as critical for any computer simulation. There may be several boundary conditions existing; however, they can be mainly categorized into two categories such as common boundary conditions and unique boundary conditions. Introduction of boundary conditions provides exact formulations of equations and the correct solution for the chosen computational methods, and the selection of boundary conditions is discussed below.

There can be many common boundary conditions pertaining to Electromagnetics (EM) problems. Among them, the perfect electrical conductivity (PEC) and perfect magnetic conductivity (PMC) are the most common in many EM studies. In PEC, the material electrical conductivity is infinite, and is given by *Equation 4.14*. In contrast, in PMC, the material magnetic conductivity is infinite, and is given by *Equation 4.15*.

$$n \times \mathbf{E} = 0 \quad \text{Equation 4.14}$$

$$n \times \mathbf{H} = 0 \quad \text{Equation 4.15}$$

Having such a boundary condition in a simulation is an advantage as it speeds up the computational model by simplifying it with reduced mesh sizes. It also simplifies the material interaction and thereby reduces the calculation time. As this study was only considering electric fields, the PEC boundary condition was chosen.

Simplifying a model using common boundary conditions is not sufficient sometimes. It is also necessary to introduce unique boundary conditions like periodic boundaries to further simplify the model. These can be implemented based on a geometrical model and the type of study of which has to be included such as thermodynamics, optics, structural mechanics, etc. In this study a unit cell of a phase mask has been modelled by applying a periodic boundary condition, which is called a Floquet boundary, to the side of unit cell instead of modelling an array of unit cells, as shown in Figure 4.16. The Floquet periodicity is used to evaluate the phase shift between the boundaries along the direction of periodicity (e.g.  $x$  direction for this model) as it dictates that the solution on one side of the unit is equal to the solution on the other side multiplied by a complex value-phase factor. Applying this periodic condition reduces the model size enormously, leading to the saving of memory and computational time.

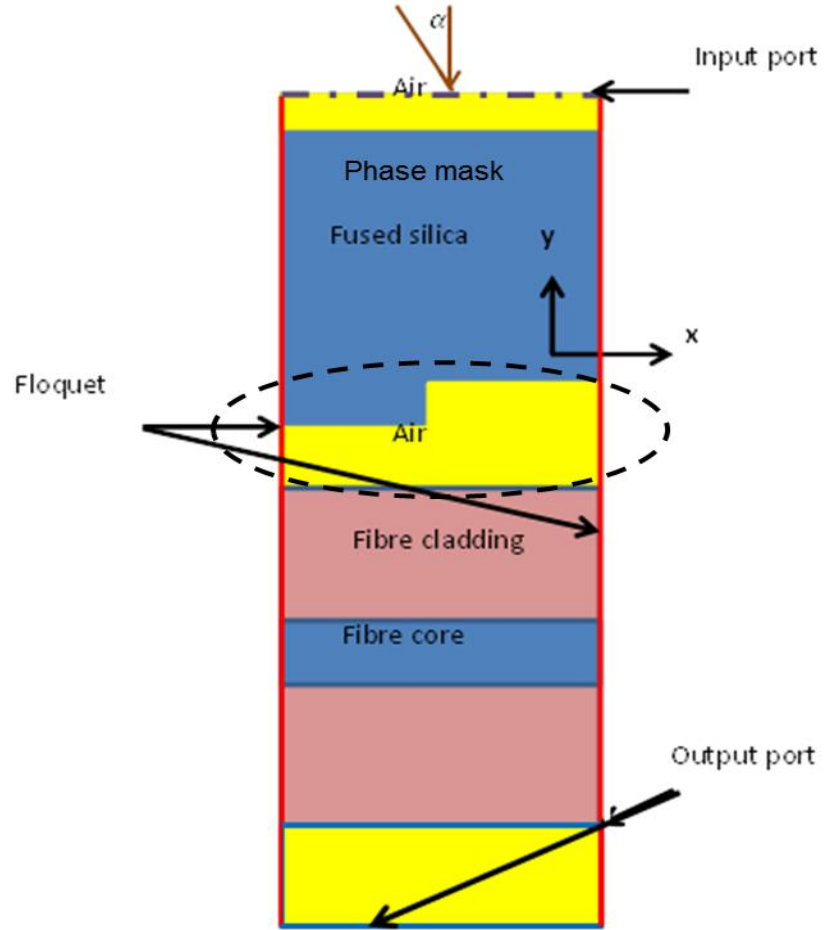


*Figure 4.16: Schematic diagram of boundary conditions on the model, inside of dashed line will be used to show the relevant mesh in Figure 4.18*

The other key component of this simulation is the introduction of a port boundary condition which allows electromagnetic energy to enter or exit from the model. As shown in Figure 4.16 the port transmits the incident wave from the air domain to fibre cladding domain which is called an output port. At the incident port and output ports, it is necessary to set the values for the parameters, as shown in Table 4.2.

Table 4.2: The calculated and defined parameters for the simulation

	Input port (IP)	Output (Exit) port (EP)
Power ( $P$ )	$P_{in}$ (in)	0 (out)
Incident angle	Alpha ( $\alpha$ )	$\beta = \arcsin(n_a \sin(\alpha)/n_b)$
Refractive index of media	$n_a$	1.4447 (RI of cladding of fibre- $n_b$ )
Port type	Periodic	Periodic
Operating frequency	$f_0 = \frac{\text{velocity of light } (c)}{\text{wavelength } (\lambda)}$	$f_0 = \frac{\text{velocity of light } (c)}{\text{wavelength } (\lambda)}$
Magnitude of the electric field	$ E_z  = \sqrt{2 \times \frac{I_0}{n c \epsilon_0}},$ $ E_x  = 0,  E_y  = 0$	$ E_z  = \sqrt{2 \times \frac{I_0}{n c \epsilon_0}},$ $ E_x  = 0,  E_y  = 0$

Where 'n' is the refractive index of each medium which is used to calculate magnitude of the electric field in Table 4.2 and  $I_0$  is the input laser intensity which is given by

$$I_0 = \frac{P_{in}}{\pi \times r_b^2} \quad \text{Equation 4.16}$$

where  $r_b$  is the beam radius of the input laser beam, and given by

$$r_b = P_{in}/(\pi \times \theta \times 0.5) \quad \text{Equation 4.17}$$

As the port only considers the input power and directions of the wave propagation, it is not compulsory to calculate the magnitude of the electric field  $|E_z|$ . Hence, any arbitrary value can be used in  $|E_z|$  while the other two are zero.

The next step is to calculate the number of diffraction orders due to the scattering effect in each port. According to the defined values given to each port, the diffraction orders can be calculated using scattering (S) parameters. S-parameters are the coefficients of a scattering matrix which originates from transmission line theory. They are used to formulate the transformation properties in terms of transmission and reflection of electromagnetic waves and defined in terms of transmitted and reflected voltage waves. This phenomenon is widely used in RF/microwave applications as those devices involve different ports. As

these ports are connected with match loads, there is no reflection in any port. If the device consists with  $j$  ports, the S-parameters are given by

$$S = \begin{bmatrix} S_{11} & \cdots & S_{1j} \\ \vdots & \ddots & \vdots \\ S_{j1} & \cdots & S_{jj} \end{bmatrix} \quad \text{Equation 4.18}$$

The voltage reflection coefficient at port 1 is  $S_{11}$  while  $S_{21}$  gives the voltage transmission coefficient from port 1 to 2 which will be later used to calculate the power transmission coefficient of an optical fibre. Therefore, reflection and transmission at any port can be calculated using S terms. Calculation of the transformation coefficient using the above method becomes invalid for the phase mask model as it uses high frequency. Therefore, it uses electric field values instead of voltage to define the S-parameters using an eigenmode expansion of the electromagnetic field. It converts the electric field pattern on a port to a scalar complex number corresponding to voltage in transmission line theory by assuming that the electric field pattern of fundamental modes on each port are known and the fields are normalized in the port cross section with respect to the integral of power flow through it. Hence the S-parameters of input ( $S_{11}$ ) and exit port ( $S_{21}$ ), as shown in Figure 4.17, can be calculated using *Equation 4.19* and *Equation 4.20*.



Figure 4.17: Schematic diagram of S-parameter

*Equation 4.19*

$$S_{11} = \frac{\int_{\text{port1}} ((E_c - E_1) \cdot E_1^*) dA_1}{\int_{\text{port1}} (E_1 \cdot E_1^*) dA_1} \quad \text{Equation 4.19}$$

*Equation 4.20*

$$S_{21} = \frac{\int_{\text{port1}} (E_c \cdot E_2^*) dA_2}{\int_{\text{port1}} (E_2 \cdot E_2^*) dA_2} \quad \text{Equation 4.20}$$

Here  $A_1$  and  $A_2$  represent the area of each port and the computed electric field represented by  $E_c$  consists of excitation plus reflected electric field. To visualize

the resultant electric field of the interference pattern of diffraction orders in the physical domain it is necessary to define the mesh through the domain properly.

**d) Finite Element Analysis**

Meshing of any structure depends on the shape of the physical structure, behaviour of their boundaries and the physics being applied. Therefore, care has to be taken to mesh a structure to optimise the outcome. The mesh size should be not greater than one eighth of the wavelength in the medium in order to resolve all wave details through the domain, and so a maximum triangular mesh size of one-tenth of the wavelength was stipulated. Figure 4.18 shows the part of the domain with its defining mesh in the phase change area.

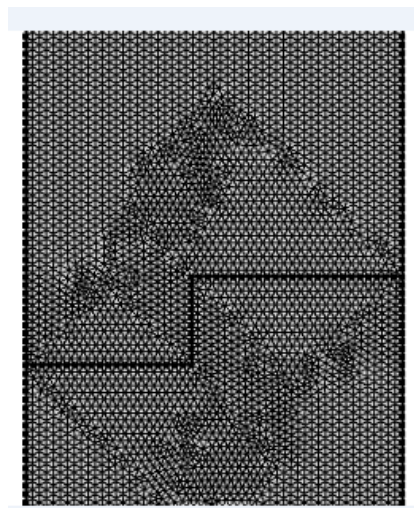


*Figure 4.18: Mesh diagram of the FEA domain around phase change area in Figure 4.16*

The analyses were performed considering the variation of the incident angle at constant frequency. Therefore, parametric analysis was used to introduce the variation of incident angle from 0 degree to 0.1 deg. It is necessary to solve a simulation by considering the size of the design model. Therefore, a solver is required to choose in terms of memory and time efficiency. For this study, PARDISO solver under direct solver was selected to speed up the simulation by reducing the solution time.

e) *Analysis (Post processing)*

The computed result from the software can be analysed to visualize the intensity variation across the physical structure using the following equations:

The intensity of a transverse electromagnetic wave,  $I$ , is given by:

$$I = \frac{E_0 B_0}{2\mu_0} \quad \text{Equation 4.21}$$

$\langle S \rangle$  is the time average Poynting vector, which is given by:

$$S = \frac{\mathbf{E} \times \mathbf{B}}{\mu_0} \quad \text{Equation 4.22}$$

$$\therefore I = \langle S \rangle \quad \text{Equation 4.23}$$

Therefore, the intensity variation across the entire domain is calculated using the time average Poynting vector which is given by

$$\langle S \rangle = \frac{1}{2} \operatorname{Re}(\mathbf{E} \times \mathbf{H}^*) \quad \text{Equation 4.24}$$

The evaluated intensity data in the core area of the fibre will be exported into the next model to analyse the spectrum of a complex fibre Bragg grating structure, as discussed in Section 2.3.1, the intensity pattern generated by the phase mask becomes “photo-imprinted” in the fibre core as refractive index changes.

#### 4.5.2 FEA ON WAVE SPECTRUM PRODUCED BY COMPLEX FBG STRUCTURE

The intensity variation exported from the proceeding simulation is used to create the complex FBG structure in SMF-28. Therefore, the refractive index variation in the core area is changed according to the following equation:

$$n = n_{core} + \alpha I \quad \text{Equation 4.25}$$

Where  $n$ ,  $n_{core}$ ,  $\alpha$  and  $I$  are refractive index value of core, initial refractive index value of SMF-28, intensity modulation factor and normalized intensity produced by the phase mask, respectively. Though some studies were conducted

considering saturation effect due intensity with time, this study was carried out without it, as it produces similar results (Kouskousis, 2009).

The theory of a FBG spectrum was discussed in Section 2.4.5 together with the analysis result of phase mask and FBG spectrum. However, it is necessary to create the physical domain of the optical fibre to simulate the FBG spectrum; hence, it is given a detailed description below.

### **(a) Physical domain of SMF28**

The model is built up using the same version of the wave optics module in COMSOL. A 2-D cross section of SMF28 can be modelled using the parameters shown in Table 2.1 and assuming that the FBG consists of 1000-unit cell of gratings along the core area of the optical fibre, as shown in Figure 4.19. It also shows the parameters considered for the modelling of the physical structure.

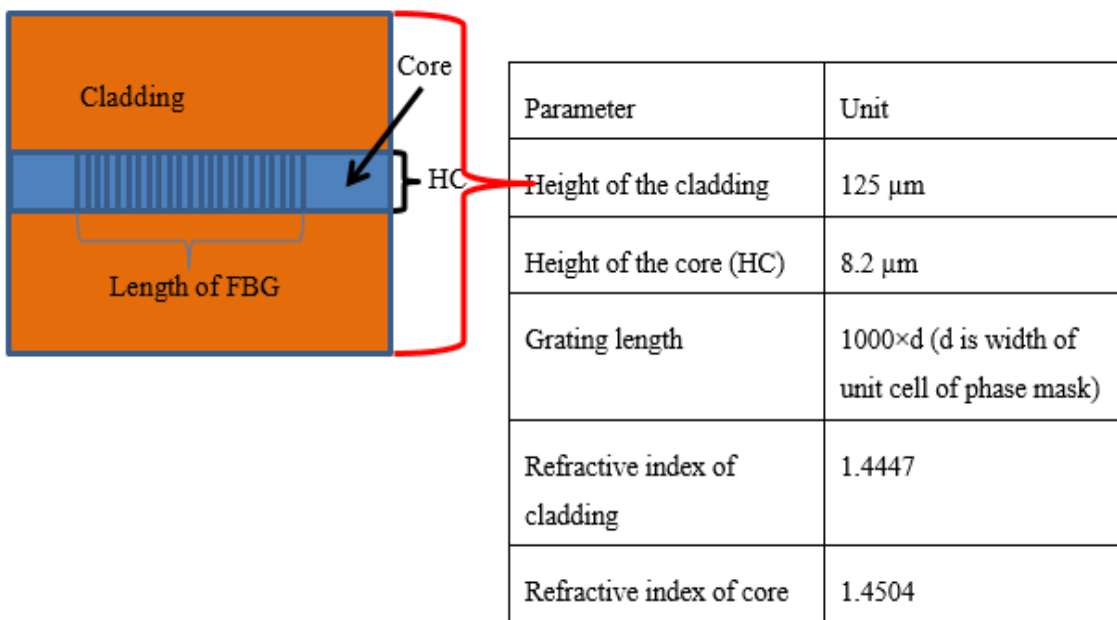


*Figure 4.19: Schematic diagram of FBG structure in SMF-28, and parameter values used*

### **(b) Mathematical model and boundary conditions**

The same mathematical equations for electromagnetic wave propagation mentioned before (*Equation 4.19* and *Equation 4.20*) will be used to evaluate the wave propagation in each domain. Each domain has real refractive index values; therefore, there is no electromagnetic loss in the domains. In the physical domains, light guidance through the structure is introduced by port boundary

conditions. An optical fibre can guide a light beam from one place to another along its core axis satisfying total internal reflection. Therefore, the wave propagating in the structure satisfies port boundary conditions as it allows a wave to propagate through from one end (input) to other end (output) of any structure as shown in Figure 4.20. The same port boundary condition is used to evaluate the effective mode indices by selecting a numeric port condition. Hence the expected Bragg wavelength is calculated to introduce the operating frequency. Once the operating frequency and effective refractive index are known the frequency range is defined to visualize its spectrum using a parametric sweep under study node together with frequency domain study. (Parametric sweep is used when a set of frequencies has to be analysed instead of a single frequency).

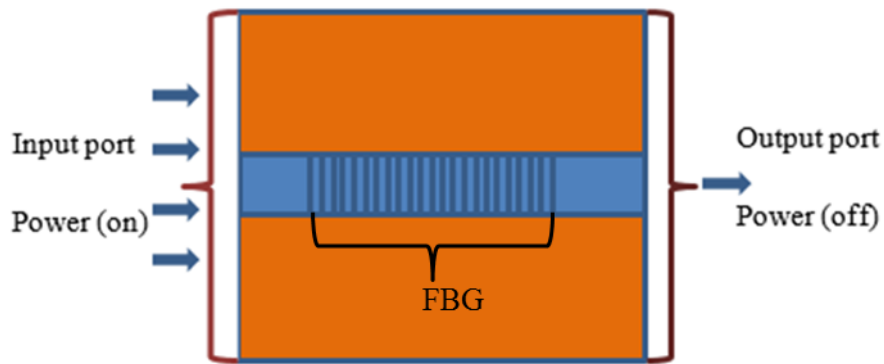


*Figure 4.20: Diagram of boundary conditions for light propagation through a FBG*

### (c) FEA of wave spectrum analysis

The meshing technique for the above structure is completely different to the previous model as the core consists of a number of periodic unit cells in the area of the FBG. Although the combined unit cells are periodic, the material variation of the unit cell is complex. The mapped mesh is selected in order to visualize the complex structure and obtain the reflection spectra. Under mapped mesh, a distribution function is selected to define the mesh along the boundaries and avoid unnecessary mesh due to the large number of boundaries. Therefore 20 mesh elements were defined per grating period along the x-direction and 82 mesh elements (height of the core  $\times 10$ ) along the height of the core in each unit cell. As the wave propagates through the core area, a similar number of meshes accounts for the cladding area. The mesh distribution in the cladding area and core of two-unit cells are shown in Figure 4.21.

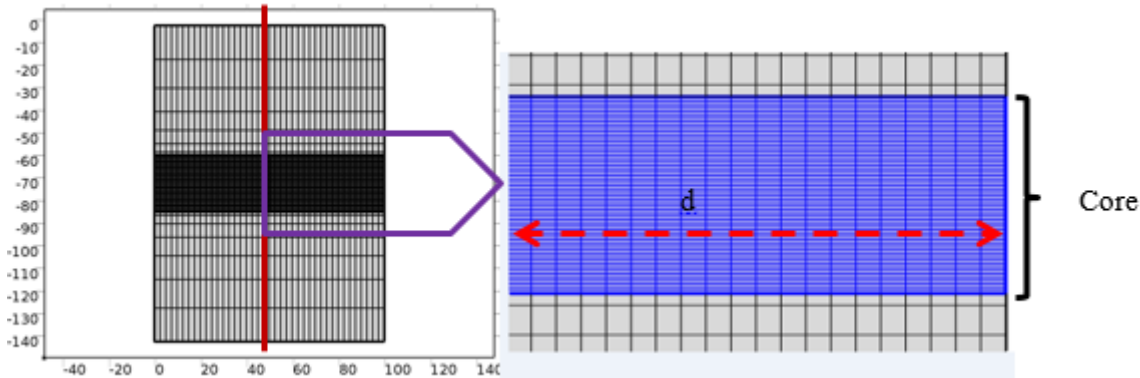


Figure 4.21: Mesh diagram of optical fibre

The frequency domain analysis performs a boundary mode analysis for the input and output ports. A parametric sweep is performed to observe the spectrum variation along the expected Bragg wavelength ( $\lambda_B$ ). PARDISO solver under direct Solver was selected to compute the simulation. Once the simulation is completed, reflectance and transmittance will be evaluated. The absolute value of S parameters is used to evaluate the spectral properties, as it allows a power flow calculation through port in light in a guiding structure, as mentioned in Section 4.5.1(c). The same approached is used to analyse the spectrum at  $(\frac{2}{3})\lambda_B$  and  $2\lambda_B$ . “As the focus was on obtaining reflectivities, calculated via power values, there was no need to explicitly determine the z-component of electrical and magnetic fields”.

## 4.6 FFT ANALYSIS OF THE DIFFRACTED DISTRIBUTION INTENSITY OF HIGHER ORDER PHASE MASK AND FEA OF REFLECTION SPECTRA AT DIFFERENT WAVELENGTHS

### 4.6.1 NORMAL INCIDENCE OF THE LIGHT ON PHASE MASK

The main focus on this section is to present the modelled intensity variation in the fibre core and, since this produces change in refractive index, to then determine the various harmonic components existing in the refractive index profile along the fibre core, their positions and Talbot length (calculated using the intensity distribution produced by modelling the phase mask method). Thus, the modelled intensity was converted to a RI profile. The profile was used to model FBG spectra. In order to observe those harmonics and their grating periods, a 1 mm FBG length was considered for analysis which was modelled by phase mask

method as mentioned in Section 2.4.2., i.e. with orders up to  $\pm 4$ . According to the fabrication method, the simulated FBG pattern shown in Figure 4.22 was obtained assuming a 1066 nm phase mask period with 1.488 index of refraction at 244 nm wavelength, and which is incident normal to the phase mask (fibre core axis placed 72.5  $\mu\text{m}$  away from the phase mask).

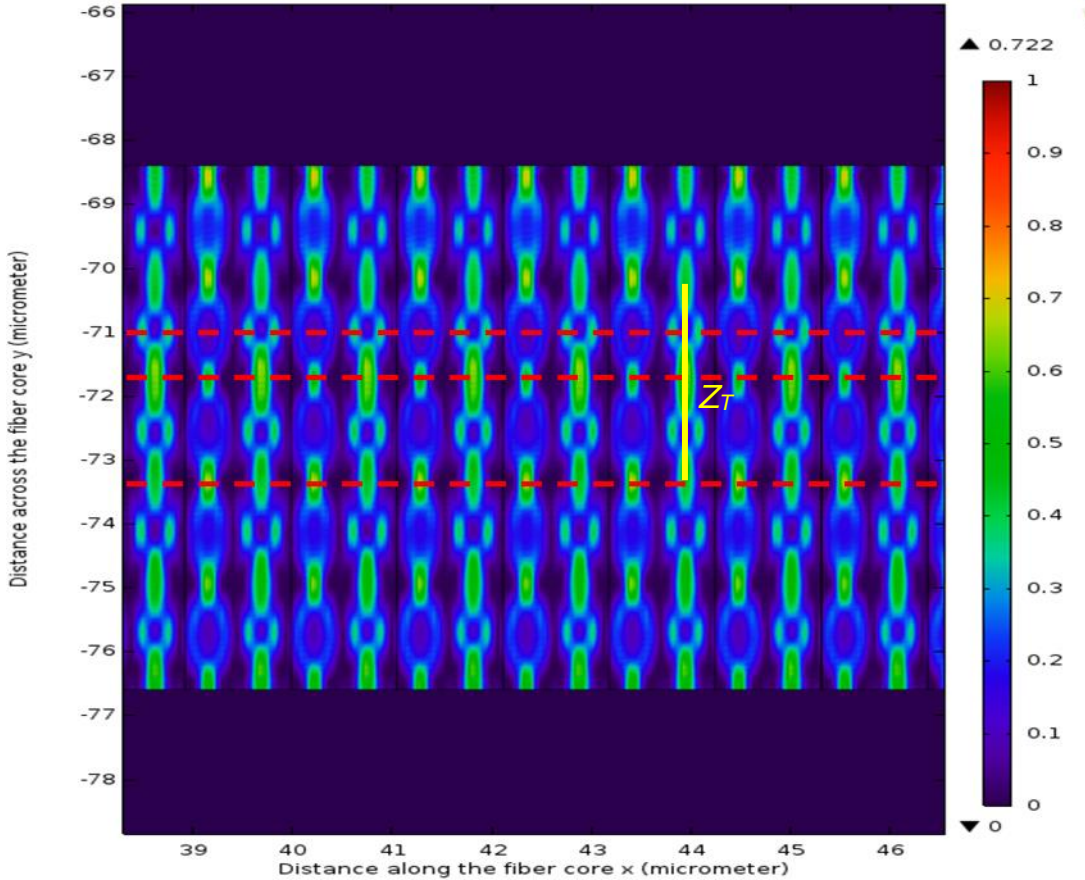


*Figure 4.22: Simulated intensity spectrum along the fibre core using phase mask method (red and yellow lines represent the line scans along the fibre core and Talbot length respectively)*

For analysis purposes, the intensity distribution produced in a  $10 \mu\text{m} \times 1000 \mu\text{m}$  region was considered in a fibre core in which the unit pixel size of 0.0076  $\mu\text{m}$ . This, as expected, is a complex structure as discussed in Section 2.4.2. Analysis of this structure in Figure 4.22 was undertaken in a fashion similar to (Kouskousis et al., 2013). To obtain the harmonic components and grating periods associated with the intensity distribution fast a Fourier transform (FFT) was performed by extracting line profiles of intensity distributions along the fibre core x, for 3 values of y, namely -71, -71.75 and -73.35  $\mu\text{m}$  as shown in Figure 4.22 (dashed lines in red colour). These intensity profiles are shown in Figure 4.23, Figure 4.25 and

Figure 4.27 and the corresponding FFT results are given in Figure 4.24, Figure 4.26 and Figure 4.28.

#### 4.6.2 FFT ANALYSIS AT DIFFERENT POSITION OF INTENSITY VARIATION ALONG THE CORE OF THE FIBRE

##### A- (I) Intensity variation at -71.00 $\mu\text{m}$

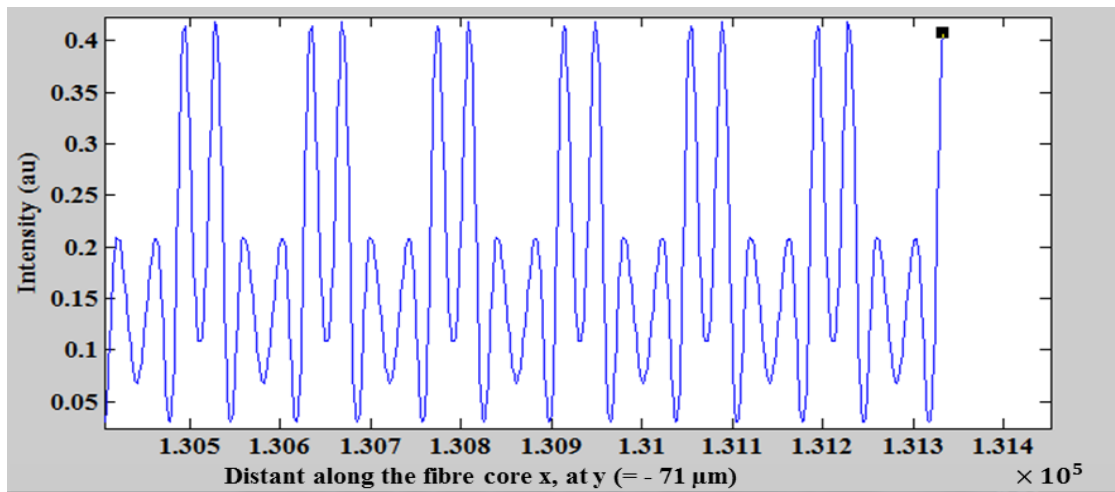


Figure 4.23: Line profile of intensity distribution at -71.00  $\mu\text{m}$  along the fibre core

##### A- (II) FFT analysis at -71.00 $\mu\text{m}$

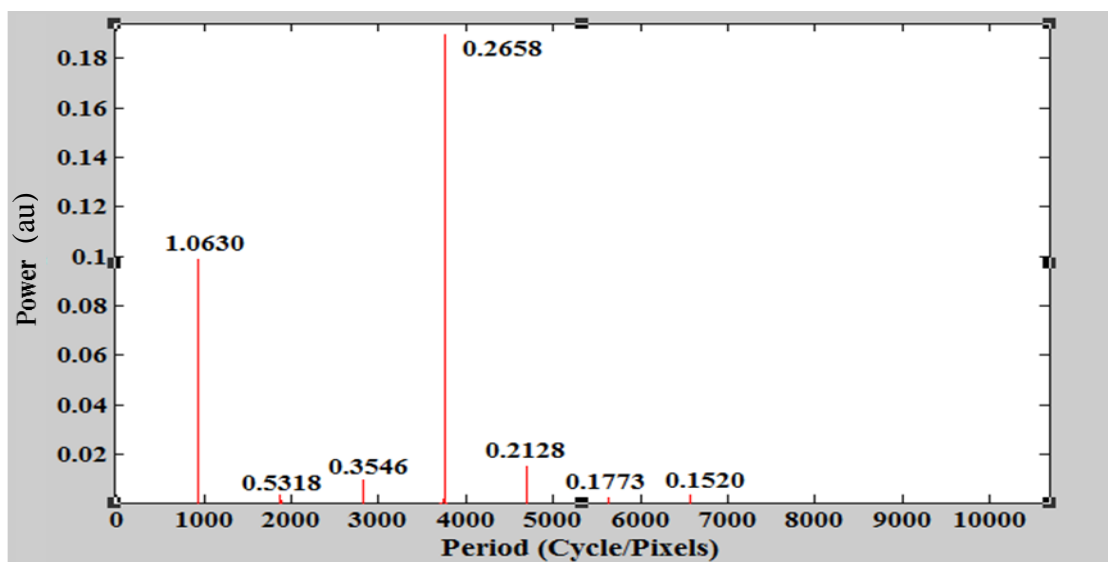


Figure 4.24: Evaluated harmonics using FFT for intensity distribution of Figure 4.23, i.e. line scan at -71.00  $\mu\text{m}$

**B- (I)** Intensity variation at -71.75  $\mu$ m

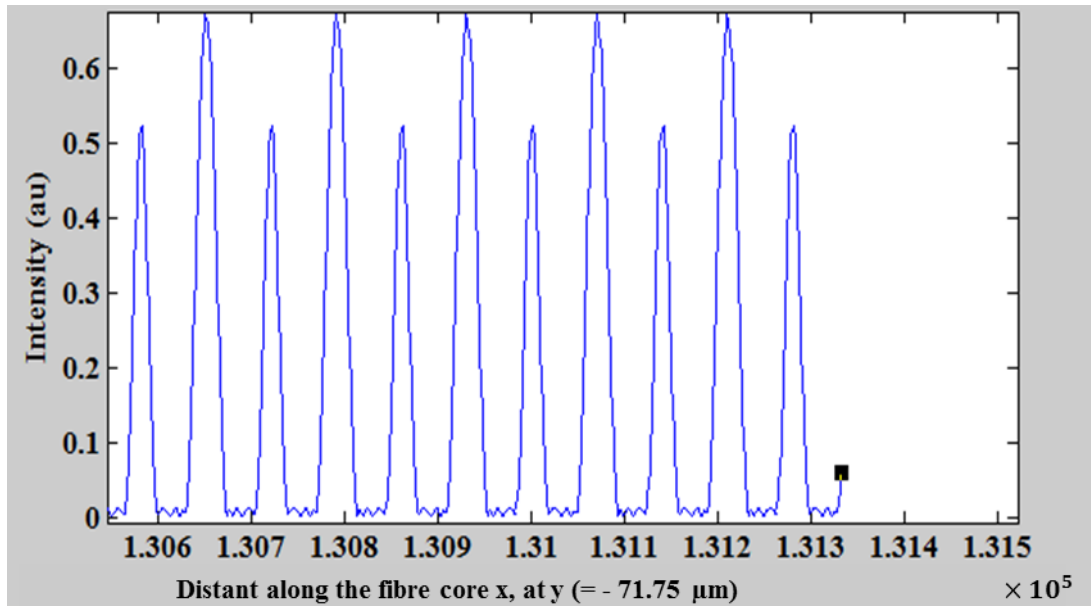


Figure 4.25: Line profile of intensity distribution at -71.75  $\mu$ m along the fibre core

**B- (II)** FFT analysis at -71.75  $\mu$ m

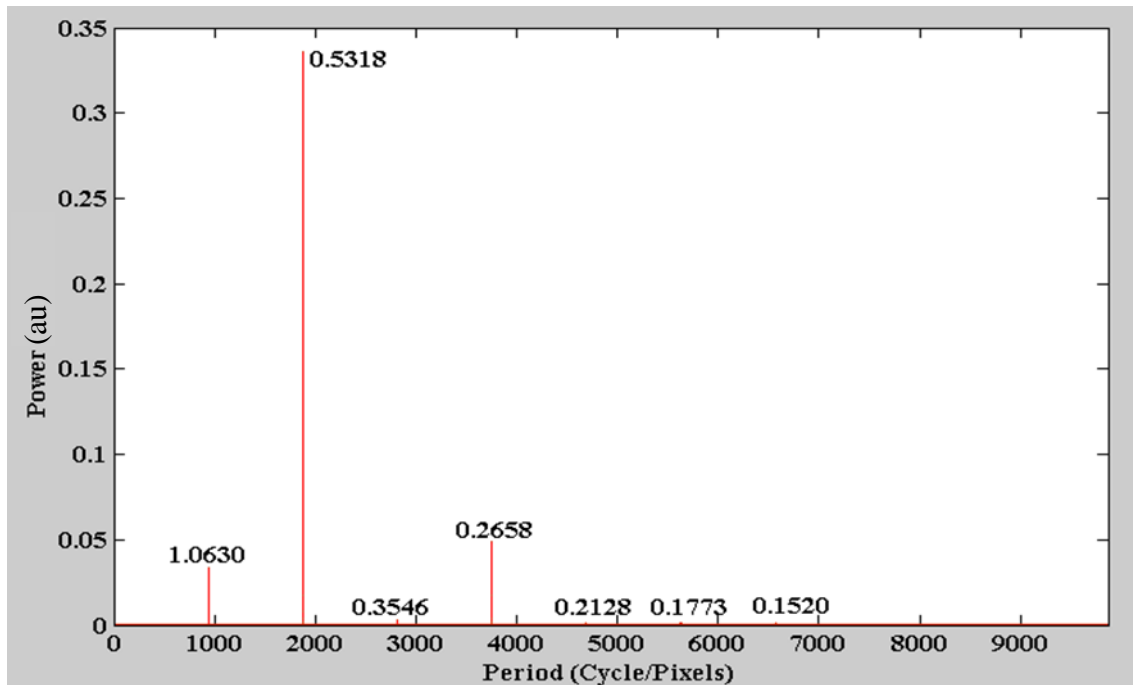


Figure 4.26: Evaluated harmonics using FFT for intensity distribution of Figure 4.25 i.e. line scan at -71.75  $\mu$ m

**C- (I) Intensity at -73.35  $\mu$ m**

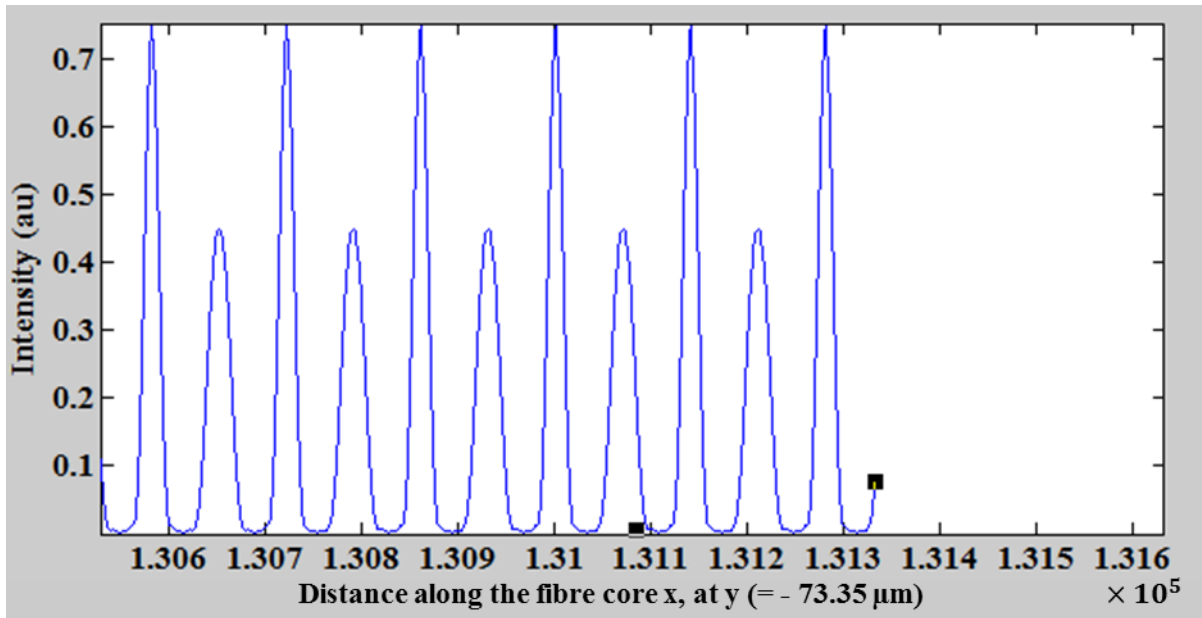


Figure 4.27: Line profile of intensity distribution at -73.35  $\mu$ m along the fibre core

**C- (II) FFT analysis at -73.35  $\mu$ m**

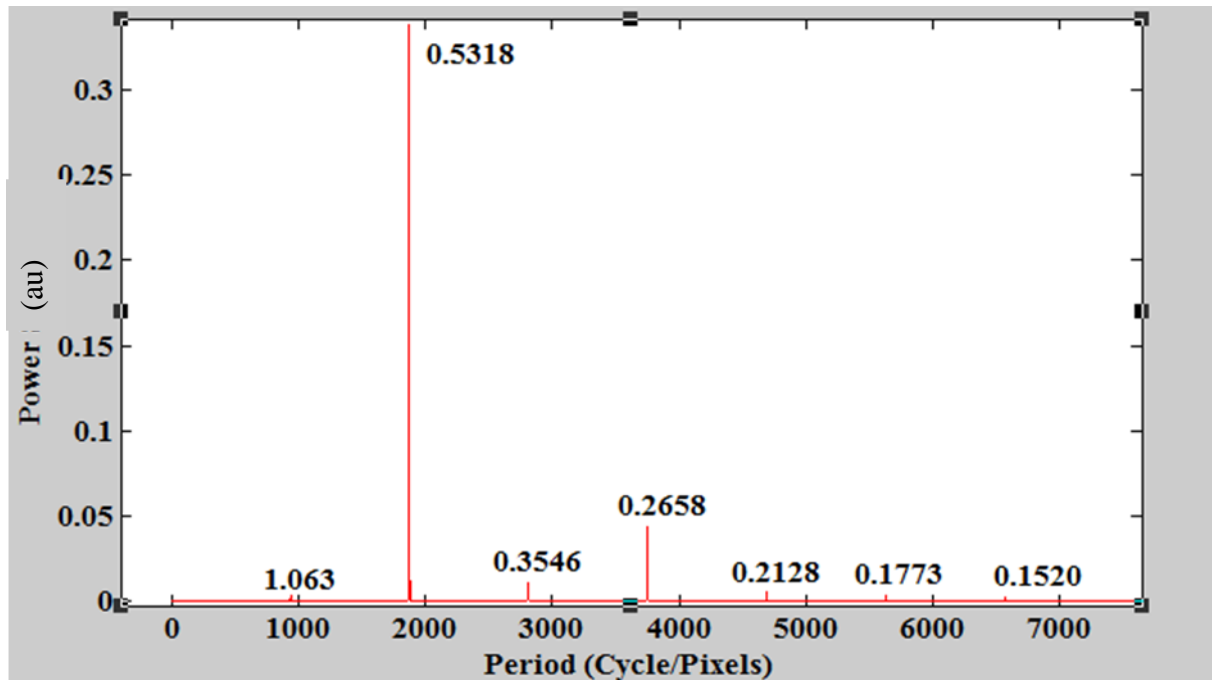


Figure 4.28: Evaluated harmonics using FFT for intensity distribution of Figure 4.27, i.e. line scan at -73.35  $\mu$ m

According to all of these FFT analyses, the line scans indicated periodicities of  $1.063 \pm 0.0038 \mu\text{m}$ ,  $0.5318 \pm 0.0038 \mu\text{m}$ ,  $0.3546 \pm 0.0038 \mu\text{m}$ ,  $0.2658 \pm 0.0038 \mu\text{m}$ ,  $0.2128 \pm 0.0038 \mu\text{m}$ ,  $0.1773 \pm 0.0038 \mu\text{m}$  and  $0.1520 \pm 0.0038 \mu\text{m}$ .

Therefore, the expected harmonics and their associated wavelengths were calculated using *Equation 2.10*, and are given in Table 4.3. The resultant strengths related to the line scans are recorded in Table 4.4.

*Table 4.3: Results of spectral components of SMF-28 for simulated FBG patterns: evaluated grating periods using FFT analysis and their harmonics, fraction of period compare to the phase mask period, calculated wavelength using Equation 2.10 and ratio of calculated wavelength to Bragg wavelength*

Harmonic m	Periods in x, FFT analysis ( $\pm 0.0038\mu\text{m}$ )	Fraction of phase mask period ( $1.066\mu\text{m}$ )	Calculated wavelength ( $\mu\text{m}$ )	Calculated wavelength/ Bragg wavelength
1	1.0630	~1	$3.0806 \pm 0.0110$	2.00
2	0.5318	~(1/2)	$1.5412 \pm 0.0055$	1.00
3	0.3546	~(1/3)	$1.0276 \pm 0.0037$	0.67
4	0.2658	~(1/4)	$0.7703 \pm 0.0028$	0.50
5	0.2128	~(1/5)	$0.6167 \pm 0.0022$	0.40
6	0.1773	~(1/6)	$0.5138 \pm 0.0018$	0.33
7	0.1520	~(1/7)	$0.4405 \pm 0.0016$	0.29

*Table 4.4: Results of diffracted efficiency of harmonics for different line scans and the expected efficiencies according to the manufacturer information*

Harmonic m	FFT strength (%) at -71 $\mu\text{m}$	FFT strength (%) at -71.75 $\mu\text{m}$	FFT strength (%) at -73.35 $\mu\text{m}$
1	9.86	3.33	0.03
2	0.35	33.62	33.86
3	1.05	0.26	1.04
4	18.93	4.84	4.37
5	1.53	0.10	0.54
6	0.31	0.14	0.25
7	0.42	0.11	0.15

According to the FFT analysis, the most dominant grating period is clearly the half of the phase mask period which is produced by  $\pm 1^{\text{st}}$  orders. However, for the line scan at -71  $\mu\text{m}$ , the 1<sup>st</sup> and 4<sup>th</sup> harmonics were more dominant while 3<sup>rd</sup> and 5<sup>th</sup> gave a contribution to the diffracted pattern. At -71.75  $\mu\text{m}$ , although the 2<sup>nd</sup> harmonic was more dominant there is a significant contribution from 1<sup>st</sup> and 4<sup>th</sup> harmonics. Similarly, at -73.35  $\mu\text{m}$  the 4<sup>th</sup> harmonic gave a significant contribution to the intensity spectrum while the 2<sup>nd</sup> harmonics became more dominant. Therefore, this FFT analysis confirms the existence of other harmonics

other than those due to the phase mask when a fibre core is placed 72.5  $\mu\text{m}$  away from the phase mask in the FBG writing process. For normal FBGs, the 2<sup>nd</sup> harmonic is dominant while others are suppressed. For complex FBGs, 2<sup>nd</sup> harmonic is dominant but other orders have significant contribution to the FBG pattern. Kouskousis (2009) and Kouskousis et al. (2013) have reported significant contribution of other orders except 2<sup>nd</sup> harmonic in result with the saturation effect of 30 % and 70 %. According to the result at 30 % saturation, the contribution of zeroth order to 5<sup>th</sup> order, strength of 2<sup>nd</sup> harmonic are decreased while 1<sup>st</sup>, 3<sup>rd</sup>, 4<sup>th</sup>, 5<sup>th</sup> and 6<sup>th</sup> harmonics are significantly increased. The result of FFT analysis for FEA analysis without a saturation effect shows similar behaviour in Table 4.4. In there, 4<sup>th</sup> harmonics become more significant after 2<sup>nd</sup> harmonic.

As discussed in Section 2.4.4 diffraction pattern exhibit a repeat distance known as the Talbot length , with each pair of orders exhibiting a particular value that can be calculated using *Equation 2.15*, and these are provided in Table 4.5. Figure 4.22 exhibits a distinct periodicity of  $\sim 3 \mu\text{m}$  across the fibre core, and this Talbot length is consistent with the calculated value of  $\sim 4.88$  for beating between  $\pm 1$  and  $\pm 2$  diffraction orders (given in Table 4.5) since *Equation 2.15* refers to diffraction pattern in free space. These FEA results are in good agreement with the experimental result of Rollinson (2012) and the analytic work of Kouskousis (2009), and confirm that the  $\pm 1$  and  $\pm 2$  diffraction orders determine the Talbot length since they are the dominant orders.

*Table 4.5: Calculated Talbot length (in free space) of the diffracted pattern produced by the phase mask with period of 1.066  $\mu\text{m}$ , index of refraction of 1.488 and wavelength at 244 nm.*

Harmonic (m)	Harmonic (n)	Talbot length ( $\mu\text{m}$ )
0	1	13.77
0	2	3.38
0	3	1.45
0	4	0.77
1	2	4.48
1	3	1.62
1	4	0.82
2	3	2.55
2	4	1.00
3	4	1.66

## 4.7 SPECTRAL ANALYSIS OF FIBRE BRAGG GRATINGS PATTERNS

The main focus in this section is to show the use of the FEA generated RI pattern for a FBG pattern (based on phase mask technology) to obtain the resultant reflection spectrum of the FBG. In order to obtain the reflection spectra of the FBG pattern, FEA was developed, as mentioned in Section 4.5.2. The analysis was performed for the same FBG pattern at different wavelengths to investigate the behaviour of the simulated FBG spectra.

### a) Reflection spectrum at $\lambda_B$

For the FEA purpose, intensity spectrum (Figure 4.22) was implemented on SMF-28 was converted to an RI variation (see Figure 4.29).

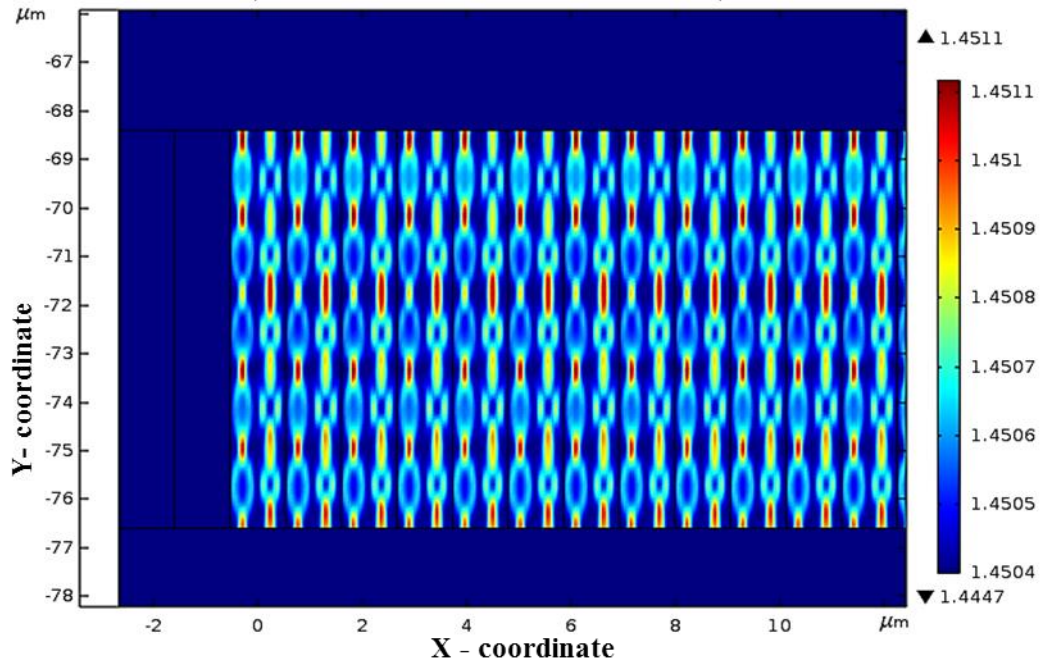


*Figure 4.29: FBG pattern was obtained using phase mask technique, the colour line represents the refractive index value of FBG pattern*

To observe the reflection spectra of FBG pattern, 1.066 mm (1000 unit cells) of grating length was considered. According to the simulation result in Figure 4.30, the Bragg peak was observed at  $1.5446 \pm 0.0010 \mu\text{m}$ . Therefore, the calculated Bragg wavelength is also in good agreement with the simulated result as it became  $1.5446 \pm 0.0014 \mu\text{m}$  which was given by the Bragg equation (*Equation 2.11*) and the FFT analysis result in Table 4.3 ( $1.5412 \pm 0.0055$ ). The resultant reflectivity of the Bragg peak from simulation is  $0.0769 \pm 0.0025$  while the

calculated reflectivity using *Equation 2.20* became 0.0776 which shows good agreement between theoretical and simulation results. The calculated normalized frequency is 2.1424 and it's under single mode operation as  $V$  is less than 2.4. It also showed by the existence of a single effective refractive index of 1.449.

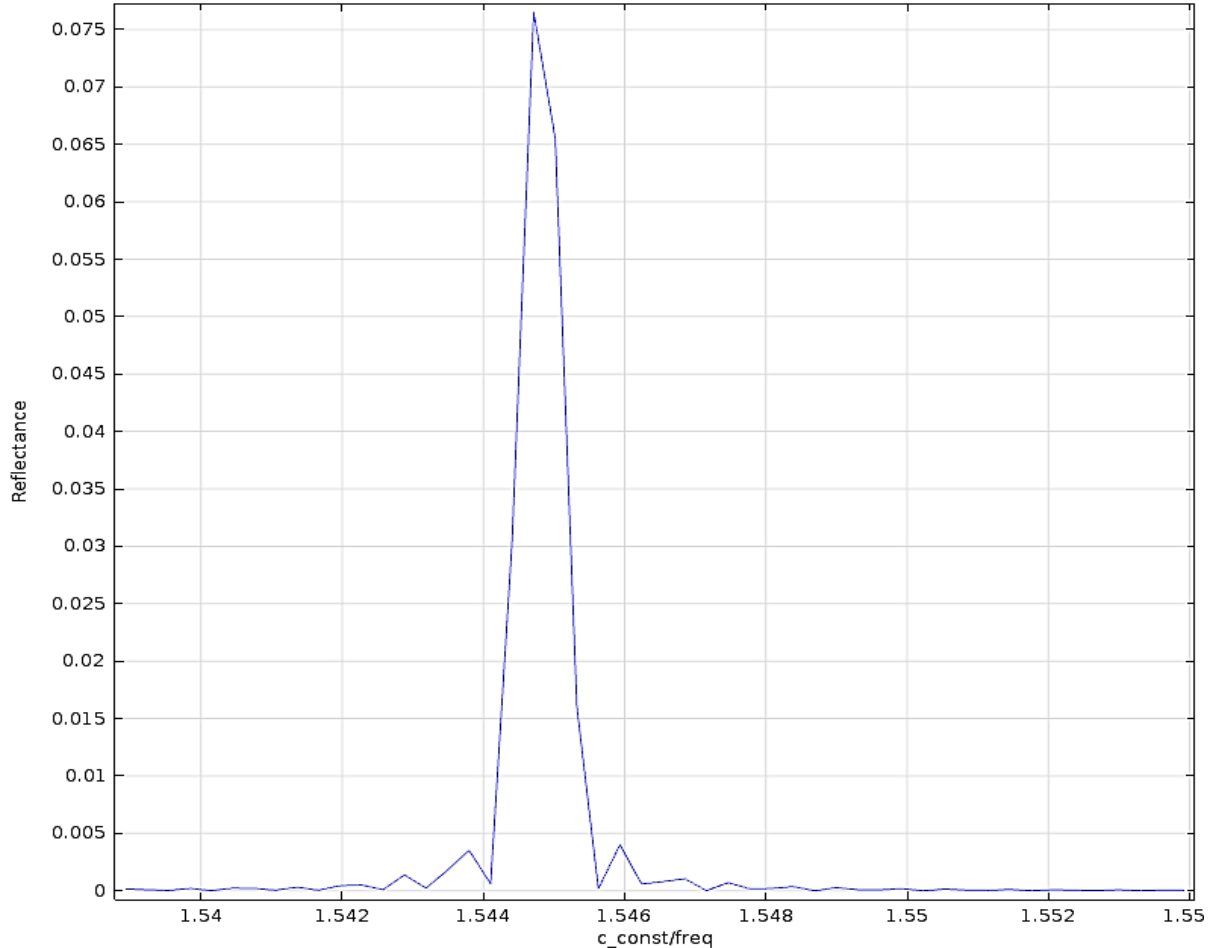


*Figure 4.30: Simulated FBG reflection spectrum at  $\lambda_B$  for complex FBG pattern of Figure 4.29, obtained by phase mask method*

**b)** Reflection spectrum at  $2\lambda_B$

The same parameters in Table 2.1 were used to simulate the reflection spectrum of the FBG structure (Figure 4.29) when the operating wavelength is at  $2\lambda_B$ . The resultant spectrum of FEA is shown in Figure 4.31. According to the results, the reflection peak is observed at wavelength of  $3.0861 \pm 0.0010 \mu\text{m}$  in simulation is in good agreement with the calculated result of  $3.0861 \pm 0.0029 \mu\text{m}$  using *Equation 2.11* and value  $3.0806 \pm 0.0110 \mu\text{m}$  which is given by FFT analysis (Table 4.3). The normalized frequency  $V$  is 1.0723 which is less than 2.4, hence at the operating wavelength of  $2\lambda_B$ , the optical fibre behaves as a single mode

fibre. It is also confirmed by the effective index of refraction ( $n_{eff}$ ) produced by the simulation. There is only one value for  $n_{eff}$  and it is 1.4475. According to Figure 4.31, the resultant reflectance value is  $0.00032 \pm 0.00001$  and it is in a good agreement with the calculated value 0.00034 using *Equation 2.20*.

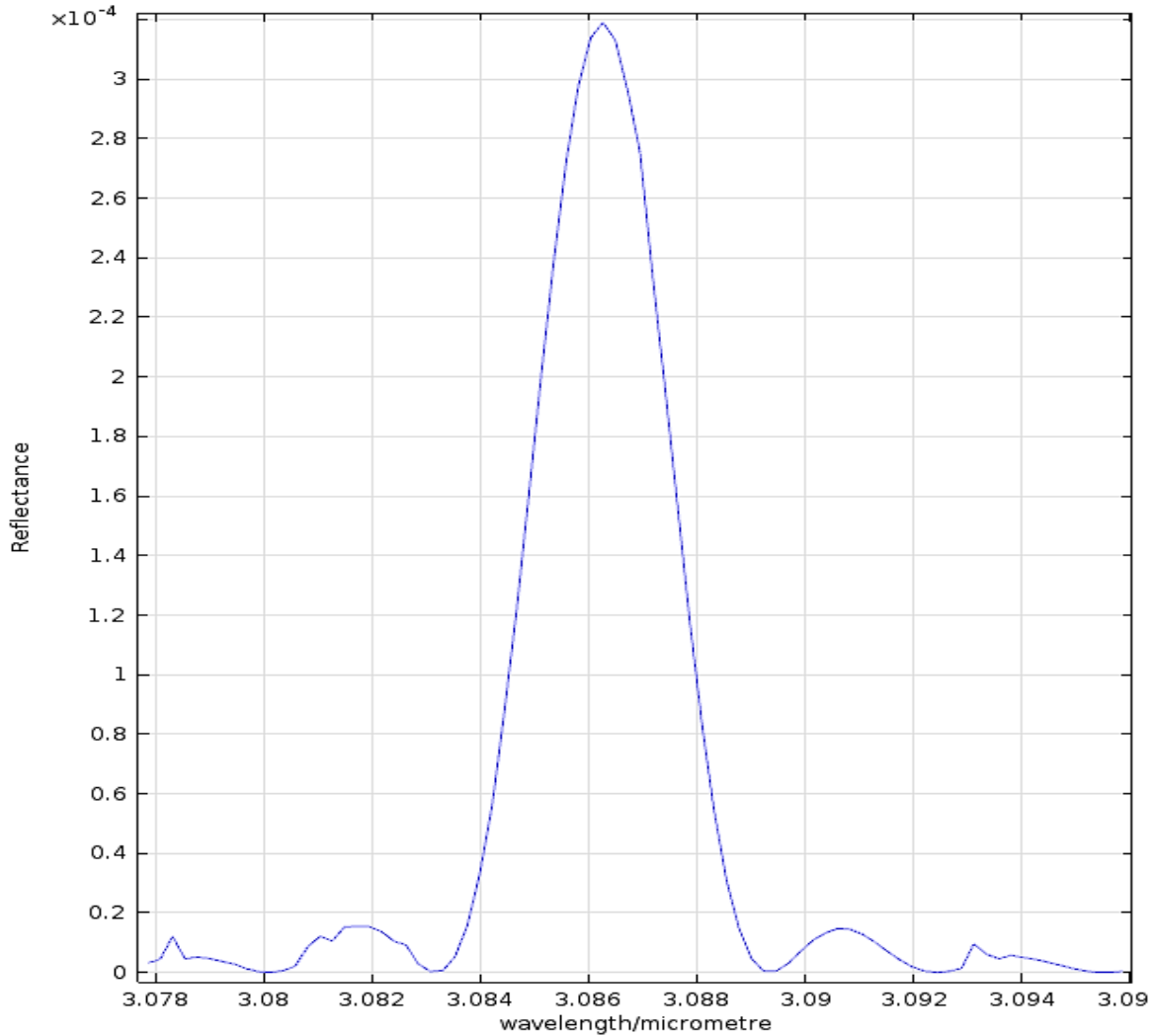


Figure 4.31: Simulated FBG reflection spectrum at  $2\lambda_B$ , obtained for complex FBG pattern

### c) Reflection spectrum at $\frac{2}{3}\lambda_B$

The same parameters are in Table 2.1 were used to simulate the reflection spectrum of FBG structure (Figure 4.29) when the operating wavelength is at  $(\frac{2}{3})\lambda_B$ . The resultant spectrum obtained via FEA is shown in Figure 4.32. According to the results, the reflection peaks are observed at wavelengths of  $1.0298 \pm 0.0010$ ,  $1.0284 \pm 0.0010$  and  $1.0265 \pm 0.0010$   $\mu\text{m}$  which is in good agreement with the calculated results of  $1.0301 \pm 0.0010$ ,  $1.0286 \pm 0.0010$  and

$1.0267 \pm 0.0010 \mu\text{m}$  using *Equation 2.11*. The calculated normalized frequency  $V$  is 3.2123 which is higher than 2.4, hence at the operating wavelength of  $(\frac{2}{3})\lambda_B$ , the optical fibre behaves as a multimode fibre. It is also confirmed by the number of effective indices of refraction ( $n_{\text{eff}}$ ) produced by the simulation. There are three strongest values for  $n_{\text{eff}}$  and they are 1.4496, 1.4474 and 1.44473. According to Figure 2.4, there ought to be 4 effective mode indices for  $(\frac{2}{3})\lambda_B$ , except that  $\text{HE}_{21}$  and  $\text{TM}_{01}$  have the same index value. Likewise, the simulation provided only 3 effective mode indices, confirming that 2 of the modes have the same index.

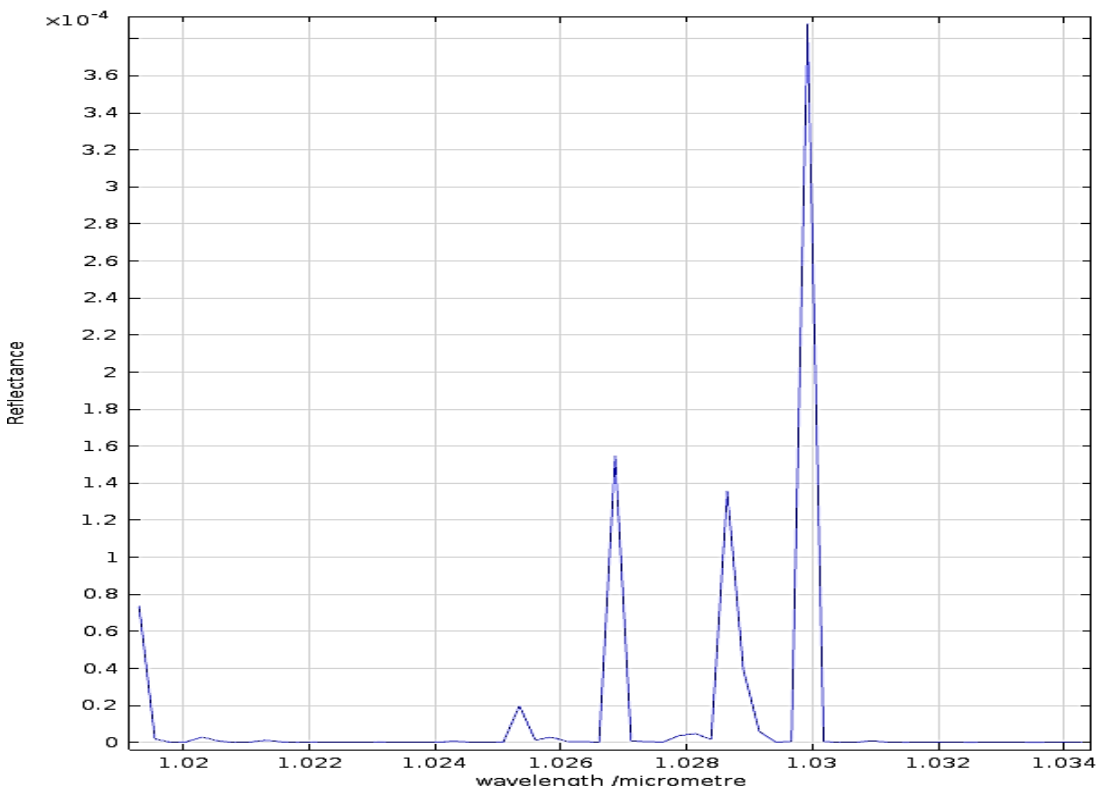


Figure 4.32: Resultant FBG reflection spectrum at  $(\frac{2}{3})\lambda_B$  by complex FBG pattern

The experiments conducted for type I and IIA FBGs by Rollinson (2012) observed 2 transmission peaks at 1025.6 and 1026.5 nm for type I and 3 transmission peaks for type IIA FBGs at 1025.9, 1027.3 and 1028.5 nm (at  $(\frac{2}{3})\lambda_B$ ). The results obtained at  $(\frac{2}{3})\lambda_B$  by FEA analysis is in good agreement with the experimental results.

## 4.8 SUMMARY

This chapter discussed details of FEA theory, its history and benefits of using it for computational modelling. This chapter mainly focused on introducing Finite Element Analysis on fibre modes, FBG structure and its spectra.

FEA were first used to confirm the well-known behaviour of optical fibre; the simulation was performed at different wavelengths to observe the number of modes that could arise. For wavelengths at  $\lambda_B$  and  $2\lambda_B$  ( $V < 2.405$ ), the analysis results show the only propagating mode is  $HE_{11}$  and so it is a single mode fibre. However, under the same condition applied to wavelength at  $(\frac{2}{3})\lambda_B$  ( $V > 2.405$ ), the results produced four modes, i.e. there is multimode behaviour. The analysis results are also in good agreement with literature findings (Figure 2.3 and Figure 2.4) which show the mode scenarios at different normalized frequency ( $V$ ). In every FEA simulation, effective mode index values were in between core and cladding refractive index values. Simulation results suggested that the light wave is more confined in the core region in situations where the effective mode index value is closer to the core refractive index value (1.4504).

New computational models were developed to create FBG structures and their spectra. To develop a computational model, first, the FBG structure was developed by considering the manufacturing process. It considered the phase mask method for FBG fabrication and developed a simple 2-D tool to create the same scenario as the manufacturing process. For the developed model, as shown in Fig 4.15, a small air gap was assumed in between the phase mask structure and the optical fibre to optimise the interference of a number of harmonics whilst avoiding possible damage to the phase mask structure by contact with the optical fibre. A gap of 10  $\mu\text{m}$  was used in all calculations (as used in typical experimental arrangements). The effect of varying the gap size was investigated by Kouskousis et al. (2013) who simulated the interference pattern for different air gaps. They showed that if the gap is bigger, only the  $+/-1$  order harmonics occur and the resultant grating has a single Bragg wavelength, but this may be weakened due to the limited coherence length of the writing beam. If the gap is small (but non-zero), a complex RI distribution results which produces Bragg reflections at multiple wavelengths (Rollinson et al., 2005).

The resultant spectrum plots were produced by the software depending on the FEA developed. Resultant spectra of simulation are not smooth as the theoretical results depend on the mesh size and wavelength spacing specified. However, the results given by the simulation agree very well with the theoretical results. The diagrams were plotted by the software for the limited number of values thereby leading to patterns, such as in 4.30, that are not smooth.

The developed model is able to create various FBG structures such as first order gratings, complex grating and a tilted grating as shown in Figure 4.33 (simulated by using COMSOL) by changing dimensions of phase mask and incident angles. The fringe pattern on a unit cell produced by the phase mask was imprinted on fibre structure by importing and using an array method to create the same pattern on the fibre. Using this method, the length of the FBG can be defined and controlled for the required purposes.

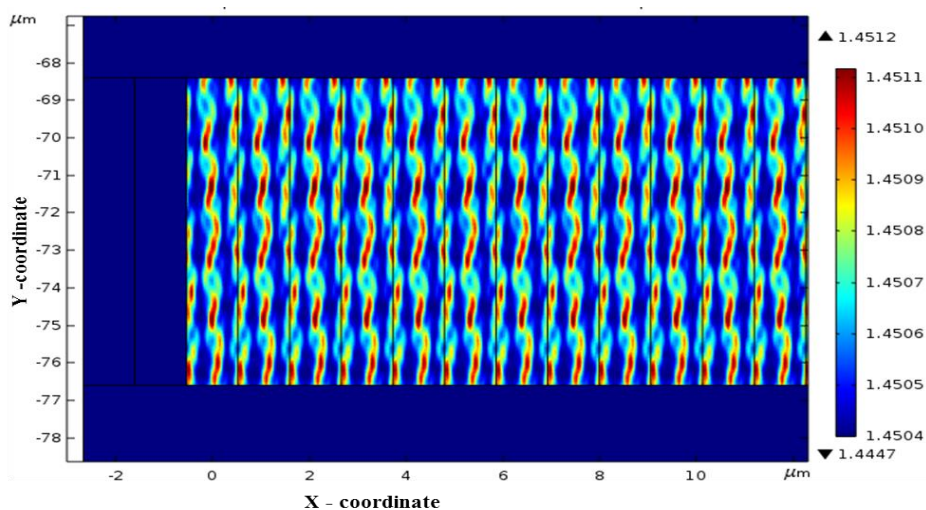


*Figure 4.33: Tilted FBG pattern obtained by phase mask method*

The chapter provides analyses of complex grating structure via a FFT analysis to find the number of harmonics, its grating period and expected efficiencies etc. The analysis identified that the complex structure could be used to analyse the spectrum and compared this with the number of modes observed at different wavelengths. The results of simulated spectra were observed and identified and shown that they were in good agreement with the results of the number of modes observed in a single mode fibre by FEA analysis.

In the literature, several analytical and experimental analyses have been reported for interference pattern associated with complex Bragg grating structures (Dyer, Farley & Giedl, 1995; Kouskousis et al., 2013; Mills et al., 2000). Tarnowski & Urbanczyk (2013) modelled wave spectrum to explain effect of tilt waveguide on multiple order phase mask. In that work, the interference pattern was produced using a numerical simulation that was converted into a refractive index modulation within the core of the fibre. The reflected spectrum of the FBG inscribed was analysed using COMSOL. Recent studies of apodized FBG formation using the phase mask method with varying duty cycle using numerical methods shows the effect of positioning of the fibre core on reflection efficiencies (Osuch & Jaroszewicz, 2017). In the proposed model, duty cycle and the position of the fibre can be changed easily; hence, calculated the reflection efficiencies.

The 2-D model of computational design for complex Bragg grating structure using phase mask method has not been reported as yet. Hence, this method is unique producing first order, higher order grating or tilted gratings simply adjusting its parameters and dimensions. The same model can be easily used for spectral analysis. The results produced by the study further validated the compatibility of the results with other anticipated theoretical results and reflected the advantage of a FEA model over analytical methods.

## **CHAPTER 5: Finite Element Analysis on pressure sensitivity (Computational design)**

### **5.1 OVERVIEW**

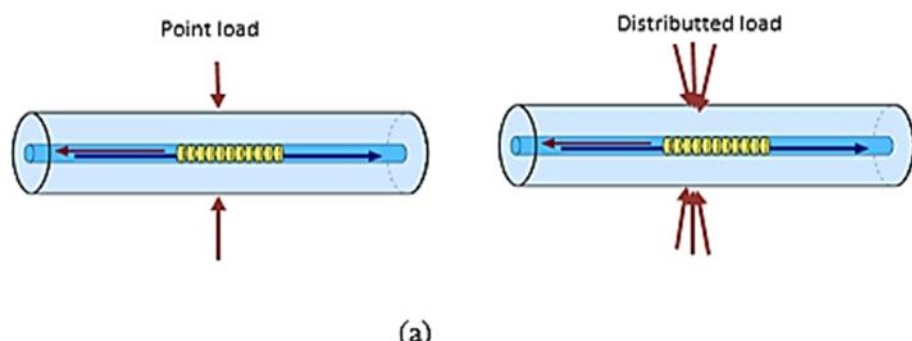
The main focus in this chapter is the use of FEA to seek solutions for existing issues with optical fibre pressure sensors as discussed in Chapter 3 including related strain sensors and identifying the potential ways to enhance their sensitivity. To achieve that Finite Element Analysis models will be introduced considering different scenarios for coating fibres with selected polymers to enhance the sensitivity. The result analysis will be compared with the limited existing literature for verification purposes. As a result, a new sensor configuration will be suggested for a low (gauge) pressure range for future use.

### **5.2 PRESSURE EXERTIONS ON FBGS**

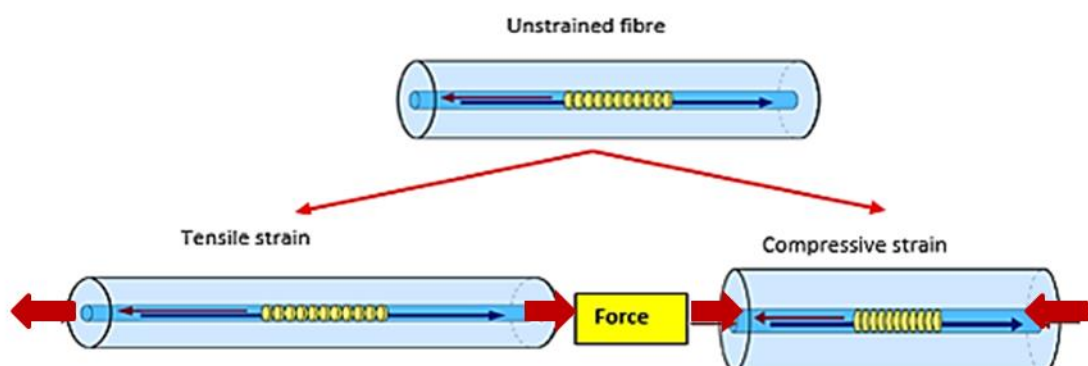
There have been many research studies for pressure sensing on fibre Bragg gratings as discussed in Chapter 3; however, most of them are only concerned with standard gratings. Although there have been many experiments on FBGs sensitivity for high pressure, as noted in that chapter, few experiments have been reported for low (0 – 200 kPa) (gauge) pressure. For example, Bal et al. (2011) have reported different responses for various FBGs and different fibre types, for up to 200 kPa. Since this work raised several questions, more research is required to understand the behaviour of complex gratings at low pressure.

Pressure and force exerted on an optical fibre can be categorised into 3 forms. They are:

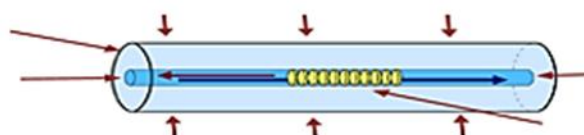
- Transverse compressive (point and distributed loading) - Figure 5.1 (a)  
(The length of the object increases while it is deformed)
- Tensile and compressive strain - Figure 5.1 (b)  
(The length of the object increases when it's under tensile force and it decreases under compressive force)
- Uniform pressure - Figure 5.1.(c)  
(The pressure exerted by a fluid at equilibrium at a given point in the same medium)



(a)



(b)



(c)

*Figure 5.1: Possible forms of pressure exertion on an optical fibre (a) Transverse compressive load, (b) Tensile and compressive strain, (c) Uniform pressure*

### 5.3 FEA ON POINT LOAD AND DISTRIBUTED LOAD

For bare FBGs, the pressure exertion due to a point load and a distributed load can be represented on a 2-D cross section, as shown in Figure 5.2.

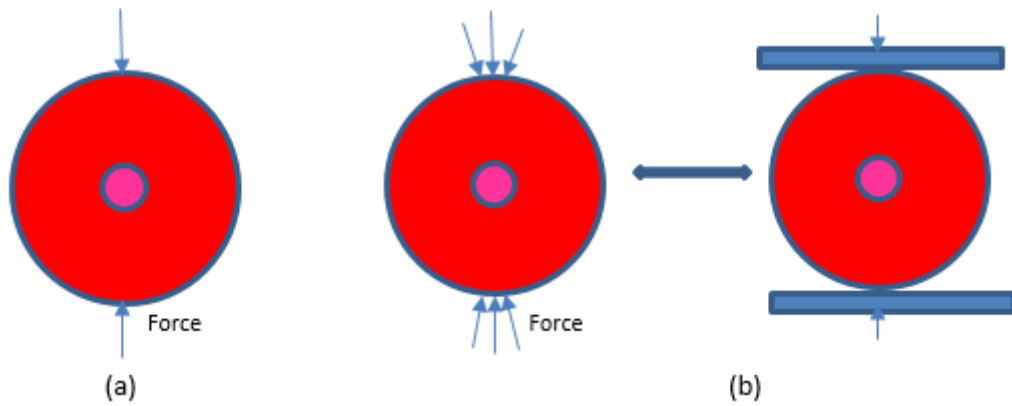


Figure 5.2: Schematic diagram of 2D cross section of point load (a) and distributed load (b) on FBG

According to Figure 5.2 (a), the cross section of a fibre exerts a point load on two sides. Strain and shape variations due to a point load are very small. Therefore, in computational modelling, plane strain was assumed, and the contact is assumed as frictionless. When a load is applied on fibre, a stress variation is created within the fibre core. Due to this stress variation, the index of refraction is changed. These refractive index changes can be calculated using *Equation 3.3* and *Equation 3.4* for the given photo-elastic constants.

### 5.3.1 FEA FOR UNIFORM PRESSURE

For a uniform pressure situation, the scenario as depicted in Figure 5.3 is considered.

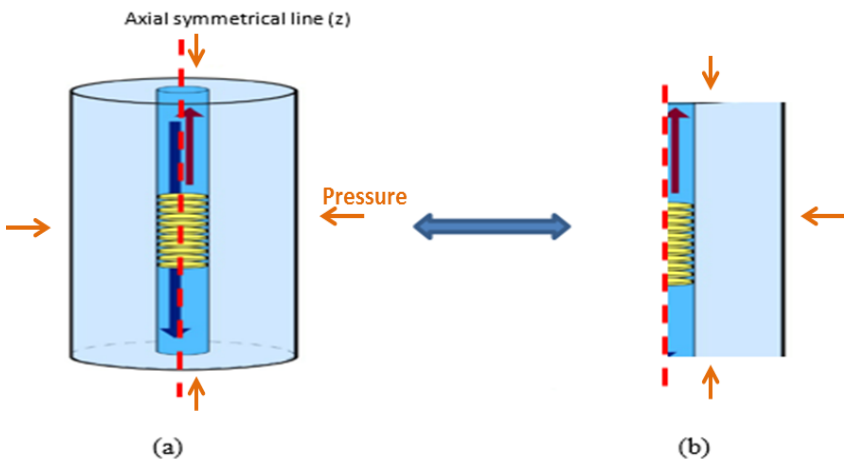


Figure 5.3: Schematic diagram of a 3-D cylindrical fibre (a) and simplified (2-D cross section) view of the same FBG due to axial symmetry (b)

For uniform pressure sensing, the cross section of a fibre (Figure 5.3 (b)) is considered for computational domain in axi-symmetric coordinates. Ideal, or

standard, gratings (Figure 2.5 in Chapter 2), are considered for simulation, and different coating materials are considered to enhance the pressure sensitivity.

### 5.3.2 PHYSICAL DOMAIN OF THE MODEL

The model was developed using the *Structural Mechanics* and *Wave Optics* module of COMSOL. The computational modelling has been undertaken by considering the real scenario of pressure exertion by an FBG as shown in Figure 5.1. Pressure sensitivity analysis using FEA methods can be obtained using 2-D or 3-D simulations. However, 3-D simulations take a long time to complete and require high RAM capacity as it solves structural mechanics and optics problems at the same time. Also, for simulation purposes, it is better to have the simplest model rather than one that is complicated. Therefore, a 2-D cross section of a FBG was considered for pressure sensitivity analysis. Although a fibre is cylindrical, previous studies have applied 2-D cross sections in Cartesian coordinates and confirmed no significant effect for the result (Prabhugoud & Peters, 2007).

For this study, the physical and material parameter of an optical fibre, SMF-28 is considered for modelling and simulations (see Table 2.2). First, a fibre without coating is considered. To simplify the simulation, a fibre end face is created considering its symmetry along the x and y directions, for point load on a FBG (see Figure 5.2 (a)). For distributed loading, the structure is created assuming the load is transferred via compact glass plates (see Figure 5.2 (b)). For uniform pressure, axi-symmetric coordinates were chosen as shown above in Figure 5.3 (b). For each case appropriate boundary conditions and constraints were chosen to perform the simulation.

### 5.3.3 MATHEMATICAL MODEL

For all cases, the mathematical model uses the *Wave Optics* and *Structural Mechanics* Modules in COMSOL version 5.3. The *Wave Optics* Module is mainly used to calculate the propagating modes in a fibre. Modelling and evaluating these modes at various wavelengths has been fully discussed in Section 4.4. However, these modes were calculated without any excess pressure. To understand the effect on a mode due to elevated pressure, it is necessary to

implement the refractive index profile in the fibre with pressure exerted. For a point load and distributed load, this has been done by using a linear stress-optical relation using the COMSOL Multiphysics module guide. A relation between stress and refractive index can be written using tensor notation as follows:

$$\begin{aligned}\Delta n_{ij} &= -B_{ijkl}S_{kl} \\ \Delta n_{ij} &= n_{ij} - n_0 I_{ij}\end{aligned}\quad \text{Equation 5.1}$$

where  $\Delta n_{ij}$ ,  $n_0$ ,  $I_{ij}$ ,  $B_{ijkl}$  and  $S_{kl}$  are the refractive index tensor, index of refraction of a stress-free material, identity tensor, stress-optical tensor and stress tensor, respectively.

*Equation 5.1* can be further simplified due to parameter symmetry where  $n_{ij}$  and  $S_{kl}$  are symmetric.  $B_{ijkl} = B_{jikl}$  and  $B_{ijkl} = B_{ijlk}$  are symmetric. Due to the reduced number of parameters, the model considers independent parameters  $B_1$  and  $B_2$  only when non-diagonal parts of  $n_{ij}$  are neglected. The simplified stress-optic relation can be given by the following equation.

$$\begin{bmatrix} \Delta n_x \\ \Delta n_y \\ \Delta n_z \end{bmatrix} = - \begin{bmatrix} B_1 & B_2 & B_2 \\ B_2 & B_1 & B_2 \\ B_2 & B_2 & B_1 \end{bmatrix} \begin{bmatrix} S_x \\ S_y \\ S_z \end{bmatrix} \quad \text{Equation 5.2}$$

When  $n_x = n_{11}$ ,  $n_y = n_{22}$ ,  $n_z = n_{33}$ ,  $S_x = S_{11}$ ,  $S_y = S_{22}$  and  $S_z = S_{33}$  the equation further translates to the following:

$$\left. \begin{array}{l} n_x = n_0 - B_1 S_x - B_2 (S_y + S_z) \\ n_y = n_0 - B_1 S_y - B_2 (S_x + S_z) \\ n_z = n_0 - B_1 S_z - B_2 (S_x + S_y) \end{array} \right\} \quad \text{Equation 5.3}$$

The tensor analysis is only performed for the domain which has an index of refraction value. The refractive index in each domain has a real value (i.e., there is no electromagnetic loss in the subdomains). The above tensor analysis will be used for mode analysis and predicts the birefringent effect under a post processing step on point load and distributed load fibres. Therefore, it is necessary to introduce the solid mechanics interface. In each model point load, distributed load and uniform pressure are introduced in different domains. In solid mechanics, the plain strain approximation is used to compute the stress variation

on the fibre. However, the plane strain simulation does not represent the real behaviour under applied load. This can be minimized by introducing generalized strain along the  $z$  direction. Assuming strain is varying linearly on the  $x$ - $y$  cross section, the out of plane strain  $\varepsilon_z$  along the  $z$  direction is implemented using this equation:

$$\varepsilon_z = e_0 + e_1 X + e_2 Y \quad \text{Equation 5.4}$$

where  $e_0, e_1$  and  $e_2$  are mathematical coefficients which are used for introducing strain  $\varepsilon_z$  with an extra degree of freedom under Global equations in COMSOL. To implement a 3-D effect, the stress-strain relationship including a thermal effect for linear isotropic material is introduced under global equations.

A relation between generalized stress-strain in three directions can be introduced into a 2-D simulation by considering *Equation 5.5*.

$$\left. \begin{aligned} S_x &= S_{11} = D_{11}(\varepsilon_x - \varepsilon_{th}) + D_{12}(\varepsilon_y - \varepsilon_{th}) + D_{13}(\varepsilon_z - \varepsilon_{th}) \\ S_y &= S_{22} = D_{12}(\varepsilon_x - \varepsilon_{th}) + D_{22}(\varepsilon_y - \varepsilon_{th}) + D_{23}(\varepsilon_z - \varepsilon_{th}) \\ S_z &= S_{33} = D_{13}(\varepsilon_x - \varepsilon_{th}) + D_{23}(\varepsilon_y - \varepsilon_{th}) + D_{33}(\varepsilon_z - \varepsilon_{th}) \end{aligned} \right\} \quad \text{Equation 5.5}$$

$$\left. \begin{aligned} \varepsilon_x &= \varepsilon_{11} = \partial u / \partial x \\ \varepsilon_y &= \varepsilon_{22} = \partial v / \partial y \end{aligned} \right\} \rightarrow \text{Strain variation along } x \text{ and } y \text{ direction}$$

$$\left. \begin{aligned} D_{11} &= D_{22} = D_{33} = E(1 - \nu) / (1 + \nu)(1 - 2\nu) \\ D_{12} &= D_{23} = D_{31} = E\nu / (1 + \nu)(1 - 2\nu) \end{aligned} \right\} \rightarrow D \text{ is material stiffness}$$

$$\varepsilon_{th} = \alpha(T - T_{ref}) \rightarrow \text{Thermal induced strain}$$

where,  $E$  is Young's modulus of a material and  $\nu$  is the Poisson's ratio. For point load and distributed load, the equation above is implemented under Global equations to calculate the stress generalized by the strain.

When stress variations and index changes (*Equation 3.3* and *Equation 3.4*) are known within the fibre cross section, wavelength changes can be calculated along the  $x$  and  $y$  direction using the following equations.

$$\left. \begin{aligned} (\Delta\lambda_B)_x &= -\frac{(n_{eff})^3}{E} \times \{(p_{11} - 2\nu p_{12})\sigma_x + [(1 - \nu)p_{12} - \\ &\quad \nu p_{11}](\sigma_y + \sigma_z)\} + \frac{2n_{eff}A}{E} \times \{\sigma_z - \nu(\sigma_y + \sigma_x)\} \end{aligned} \right\} \quad \text{Equation 5.6}$$

$$(\Delta\lambda_B)_y = -\frac{(n_{eff})^3 A}{E} \times \{(p_{11} - 2vp_{12})\sigma_y + [(1-v)p_{12} - vp_{11}](\sigma_x + \sigma_z)\} + \frac{2n_{eff}A}{E} \times \{\sigma_z - v(\sigma_y + \sigma_x)\} \quad \text{Equation 5.7}$$

where  $n_{eff}$  is the effective index of refraction of stress free material,  $E$  is the Young's modulus of the fibre,  $v$  is the Poisson's ratio,  $p_{11}$  and  $p_{12}$  are the photoelastic constants and  $\sigma_{x,y,z}$  are normal stress.

The results of wavelength changes in the  $x$  and  $y$  directions can be used to predict the broadening of spectra or the possibility of a birefringent effect. The resultant wavelength change produced by the simulation will be discussed in Section 5.4. To implement these equations and solve them it is necessary to introduce proper boundary conditions for point load and distributed load models.

When a material is subjected to a uniform pressure, it tends to deform in every direction. The strain induced refractive index change is due to the photo-elastic effect and it is given by

$$\Delta \left( \frac{1}{n_{ij}^2} \right) = p_{ijkl} \varepsilon_{kl} \quad \text{Equation 5.8}$$

where  $p_{ijkl}$  are components of the photo-elastic tensor and  $i, j, k$  and  $l$  are integers.

When a FBG is subjected to uniform pressure, wavelength changes can be calculated manually by *Equation 3.11*. To analyse the wavelength changes due to uniform pressure, the following conditions were introduced to the FEA model to complete the mathematical model.

For computational modelling of uniform pressure sensing, cylindrical coordinates were chosen. For an optical fibre, when a strain is isotropic in the cross section, the effective index changes are given as follows (*Equation 5.9*):

$$\frac{\Delta n_{eff}}{n_{eff}} = -\frac{n_{eff}^2}{2} [(p_{11} + p_{12})\varepsilon_r + p_{12}\varepsilon_z] \quad \text{Equation 5.9}$$

The radial strain is  $\varepsilon_r$  ( $= \varepsilon_{11} = \varepsilon_{22}$ ) and axial strain is  $\varepsilon_z$  ( $= \varepsilon_{33}$ ) due to the symmetry of the structure. Hence, the Bragg wave length change due to strain and effective mode index change is given by *Equation 5.10*:

$$\frac{\Delta\lambda_B}{\lambda_B} = -\frac{n_{eff}^2}{2}(p_{11} + p_{12})\varepsilon_r + \left(1 - \frac{n_{eff}^2}{2}p_{12}\right)\varepsilon_z \quad \text{Equation 5.10}$$

This equation will be used to calculate the wavelength change due to uniform pressure on the FBG structure. The fibre material is less sensitive to the pressure due to the high Young's modulus and Poisson's ratio. To enhance the pressure sensitivity, it could be coated with a polymer material to improve the material properties as discussed earlier for plain fibres (Section 3.4). To implement these mathematical steps, it is necessary to introduce proper boundary conditions to complete the mathematical model.

#### 5.3.4 BOUNDARY CONDITIONS

There are different boundary conditions involved in each case, due to significant differences in the pressure fields. These conditions will be discussed separately as follows.

- I. First, the point load case is considered. The following Figure 5.4 shows the computational domain of the end face fibre.

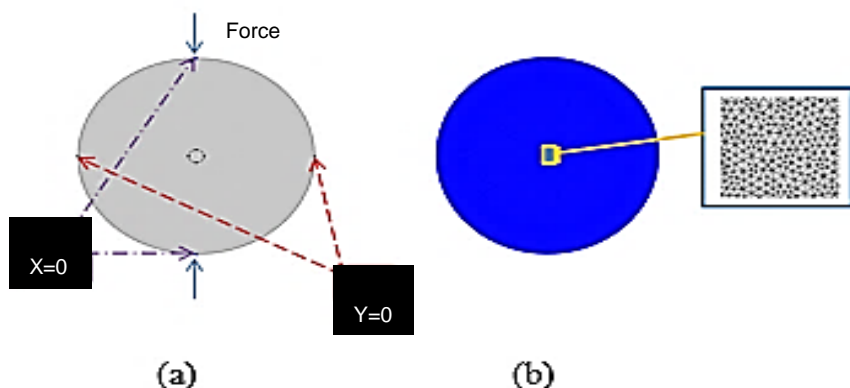


*Figure 5.4: Schematic diagram of computational domain for point load (a) and mesh diagram (b)*

- II. The next step is to consider distributed loading on the fibre. To apply load evenly on the fibre, two glass plates are placed on the top and the bottom of the fibre as shown in Figure 5.5.

III. For uniform pressure sensing (see Figure 5.6), firstly a bare fibre is considered and secondly the fibre is uniformly coated with a polymer.

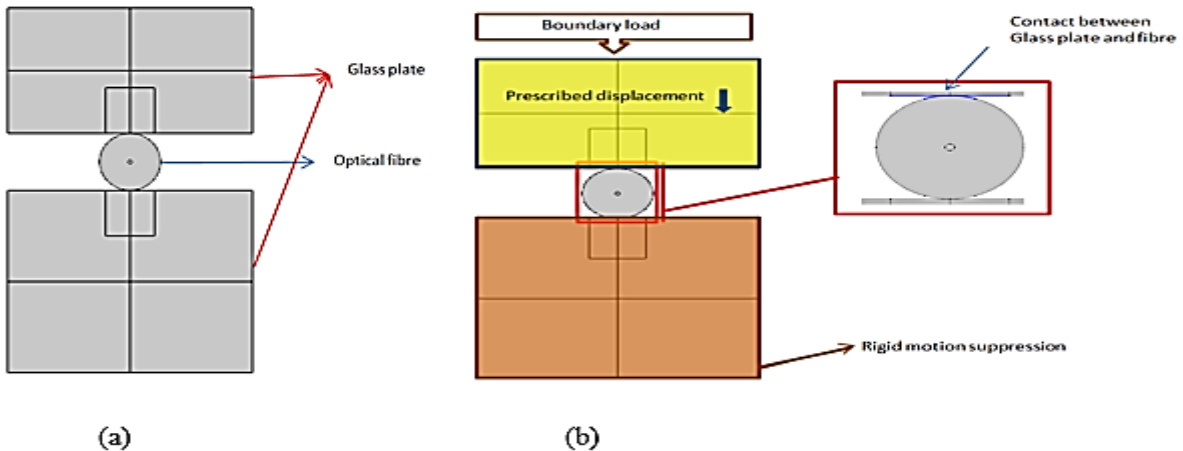


*Figure 5.5: Schematic diagram of computational domain for distributed load on an optical fibre (a) and boundary conditions (b)*

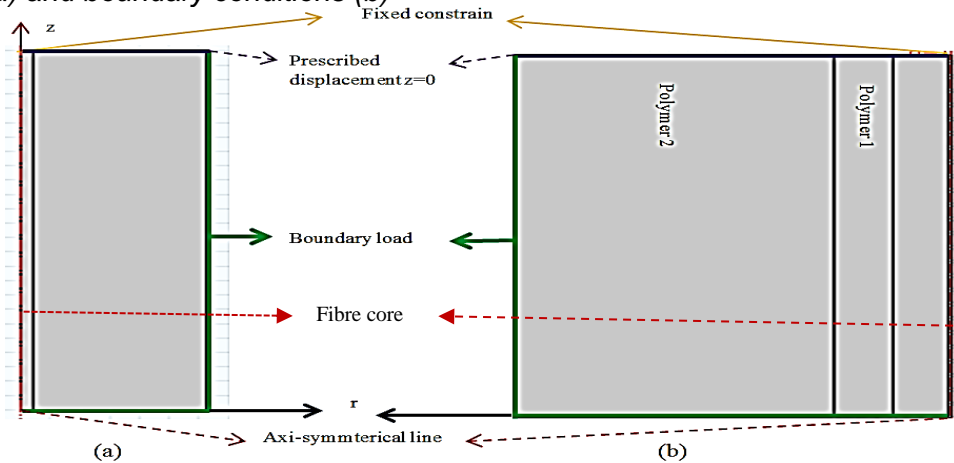


*Figure 5.6: Schematic diagrams of bare fibre (a) and polymer coated fibre (b) experiencing uniform pressure in cylindrical coordinates*

Once the computational domain is defined, the introduction of boundary conditions is required. These boundaries should consider transferring the applied load into the fibre and avoid unnecessary twisting or rotating of the fibre. This can be done by the Solid Mechanics interface under physics in COMSOL modules. For analysis, different mathematical conditions, parameters and boundaries were considered.

For each case, plain strain is selected assuming deformation of the structure is negligible. A linear elastic material was selected, and the temperature was set to 20 °C. For point load, as shown in Figure 5.4 (a), equal force was applied on opposite directions. To avoid unnecessary movement in the x and y direction, a

point prescribed displacement was introduced on 4 main points on the fibre. For this study, a 1 mm length of fibre was selected for the simulation.

For a distributed load on a fibre, the load was applied on the glass plate and the pressure transferred on a 1 mm long fibre, although it is not shown in the schematic diagram. To apply the load ( $L$ ) on the top of the glass plate, a boundary load was added. The boundary load is allowed to define the direction and the total force on the glass plate. These loads should not disassemble the whole structure. Therefore, contact boundaries were introduced in between the top and bottom plates to act as one piece of structure, as shown in Figure 5.5 (b). To avoid rotation and twisting of the structure, rigid motion suppression was selected for the bottom of the structure. To avoid unnecessary computational time and structure movements, domain prescribed displacements were introduced to the top of the plate considering moving vertically down only. Point prescribed displacements were also introduced to implement fibre movement while applying load.

The boundary conditions mentioned above will provide exact formulations of equations and correct solution to the chosen computational methods in solid mechanics. The solution of the Solid Mechanics interface should transfer into the Electromagnetic wave, frequency domain interface and solve them using proper equation by introducing appropriate boundary conditions in selected domains. The mode analysis was performed for a fibre end face only. Therefore, it was selected in the domain of the fibre core and cladding only. In the selected domains, electric fields are solved for three vector components vector for the full field. The wave equations are solved by implementing the following parameters and conditions under the wave equation node (see Figure 5.7).

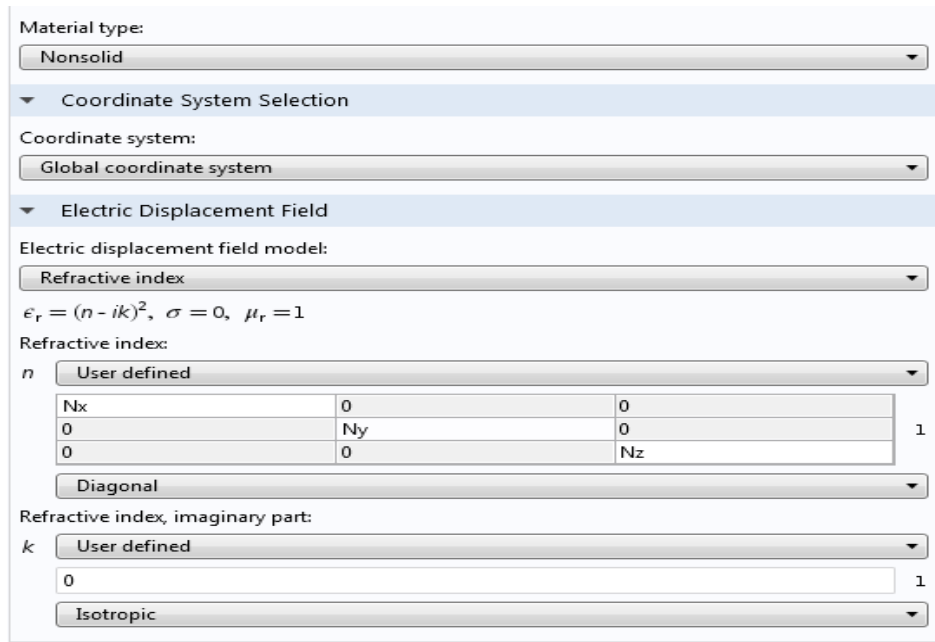


Figure 5.7: Screen shot of wave equation is set under electromagnetic wave, frequency domain in COMSOL

For uniform pressure sensing, computational domains were created for bare fibre and polymer coated fibre with different lengths and thicknesses. To keep the structure from unnecessary movements, a point fixed constraint was introduced under Solid Mechanics, as shown in Figure 5.6. A prescribed boundary constraint was introduced to the top edge of the structures, allowing radial direction movements only. It is assumed that the whole structure is under the uniform pressure, which causes squeezing of the structure. To analyse the pressure sensitivity on the structure with different loads ( $L$ ), a stationary study was performed using a parametric sweep under the study node which allows varying boundary loads.

After the above steps, meshing of the domains was required to visualize the resultant stress field and electric field. This is obtained by defining the mesh through the domain properly.

### 5.3.5 FINITE ELEMENT ANALYSIS

In these models, there are different domains with different physics problems. To solve these problems, it is required to introduce the appropriate mesh to optimise the process. For point loads, previously Figure 5.4 (b) showed the meshing on the fibre. The point load model was solved by applying different loads on a fibre. A suitable calculation of the stress variation on a fibre requires a finer mesh

on the fibre, as a discontinuity of stress pattern would have occurred if an incorrect size and shape of mesh had been selected. By ensuring that the maximum size of the triangular mesh was one-tenth of the wavelength in the medium, the optical wave propagation through the domains was determined to the required level of detail. Figure 5.8 shows the meshing of the entire structure for a distributed load. Accordingly, the top and glass plates have different mesh compared to the end face of the fibre. The load is applied and transferred through the top plate. The bottom plate holds the fibre structure and stops unnecessary rotation. In the end face of the fibre, the refractive index is changed due to stress variation. To view these all scenarios, it was necessary to mesh the end face of the fibre finely and other boundaries accordingly. In the end face, the maximum size of the triangular mesh is defined as one-tenth of the wavelength in the medium in order to resolve the wavelength finely through the domains. Glass plates were meshed using mapped mesh method and considering the condition chosen.

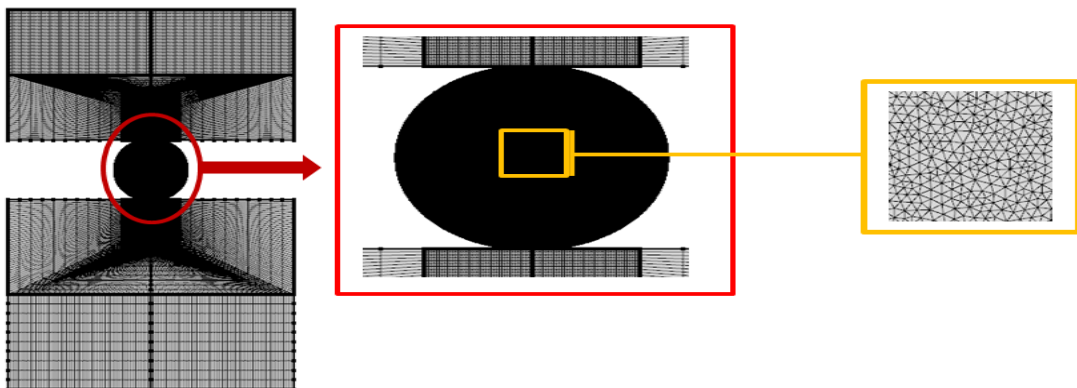


*Figure 5.8: The domains of distributed load with its defining mesh*

The analysis was performed by adding different loads to the glass plate. Therefore, parametric analysis was used to introduce the variation of load from 0 to 75 N. To solve structural mechanics and optics problems, stationary and mode analysis were chosen under study node. For point load, an extra parametric solver was introduced to analyse the stress coupling effect and vice versa. For distributed loads, another parametric sweep was added to calculate the strain generalized effect compared to the plain strain effect. To solve a simulation more time and memory efficiently, PARDISO solver was selected. It helps to speed up the simulation by reducing the solution time.

Triangular mesh was introduced to analyse the uniform pressure on bare and polymer coated fibre, as shown in Figure 5.9. The number of meshes were dependent upon the material types and the pressure experienced. Pressure has been created varying from zero to 70 MPa on bare fibre and up to 10 MPa in polymer coated fibre to compare with the literature. To analyse (gauge) pressure sensitivity up to 50 kPa, the geometrical structure has been changed. Stationary solver was used under parametric sweep and PARDISO solver was chosen under direct solver.

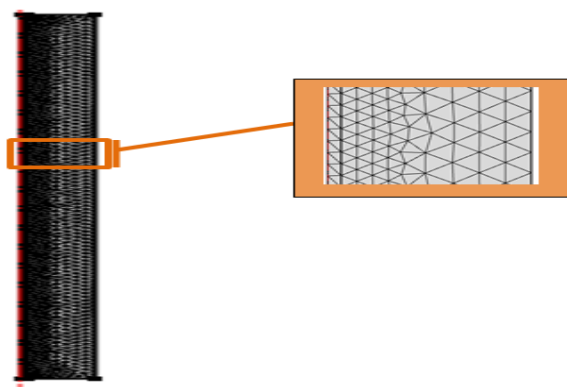


*Figure 5.9: Mesh diagram on the uniform pressure sensing on bare fibre*

### 5.3.6 ANALYSIS (POST PROCESSING)

The main purpose of this point load and distributed load simulations is to observe the birefringent effect due to an external load. To observe the birefringence, it is necessary to solve the effective mode indices. This was achieved by adding Global evaluation under derived values in the result section (computational simulation). To plot the wavelength changes due to an added load, point evaluation was added to the same section. The axis of the core was selected under data set for the point evaluation. In uniform pressure sensing, the pressure sensitivity was analysed with the aid of equations and simulation results.

## 5.4 RESULT FOR POINT LOAD AND DISTRIBUTED LOAD SIMULATION

The main aims of this section are to understand the behaviour of single mode fibre with applied load, especially the birefringent effect. To observe the birefringence effect with applied load, the computation simulation was conducted with the load ( $L$ ) changing from 0 to 50 N for a point load and up to 70 N for distributed load on simple FBGs.

#### 5.4.1 EFFECTIVE MODE INDICES CHANGE WITH TEMPERATURE AND POINT LOAD

Figure 5.10 shows the load dependency of effective mode indices for two different temperatures. The first graph (a) represents the simulation performed under same temperature, 20 °C. The next graph (b) shows the effective mode variation when the reference temperature is 1000 °C. In both graphs, the effective refractive index (ewfd.neff- $n_{eff}$  in FEA) values were given for without stress-optic relation (no-coupling) and with stress-optic relation (plane strain). In Figure 5.10, ewfd.neff (1) and ewfd.neff (2) refer to the two different effective refractive indices values simulated with and without stress-optic relation.

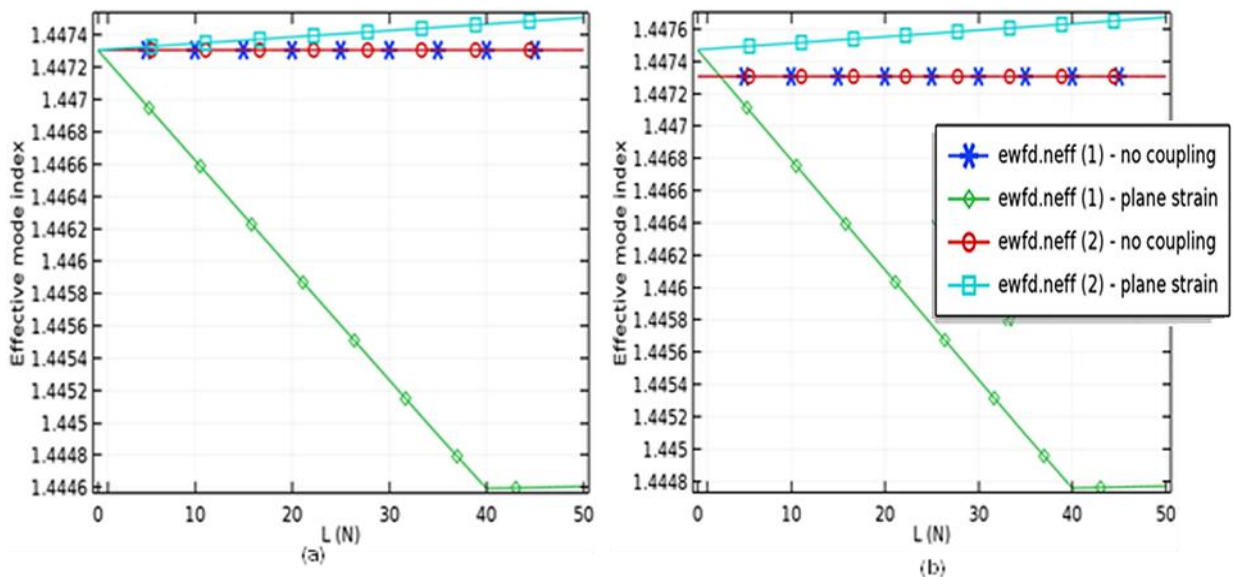


Figure 5.10: Effective mode index variations, with and without stress-optic relations when reference temperature is 20 °C (a) and 1000 °C (b)

According to Figure 5.10 (a) and (b), the effective mode index remains constant (1.4473) without any coupling. However, under plane strain assumptions with zero load, the effective mode index becomes 1.4475 at 1000 °C (Figure 5.10(b)). Further, for the plane strain calculations for both temperatures, both of the effective mode indices change with increasing load. The ewfd.neff (1) index decreases with increasing load until it reaches the cladding refractive index value (1.4447 at 20 °C as noted in Section 4.4) at 40 N. It is clear in Figure 5.10 that one effective mode index (ewfd.neff (1)) changes significantly with the load, whilst

other (ewfd.neff (2)) showed minimal change; hence, ewfd.neff (1) is effective for the analysis of a point load.

Depicted in Figure 5.11 is the effective index mode of stress generalized strain (calculated using the proper mathematical equations discussed in Section 5.3.3) for 1000 °C. The index value of 1.4473 at zero load differs slightly from the plane strain mode index. Both show a significant change in the trend after 40 N, with the plane strain being constant and the other showing a reversal of the trend. Therefore, the effective mode index value 1.4473 can be selected as the proper value for the initial mode index for further calculations.

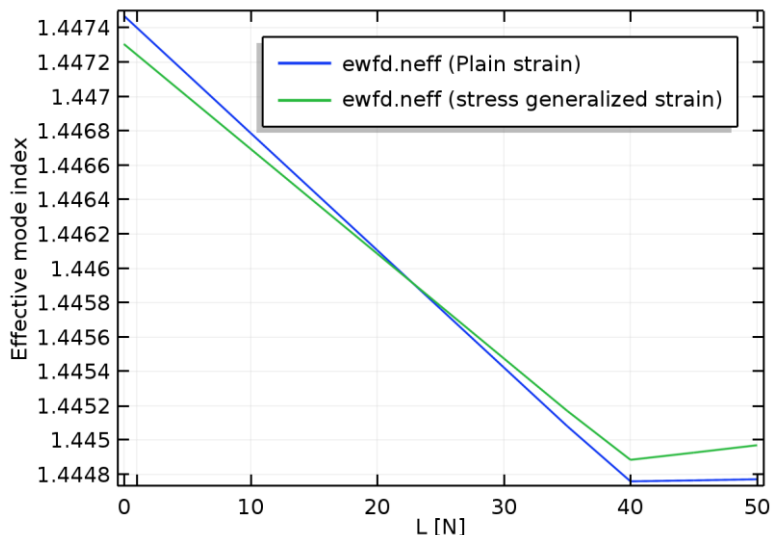
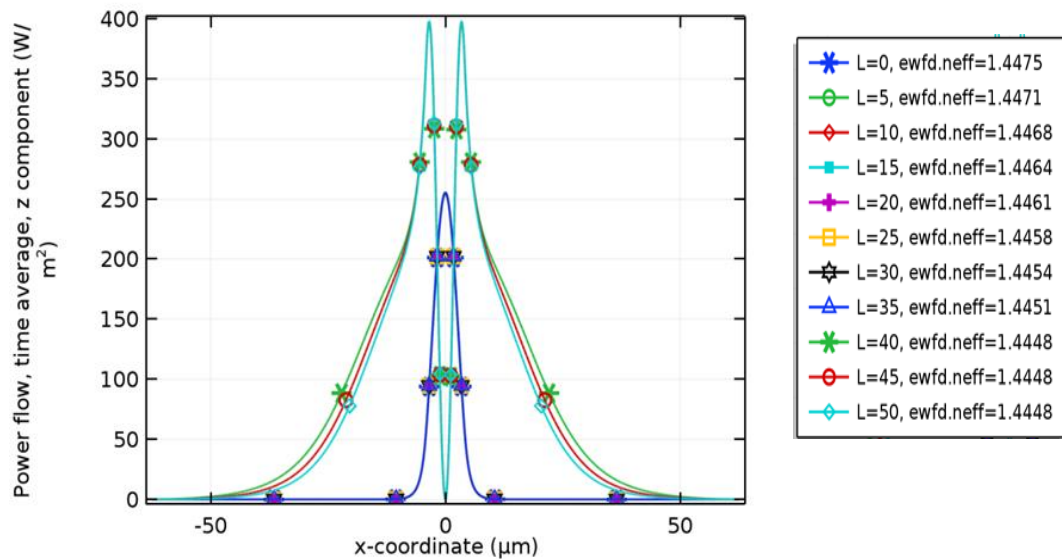


Figure 5.11: Effective mode variation with plain strain and generalized plain strain when reference temperature is 1000 °C

The sudden change in the behaviour of the effective index at 40 N is due to the change from the SMF28 optical fibre no longer supporting a guided mode. Clearly the software (COMSOL) shows great utility, as it is able to track the behaviour of the mode from being guided to unguided. To understand the behaviour of the effective mode index at 40 N compared to other applied loads, the power flow time average (intensity) along the z direction was plotted (see Figure 5.12) at various loads to see the how the optical mode changed from the usual pattern (Figure 4.6).



*Figure 5.12: Power flow across modes across end face of the fibre.*

Figure 5.12 shows that there is a significant change to the intensity distribution across the fibre after 40 N. Before 40 N, most of mode is a single narrow curve, confirming it is confined within the core area of the fibre. Above 40 N, it broadens significantly, and splits into two curves, showing it is no longer propagating as a single mode in the core area of the fibre. It shows increase of intensity variation in the range of 40 to 50 N. The mode variation from zero loads to 50 N can be observed by plotting the mode on the end face of the fibre. The following figure shows the mode fields at 0, 20 and 40 N.

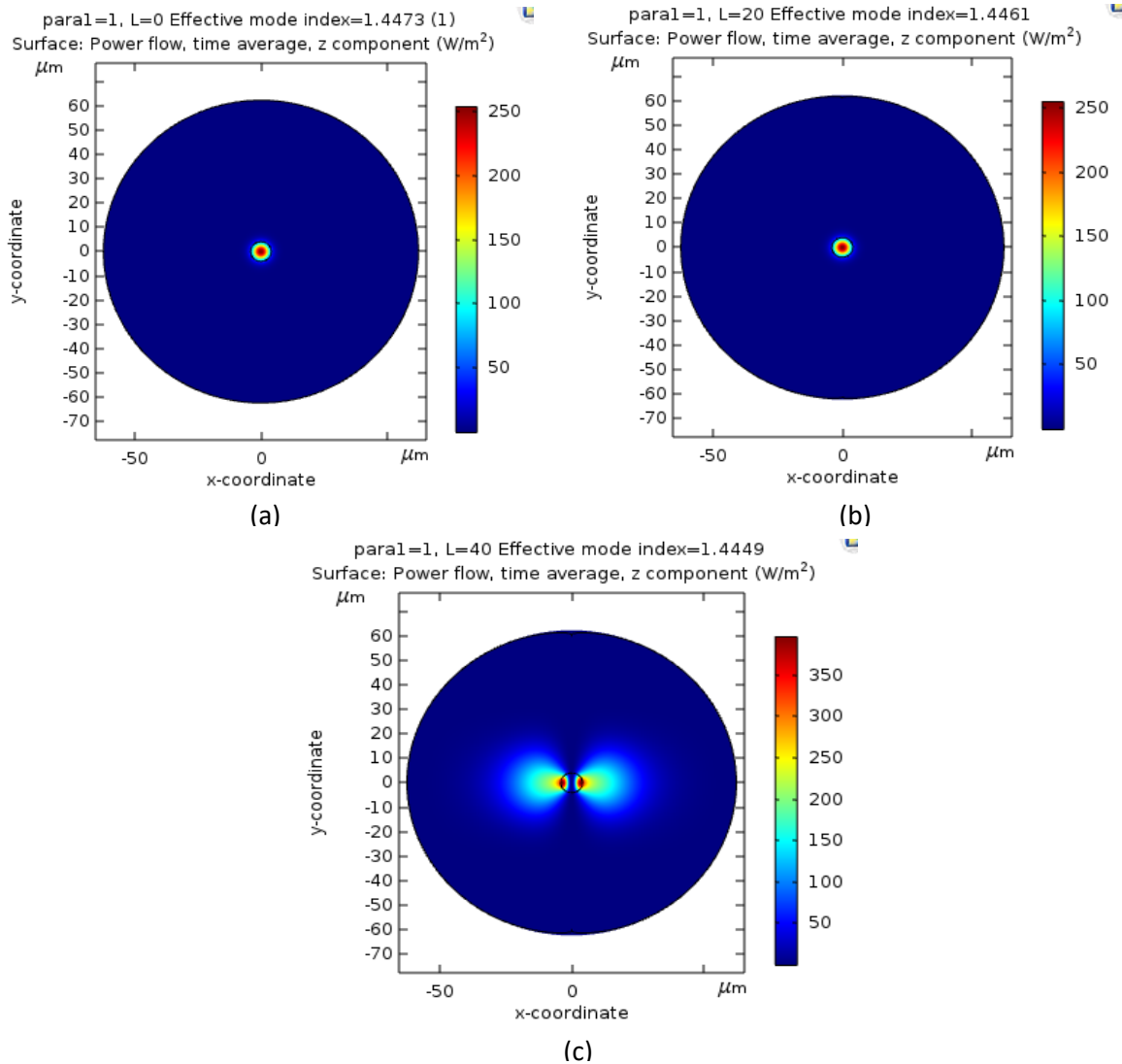


Figure 5.13: Power flow variation on the end face of the fibre due to 0 N (a), 20 N (b) and 40 N (c)

Figure 5.13 clearly shows the birefringence effect at 40 N. At smaller loads, it is visible that the mode shapes are not changing; however, after 40 N it starts to change in the  $x$  and  $y$  directions with the effect of refractive indices change. This phenomenon has led to birefringence. This has also been indicated in Figure 5.12 with intensity variation formed after 40 N. After 40 N, the resultant effective refractive index value and cladding refractive index values are similar. Therefore, above a 40 N load, the SMF28 fibre is no longer behaving as a single mode fibre, and so the optical field changes significantly, as clear in Figure 5.12.

Figure 5.14 shows the stress variation in each direction due to applied point load whereas Figure 5.15 shows the stress variation in the middle of the fibre along the  $y$ -direction.

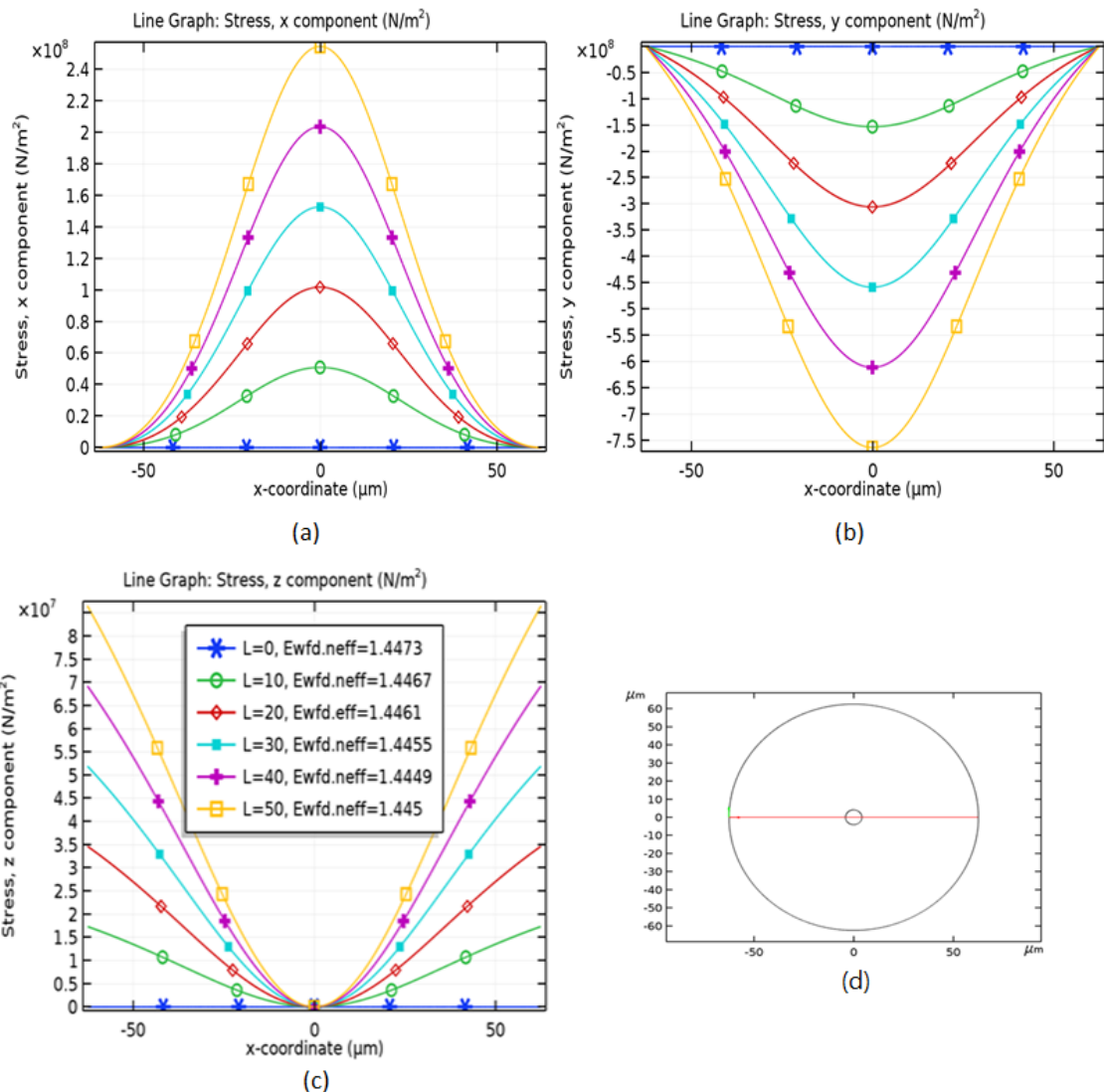


Figure 5.14: Stress variations along x (a), y (b) and z direction (c) and along the middle of the fibre as shown in red line (d)

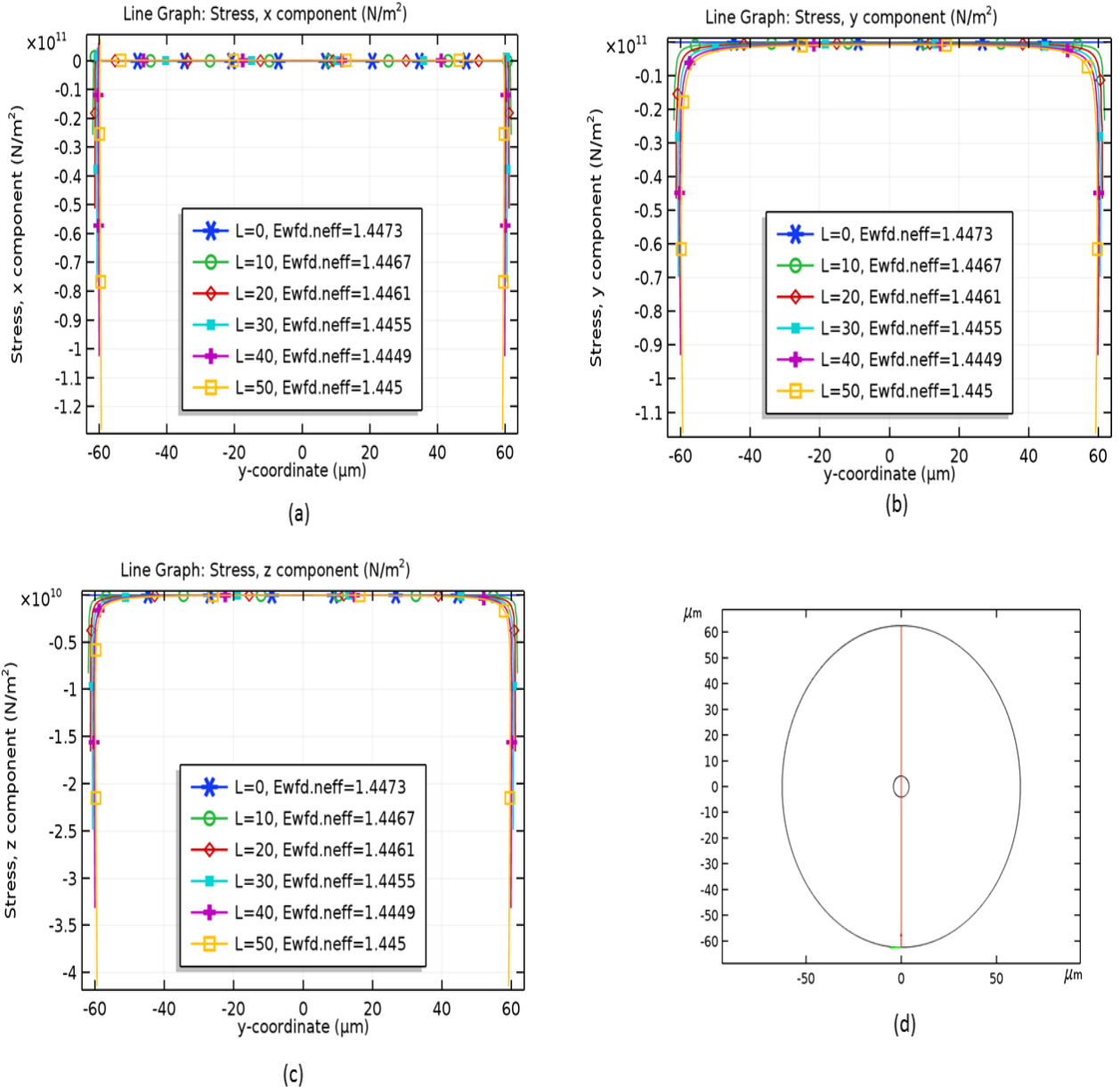


Figure 5.15: Stress variations in the x (a), y (b) and z direction (c) and in the middle of the fibre line as shown in (d)

Figure 5.14 and Figure 5.15 show the symmetrical stress variation on horizontal and vertical directions on the fibre cross section. Therefore, birefringence on a point load fibre shows the symmetrical behaviour as shown in Figure 5.12 and Figure 5.13 (c). Although this shows symmetrical behaviour, some experimental results showed a non-symmetric spectrum peak due to the birefringence effect as noted in Section 3.2.2. These non-symmetrical shapes were observed in distributed load fibres. In the next section the distributed load will be considered more realistically in application practically compared with point loads. It will further investigate the reasons behind these non-symmetrical shapes.

#### 5.4.2 BEHAVIOUR UNDER A DISTRIBUTED LOAD

To understand the behaviour of distributed load on fibres, the computation domain was created, as shown in Figure 5.5. The load was applied on the top glass plate and varied from 0 N to 75 N. Previous simulations for point load were considered up to 50 N; however, this has been extended up to 75 N to provide more information. Similar to previous simulations, stress generalized strain was considered only to avoid plain strain conditions. Figure 5.16 shows the resultant effective mode index variation due to a distributed load due to generalized plain strain along the z direction.

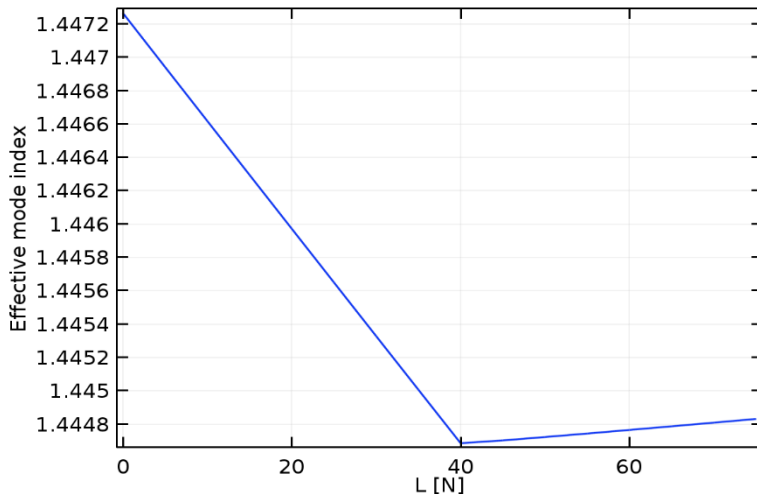


Figure 5.16: Graph of effective mode index variations with applied load for distributed load fibre

According to the above figure, the initial effective mode index without any force is 1.4473 which is similar to the effective mode index given for the point load simulation. Similar to the mode index variation due to a point load, the effective mode index decreases steadily with applied load until 40 N and then there is a sudden change in trend including a slight increase due to the unguided behaviour of SMF28 fibre after 40 N. The following figures confirm this, showing the power flow (intensity) along the z direction for different loads at the end face of the fibre (Figure 5.17) and their power flow across the centre of the fibre (Figure 5.18).

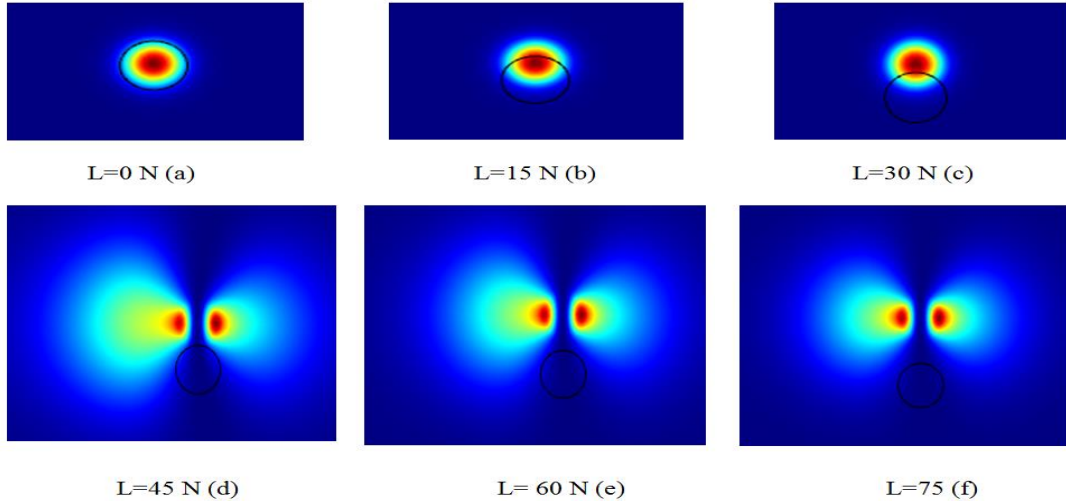


Figure 5.17: Intensity variation on the end face of the fibre with different loads

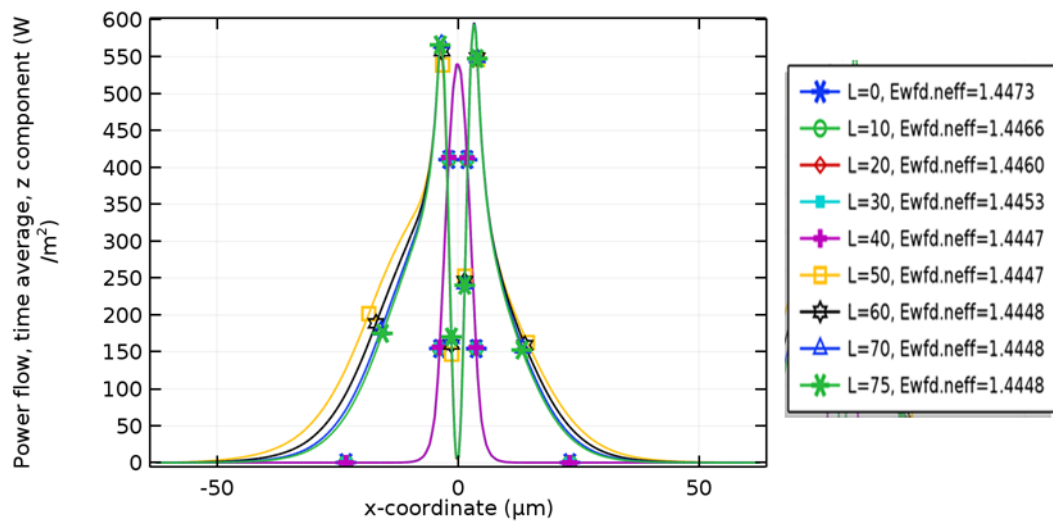


Figure 5.18: Intensity of all effective mode values along z direction

Figure 5.18 shows a circular mode until 40 N and above after 40 N, double shapes appear. These mode shapes are not symmetrical compared to the intensities related to the mode shapes formed by a point load (Figure 5.12). In the same figure (Figure 5.18), at 45 N, the shape of the left side intensity related to the mode shape is broader than the right and the maximum height is lower compared to the right. When the distributed load is increased up to 75 N, it becomes narrow and the intensity related to the mode shape height increases. This is evidenced by many experiments conducted to understand the birefringence effect with the distributed load. The spectrum produced by loaded fibre has shown the change wave spectra from linear to curve, broadening or splitting in various studies (Bal, 2010; Wagreich, 1996), which can be explained due to the birefringence effect.

To understand this behaviour, the stress profile in each direction is discussed below (in conjunction with Figure 5.19 and Figure 5.20).

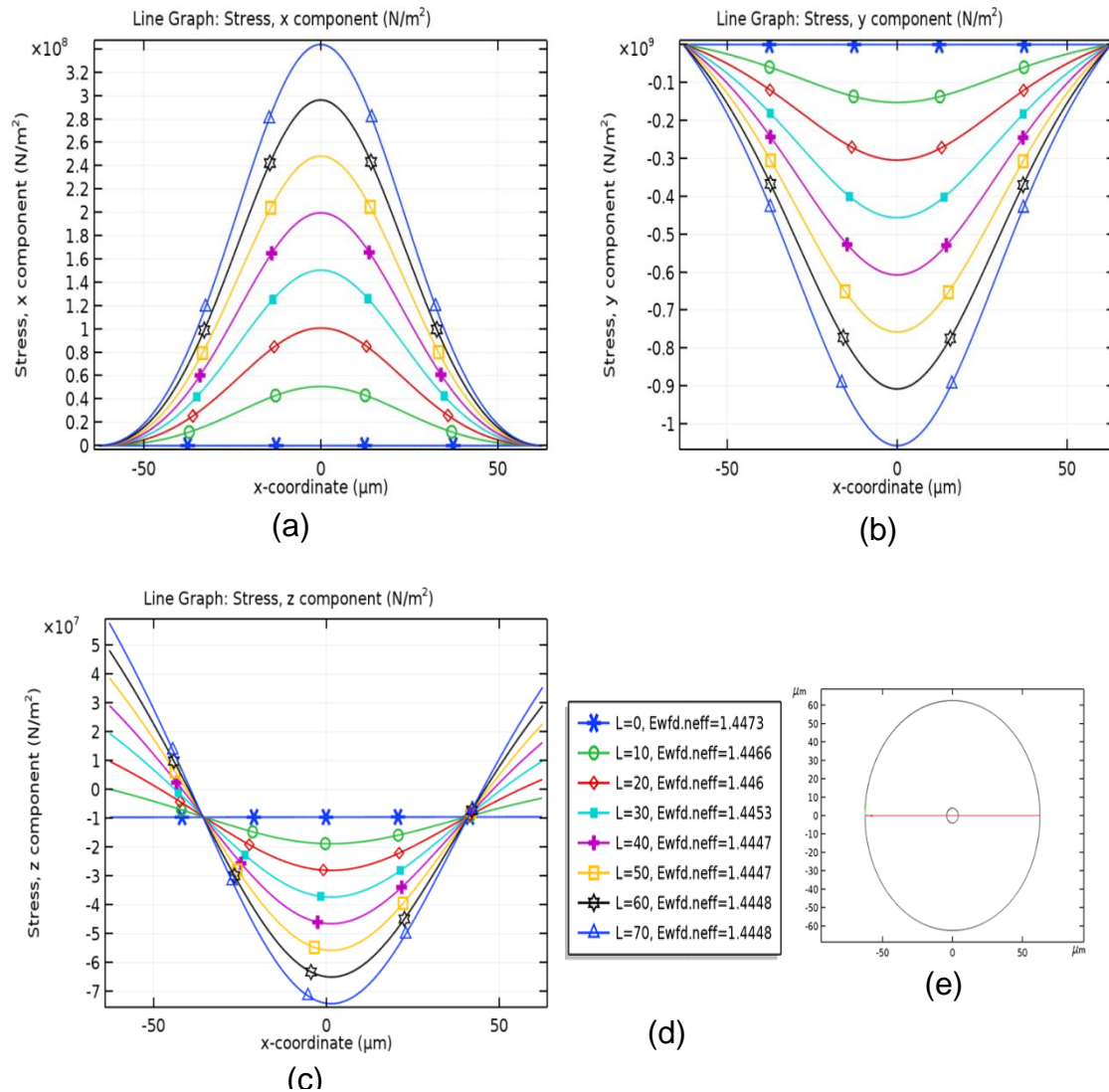
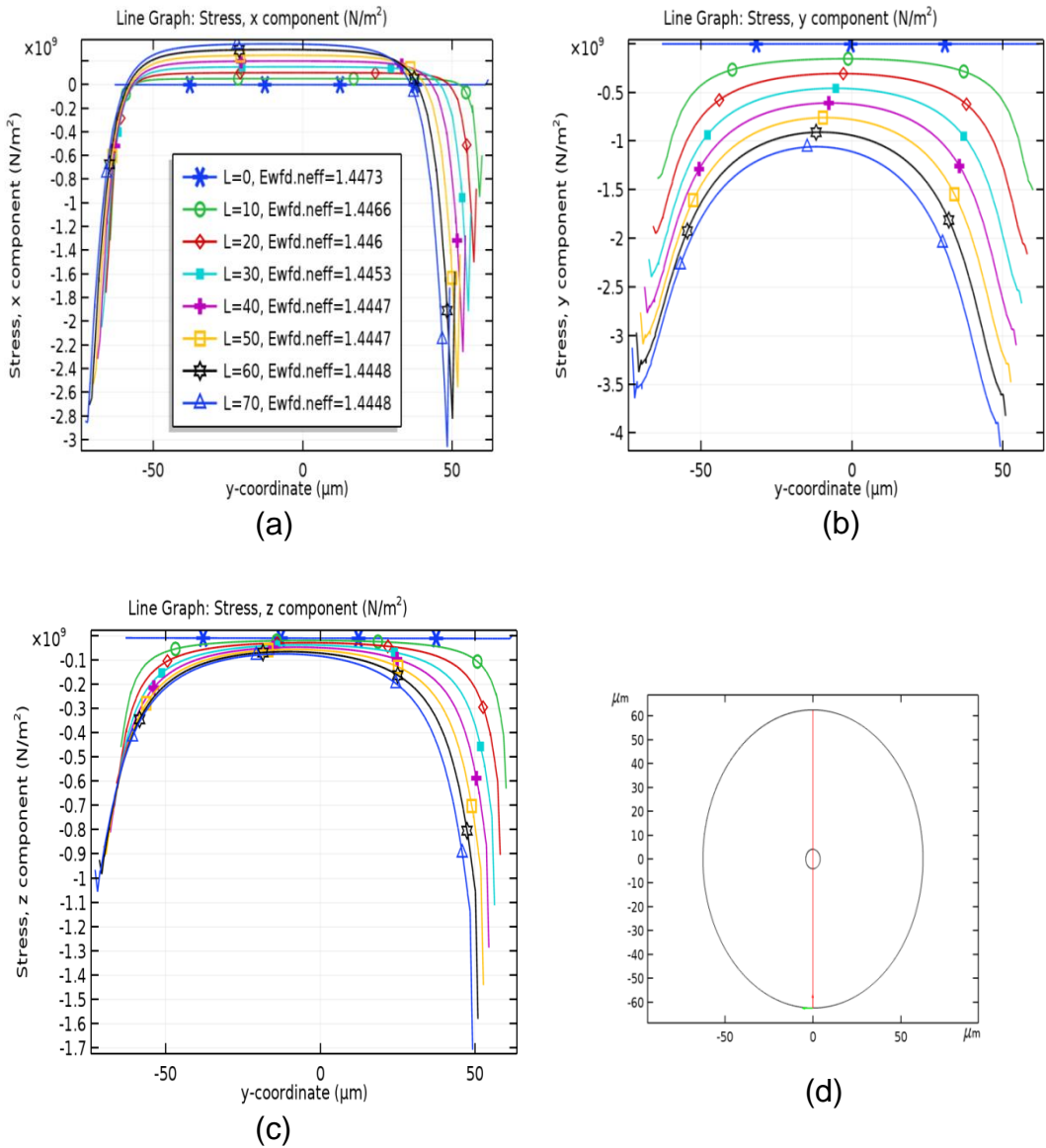


Figure 5.19: Stress variations along x (a), y (b), z direction (c) along middle of the fibre as shown in red line (e) and relevant effective mode index for different loads (d)



*Figure 5.20: Stress variations along x (a), y (b), z direction (c), along middle of the fibre as shown in red line (d) and, relevant effective mode index for different loads*

These figures show the stress variation in the vertical and horizontal directions in the fibre. In Figure 5.19, the stress variation along x and y direction is symmetrical similar to the point load graph in Figure 5.14. But, the stress variation along the z direction is non-symmetrical in Figure 5.20 (c) compared to point load graphs in Figure 5.14. In point load graphs, the initial stress variation along the z direction is zero whereas for the distributed load, none of them are zero at the centre of the fibre. The stress variation in the vertical direction shows a non-symmetrical graph for the distributed load the while the point load shows vice versa. It can be assumed to be due to the result of contact surfaces. When comparing the stress graph with distributed load graph it is clear that the stress variations are different

to one another which has led to non-symmetrical mode shape in the distributed load fibre.

Birefringence is a result of non-uniform induced refractive index change due to stress change. The index of refraction change due to stress effect can be calculated using *Equation 3.3* and *Equation 3.4* with the help of simulation results. Birefringence in the centre of the fibre was calculated using refractive index change in the  $x$  and  $y$  directions using simulation results. The refractive index changes and birefringence in the centre of the fibre due to distributed load are shown in Figure 5.21.

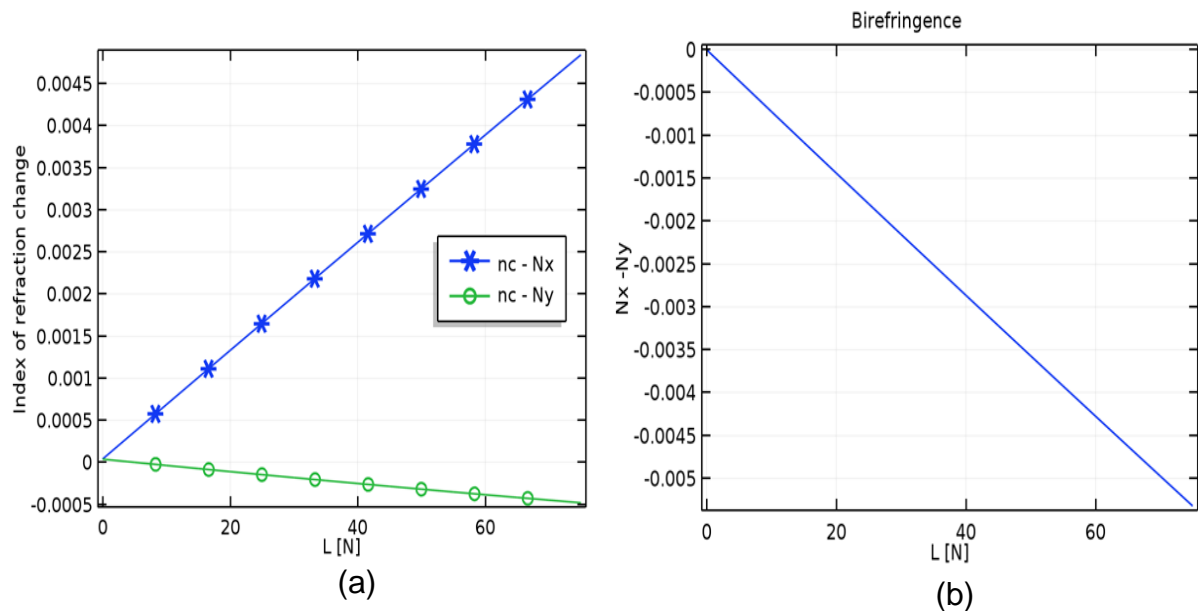


Figure 5.21: Index of refraction changes in (a)  $x$  and  $y$  directions are calculated using equations and simulation results (b) birefringence, in the centre of the fibre

The simulation results were also used to calculate wavelength changes and resultant wavelength in each direction for an FBG. These results are shown in Figure 5.22 where Figure 5.22(a) shows the wavelength change due to the stress effect and Figure 5.22(b) the resultant wavelength. The wavelength difference at 40 N is nearly 3 nm and 5.5 nm at 75 N. All these results are simulated assuming the thickness of the glass plate was 1 mm.

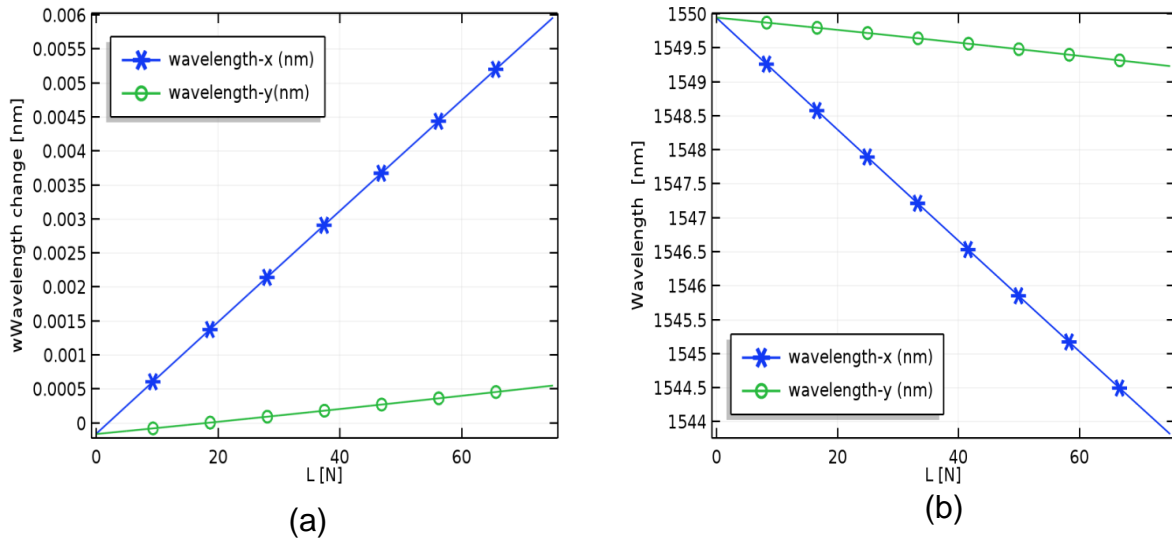


Figure 5.22: (a) Bragg wavelength change in x and y directions and (b) Bragg wavelength in x and y directions for a distributed load

## 5.5 RESULTS OF UNIFORM PRESSURE SENSING

The analysis is based on the computation domain given in **Figure 5.6** (a) and the simulation is performed for simple grating assuming the structure deforms uniformly in both radial and axial directions.

### 5.5.1 BARE FIBRE

The following graphs (Figure 5.23) show the stress variation and strain variation in the centre of the core.

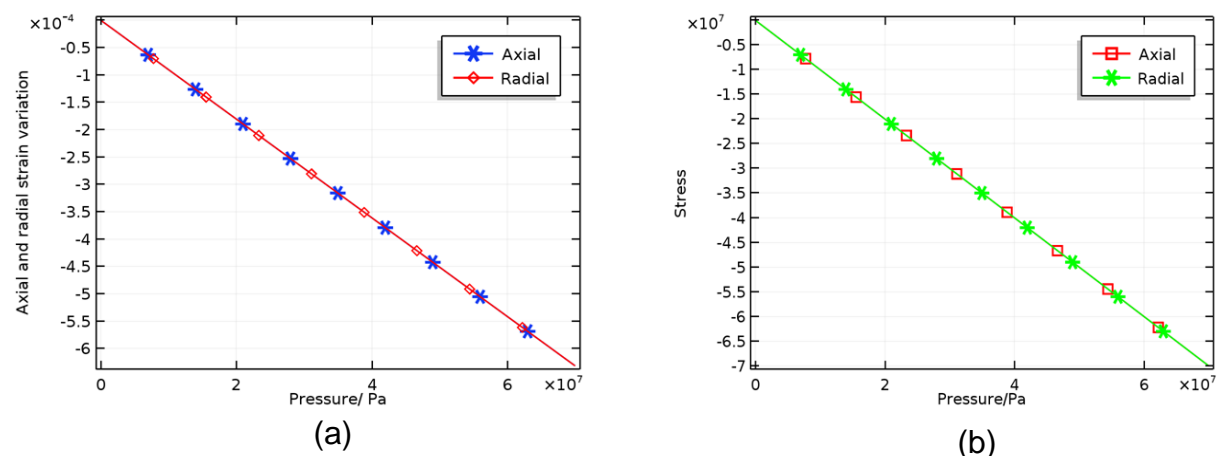


Figure 5.23: Graph of radial axial and radial strain (a) and stress (b) vs pressure  
The strain graph (Figure 5.23 (a)) shows a similar variation for axial and radial directions while the stress graph (Figure 5.23 (b)) shows the same pressure exertion on the core and cladding of the structure. The resultant wavelength shift is plotted using Equation 5.10.

Figure 5.24 is given to show the wavelength shift over the range of 70 MPa gauge pressure.

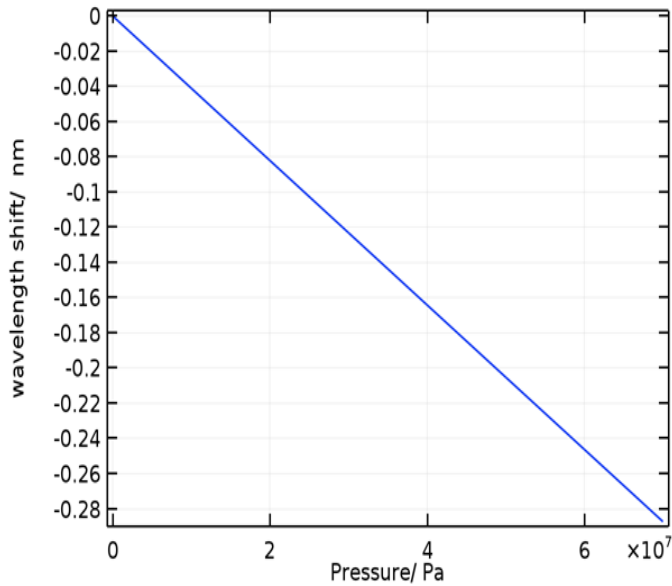


Figure 5.24: Pressure vs wavelength shift

When the Bragg wavelength is 1550 nm, the above graph shows -0.285 nm wavelength shift at 70 MPa. It is assumed that there is no thermal effect for the experiment. To compare the results with the literature, first and second strain-optic coefficient are considered as 0.121 and 0.270. The effective mode index becomes 1.4622 and Young's modulus is 73.1 GPa. The calculated pressure sensitivity can be presented by the Equation below:

$$\frac{\Delta\lambda_p}{\lambda_B \Delta P} = -2.64 \times 10^{-6}/MPa \quad \text{Equation 5.11}$$

The above simulation result is close to the result provided by Hocker (Table 3.2), and confirmed the result produced by simulation is accurate. Table 3.2 shows similar result by other researchers but as noted parameter values were chosen differently.

### 5.5.2 POLYMER COATED FIBRE

Next polymer coated fibre was considered, for comparison with the article published by Yunqi et al. (2000). They coated silica fibres in a cube of polycarbonate and was able to produce 30 times higher pressure sensitivity than

that of Xu et al. (1993). The material properties given in Table 5.1 were considered to verify this simulation for the selected polymer (Yunqi et al., 2000). In the simulation it was assumed to be embedded in a polycarbonate cylinder instead of a cube. The simulation was performed assuming there is no thermal effect. Two coating layers were introduced for adding different materials together or discern whether there is any effect due to the thickness of the coating layer.

*Table 5.1: Material properties of selected polymers*

	Silica	Polycarbonate	For each
Young's modulus ( $E$ )	73.1 GPa	3.5 GPa	
Poisson's ratio ( $\nu$ )	0.17	0.35	
Density	2203 kg/m <sup>3</sup>	1190 kg/m <sup>3</sup>	
Coefficient of thermal expansion	$0.55 \times 10^{-6}/K$	$0.55 \times 10^{-6}$	

simulation, the bulk modulus ( $B$ ) and shear modulus have been introduced under material properties, using the following equations:

$$B = \frac{E}{3(1 - 2\nu)} \quad \text{Equation 5.12}$$

$$S = \frac{E}{2(1 + \nu)} \quad \text{Equation 5.13}$$

In polymer coated fibres, pressure is applied up to 10 MPa. The following graph (Figure 5.25) shows the wavelength shift with the relevant pressure until 10 MPa.

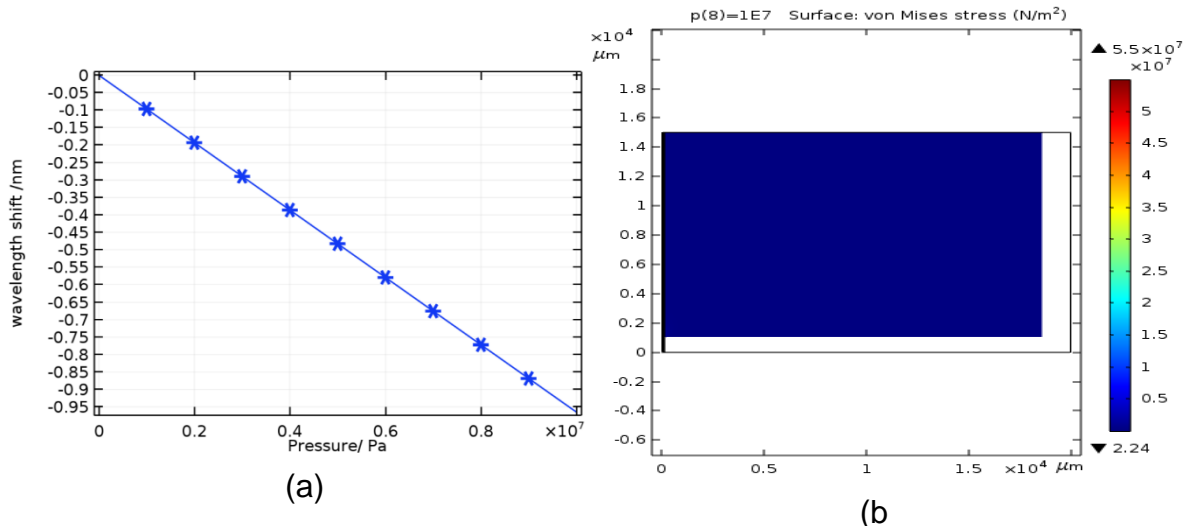


*Figure 5.25: (a) Wavelength shift Vs pressure and (b) 2D cross section view of structure deformation due to pressure experience (b)*

According to Figure 5.25 (a), the calculated Bragg wavelength pressure sensitivity is:

$$\frac{\Delta\lambda_p}{\lambda_B \Delta P} = -6.19 \times 10^{-5} / MPa \quad \text{Equation 5.14}$$

The above result is very close to the experiment result ( $-6.25 \times 10^{-5}$ ) produced by Yunqi et al. (2000). The following graphs (Figure 5.26) show the strain and stress variation along the axial and radial directions for the above simulation.

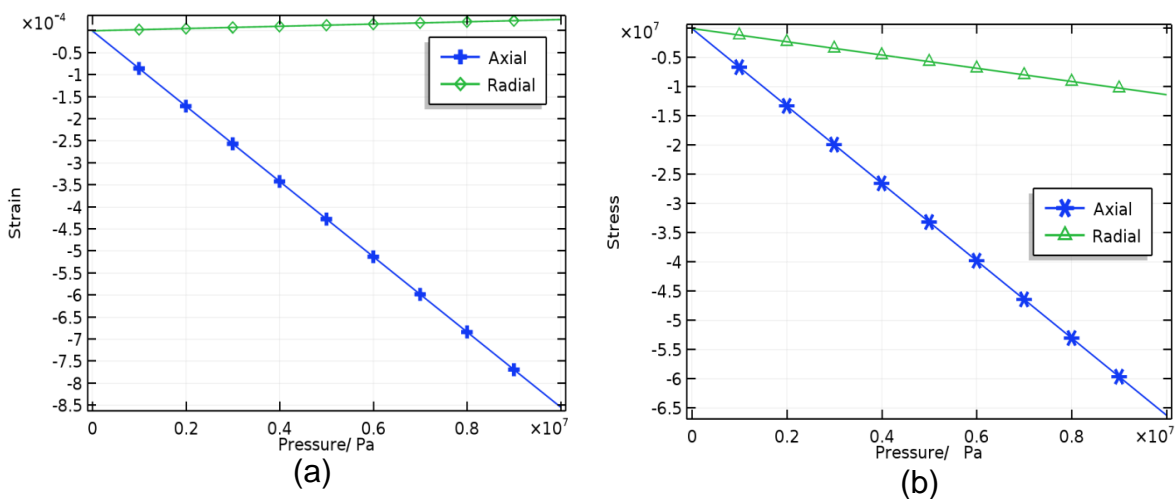


Figure 5.26: Strain (a) and stress (b) variation along axial and radial directions on the centre of the fibre

These graphs show that the strain and stress variation along the axial and radial directions are not equal, in contrast with the bare fibre that showed both variations are equal in the axial and radial directions in Figure 5.23. In polymer coated fibre, the strain and stress variation in the axial directions are higher than in the radial direction.

As the above simulation showed good agreement with previous work with 30 times more sensitivity than bare fibre, further simulations were undertaken using different polymers as coating materials to determine the pressure sensitivity under 0.1 MPa. Therefore, the following materials (Table 5.2) have been considered for the coated material to apply for similar simulations.

Table 5.2: Material properties of PTEF and PDMS

	PTEF (polytetrafluoroethylene)	PDMS (polydimethylsiloxane)
Young's modulus ( $E$ )	0.4 GPa	750 kPa
Poisson's ratio ( $\nu$ )	0.46	0.49
Density	2200 kg/m <sup>3</sup>	970 kg/m <sup>3</sup>
Coefficient of thermal expansion	$100 \times 10^{-6}/K$	$9 \times 10^{-4}/K$

The first material shows a high Young's modulus and high Poisson's ratio while the second shows low Young's modulus and high Poisson's ratio. Figure 5.27 shows a linear pressure variation of the Bragg wavelength up to 100 kPa (~ 1 atm) for both materials. Among them PDMS shows more sensitivity than PTFE. Among the two graphs, the first graph shows a linear relationship for PTFE while the second graph shows non-linear relations for PDMS. The behaviour of PDMS on second graph has been verified by Cooksey & Ahmed (2016).

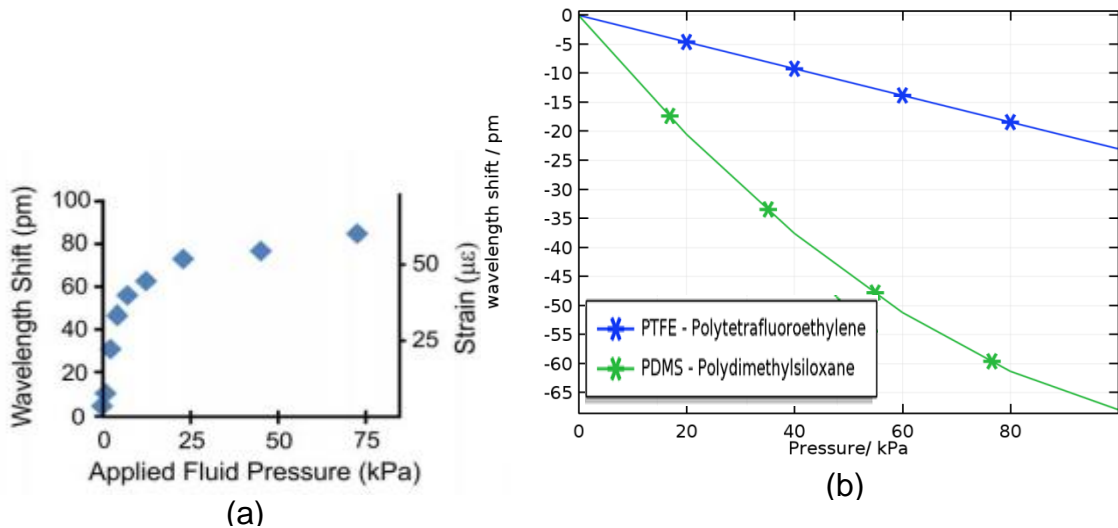


Figure 5.27: Experiment results of (a) wavelength shift vs pressure graph for PDMS (Cooksey & Ahmed, 2016), (b) simulation results for wavelength shift vs pressure for PDMS and PTFE

PDMS shows similar behaviour under pressure in Figure 5.27 (a) and (b). To calculate and compare the pressure sensitivity of selected polymers, second graph (Figure 5.27 (b)) has been chosen. The following table shows the pressure sensitivity of each material considered. It is assumed that the PDMS behaves linear under pressure up to 100 kPa.

Table 5.3: Pressure sensitivity of selected materials

	Silica (Bare)	Polycarbonate	PTFE	PDMS
$\frac{\Delta\lambda_p}{\lambda_B \Delta P}$ (/MPa)	$-2.64 \times 10^{-6}$	$-61.9 \times 10^{-6}$	$-148.4 \times 10^{-6}$	$-451.6 \times 10^{-6}$

The last two materials in Table 5.3 show 55 times and ~170 times high sensitivity than bare fibres. Those two materials clearly can be used in pressure sensing at less than 100 kPa but non-linear behaviour of PDMS has to be addressed. However, when comparing the thermal coefficient of each material, the thermal expansion coefficient of PDMS is 7 times higher than PTFE. Although these simulations were performed without any thermal effect, PDMS can be recommended mostly for further studies. Density-wise PTFE looks more acceptable although it has less sensitivity compared to PDMS. PDMS and PTFE based sensors have already been reported. Therefore, further investigations were performed by reducing pressure and thickness of the material. As PDMS coatings are commercially available but limited to 100  $\mu\text{m}$ , the thickness of the fibre coating was set to 100  $\mu\text{m}$  for both materials. The maximum pressure is set up to 10 kPa. Figure 5.28 shows the wavelength shift for the set pressure limits.

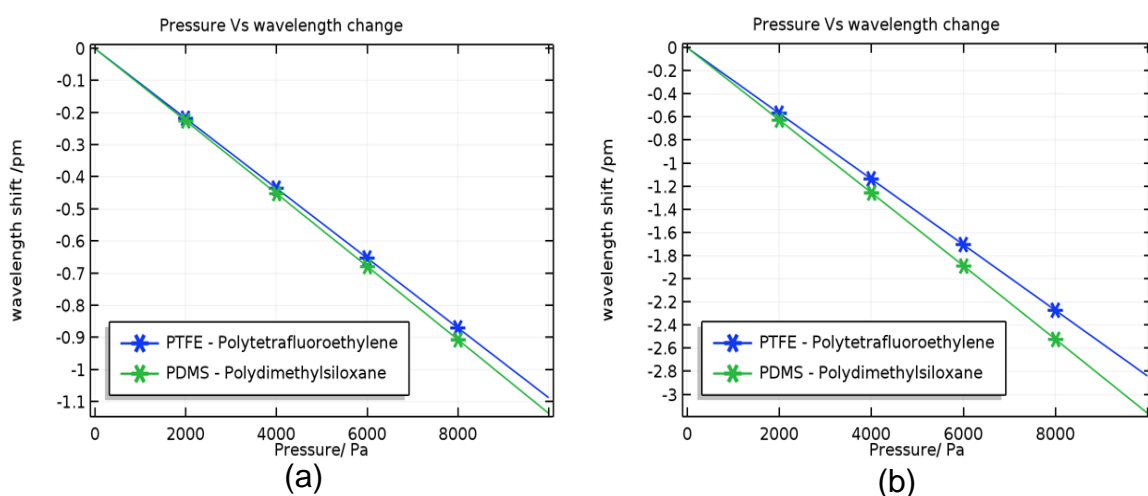
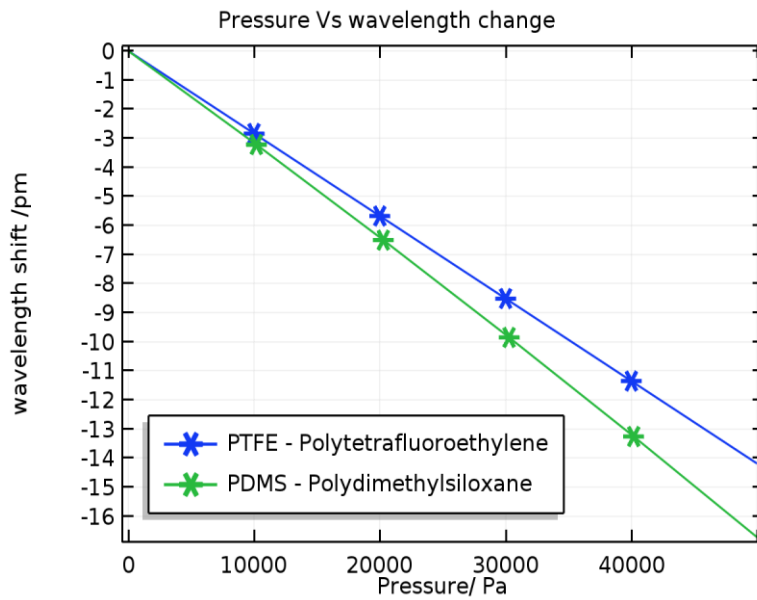


Figure 5.28: Wavelength shift vs pressure, without any diameter deduction of the fibre cladding (a), wavelength shift after 30  $\mu\text{m}$  deduction from the cladding of the fibre

In each case both materials show a linear relationship with the pressure applied. When the fibre diameter decreased it shows 3 times higher sensitivity (Figure 5.28 (b)). Fibre diameter reduction is also practically possible through introducing etching techniques. The pressure sensitivity has been further investigated for

reducing the diameter for both materials. Therefore, the following graph was plotted after setting the pressure up to 50 kPa.



*Figure 5.29: Wavelength shift vs pressure graph for PTFE and PDMS when fibre diameter is 30  $\mu\text{m}$*

Table 5.4 summarises the pressure sensitivity of PTFE and PDMS. Both materials show nearly 35 times (bare fibre) sensitivity without any diameter change at 10 kPa. The same material shows nearly 100 times more pressure sensitivity at 50 kPa compared with the bare fibre at 70 MPa. It shows linear sensitivity under 10 kPa and 50 kPa. Therefore, both materials are viable options for low (gauge) pressure measurement. However, further investigation conducting experiments is required to confirm their commercial use.

*Table 5.4: Pressure sensitivity by different materials under different pressure and changing diameter*

	Cladding diameter of fibre = 30 $\mu\text{m}$		Cladding diameter of fibre = 62.5 $\mu\text{m}$	
	50 kPa		10 kPa	
	PTFE	PDMS	PTFE	PDMS
$\frac{\Delta\lambda_p}{\lambda_B \Delta P}$ (/MPa)	$-183 \times 10^{-6}$	$-216 \times 10^{-6}$ (= -0.34 nm/MPa)	$-70.1 \times 10^{-6}$	$-73.5 \times 10^{-6}$

## 5.6 SUMMARY

This chapter focused on using FEA to understand pressure exerted on optical fibre and proposed new pressure sensors to measure at a low-pressure (gauge) range. Computational models were developed to create a point load and a distributed load on optical fibre considering geometrical deformation under pressure. It included deformation of the structure not only in 2-D coordinates but also 3-D coordinates. This has given a clear picture of the behaviour under transverse compressive load. The results show a birefringent effect with an increase of load confirming the experimentally observed non-linear behaviour. The 2-D model was converted to a 3-D model by adding extra equations to simulate its true behaviour under an applied load. The splitting of the peak produced due to load was in good agreement with the data of the literature available. The analysis was also used to find the magnitude of the wavelength shift in each of the  $x$  and  $y$  directions with the aid of simulation results and mathematical equations.

A possible uniform pressure sensor was modelled considering the literature and further modified for low pressure sensing after confirming the experimental results found in the literature. All the developed models were successfully designed with the aid of mathematical equations.

Those models were used to analyse and determined an enhancement of the pressure sensitivity of FBG based sensors in this chapter. The developed models were in good agreement with the literature provided. Therefore, further analysis was carried out to improve the sensitivity in low (gauge) pressure range by adding polymer coating to change material properties of the cladding and the thickness of the fibre cladding diameter. The sensitivity obtained for the range of 0 - 50 kPa is 100 times sensitivity than the sensitivity reported for bare fibre at 0 - 70 MPa.

According to Table 3.1, the maximum recorded pressure sensitivities at low pressure is 9.08 nm/MPa at range of 0 - 100 kPa for photonic crystal fibres. This study shows the pressure sensitivity of polymer coated fibre using PDMS and PTEF is nearly 0.34 nm/MPa at range of 0 - 50 kPa. Therefore, the proposed pressure sensors at a range of 0 - 50 kPa is a good candidate as a low pressure

sensor when considering the shape of the fibre and medium of the surroundings. Reviewing the predicted sensitivity of the sensor proposed in this chapter is in comparison to the application in the biomedical field as obtained in Table 1.1 and Table 1.2. It is evident that advantages of further investigation are towards biomedical applications.

## CHAPTER 6: Conclusion and future works

### 6.1 KEY OUTCOMES

This work considered a low (gauge) pressure sensor using a FBG for use in the field of biomedicine, sport... etc. To achieve this goal, this study used FEA methods to model FBGs structures and their spectra to analyse and to understand how their behaviour depends on the fabrication process. Then FBGs were modelled with different coatings using FEA to identify the suitable materials to enhance the pressure sensitivity in the range of 0 – 50 kPa.

To achieve the above targets FEA was carried out step by step. Firstly, optical fibre (SMF-28) characteristics were analysed by FEA. Simulations were performed at different wavelength to analyse the number of modes propagating at each wavelength. It was confirmed the only mode propagates at  $\lambda_B$  and  $2\lambda_B$  is  $HE_{11}$ . However at  $(\frac{2}{3})\lambda_B$  more modes (4 modes) were present, confirming its multimode behaviour due to  $V > 2.405$ . The analysis results are also in good agreement with the literature (Figure 2.3 and Figure 2.4). As expected, effective mode index values were between core and cladding refractive index values at each wavelength.

Next, FEA was used to develop new computational models to create FBG refractive index structures and their spectra. The developed computational model was designed using phase mask manufacturing process as it is the commonly used method. This study considered multiple orders of the phase mask instead of an ideal phase mask, as it provides a complex grating structure which requires more research to understand its behaviour at different wavelengths and its response to various methods of exerting pressure (stress, load... etc). The developed 2-D model was used to analyse the wave spectra and their harmonics. The FEA model was capable of creating various FBG structures by changing characteristics of the phase mask and incident angles such as first order gratings, complex grating and tilted grating as shown in Figure 4.33 (simulated by using COMSOL). FFT analysis was performed for the model FBG structure and it provided the number of harmonics, its grating period and expected efficiencies associated with the FBG pattern. The results produced were in a good agreement

with (Kouskousis et al., 2013) and (Rollinson, 2012). Reflection spectra were observed for the same structure at the wavelength of  $\lambda_B$ ,  $2\lambda_B$  and  $(\frac{2}{3})\lambda_B$ . The results were in good agreement with number of modes observed for single mode fibre by using FEA.

The above method of the FBG produced by using 2-D model of computational design has not been reported previously. This method is unique and able produce first order, complex grating or tilted gratings simply by adjusting its parameters and dimensions of first order or multiple order phase mask. The complex FBG pattern was easily imported into a simulated optical fibre to analyse the spectrum at different wavelength.

The next phase of the study was to develop 2-D models for pressure exerted via point load, distributed load and uniform pressure. In many studies of the literature, point load and distributed load were simulated assuming plane strain of the structure. In this study, it was extended to analyse the strain variation in the z direction using COMSOL software. Therefore, all the effects due to force on the fibre were included in the analysis. Those models were used to understand the birefringence effect on fibres due to an external load. Both models showed SMF28 is no longer behaving as a single mode fibre above 40N. The simulation results showed the splitting of the spectrum due to birefringence effects in both point and distributed load simulations. Compared to point load, the distributed load showed unequal peaks at the beginning of the split. After analysing the results, stress variation of distributed load showed the reasons for those peaks. Therefore, those models showed the advantage of computational modelling in understanding the real situation.

Finally, the uniform pressure sensing of the FBG was modelled using literature data and its computational analysis was then verified with the results found in literature. The results of simulations were in a good agreement with literature findings; hence, the validity of the model was confirmed. It was then applied to test different materials in high pressure and once it produced acceptable wavelength change further studies were carried out by lowering the pressure up to 50 kPa. After testing several polymer materials to enhance the pressure sensitivity, PTFE and PDMS were found to be most viable, hence, they were

recommended for further study. Both materials were positive according to the fact that they are commercially available and have already been used for sensing purpose. Although PDMS did not show a linear response around 100 kPa it showed linear response up to 50 kPa. At 10 kPa, PDMS showed high sensitivity while PTFE showed less. However, at 50 kPa, both showed linear and similar response. In contrast with the material properties PTFE has high Young's modulus and low Poisson's ratio while PDMS has vice-versa. Therefore, all the findings give an indication of the coating process of the material that will be different to each other. The proposed low (gauge) pressure sensors are more suitable for low pressure measurement in the range of 0 – 50 kPa compared to the sensors were listed in Table 3.1. The outcome of these FEA simulations has made significant contribution to knowledge in understanding of characteristic of optical fibre, complex FBG structures and their spectrum, various method of pressure exerted on FBGs and advancement of use in modelling pressure sensors.

In conclusion, key outcomes can be mapped with the initial objectives as we planned in the research as shown by the following table;

*Table 6.1: Mapping key outcomes of the study with the initial objectives*

<b>Key Outcome</b>	<b>Targeted Initial Objectives</b>
<ol style="list-style-type: none"> <li>1. Complex FBG structures were developed using FEA method</li> <li>2. FEA model was developed to obtain spectra patterns</li> <li>3. Analysed results for spectra patterns were in good agreement with theoretical and experimental findings</li> </ol>	Model FBG structures and their spectra using Finite Element Analysis (FEA) methods; Analyse their spectra for better understanding of their relationship with the underlying FBG complex refractive index variation
<ol style="list-style-type: none"> <li>1. FEA model was built to simulate moderate pressure on a polymer coated fibre.</li> <li>2. Different materials were analysed and PDMS determined as the most effective coating material at moderate pressure range</li> <li>3. Analysed results in good agreement with existing literature</li> </ol>	Model FBGs with different polymer coatings using a FEA method to identify suitable materials for enhancing the pressure sensitivity at moderate pressures; Compare the results with existing literature to confirm efficacy of the findings in simulations.

## 6.2 FUTURE WORK

Modelling of internal FBG structure post fabrication using a standard phase mask showed good agreement with theoretical analysis and experimental. Therefore, the developed models can be effectively applied in future work with complex grating. All the simulations were performed for wavelength spectrum which was produced assuming 1.066 mm grating length. The grating length was limited by the size of the RAM (32 GB) available in the computer. Moreover, simulating optical fields requires a higher number of mesh points to ensure accurate results. Hence, the higher the RAM capacity of the computer the greater the number of mesh points which leads to more accurate results. A computational model of the phase mask method includes the angle of incidence of the light. This can be used to model a tilted grating for any angle. However, the developed tilted structure could not be analysed due to the number of mesh requirement in the cladding area which needs to show how the cladding modes propagate. Using high power computers with more RAM, this can be achievable. Therefore, future work can be designed using the same model but with high power computers with adequate RAM to analyse the behaviour of tilted structures. The model was built based on the literature and following the manufacturer's (Ibsen) information of the phase mask structure. UV absorption was not included; this was not possible due to the difficulty of finding an accurate value for UV absorption. Although UV absorption in glass is high, it could be neglected considering the small lengths involved. The approach used is validated, as the results agree with the other models and experiments.

For a point load, distributed load and uniform pressure sensing, analyses were performed assuming the grating structure is similar to first order gratings due to the insufficient computer capacity. Analysis of the pressure sensitivity of complex structure can be deeply investigated along with the developed computational models aided with sufficient computer capacity. A more efficient process to doing this is by combining spectral analysis of complex structure with pressure analysing together. The derived results can be greatly utilised to understand the complex structure and its commercial usage.

Low pressure sensing is greatly challenging due to material properties of optical fibre. In regard to commercializing sensors, simplicity of a sensor is a significant factor for consideration. In this study, PTFE and PDMS have been selected for further studied pressure sensitivity in different pressure ranges. The developed computation model shows promising sensitivity at low pressure range (up to 50 kPa). It is also observed that both PDMS and PTFE have shown similar results at low pressure range; hence, future studies should target more on practical viability of both materials at low pressure range. In this study, simulation was performed only for normal gratings. Hence, future studies can consider the application of similar simulation for complex grating structure in 2-D coordinates in Cartesian coordinates.

## REFERENCES

- Abe, I, Kalinowski, HJ, Nogueira, R, Pinto, JL & Frazao, O, 2003, 'Production and characterisation of Bragg grating written in high-birefringence fibre optics', *IEE Proceedings - Circuits, Devices and Systems*, vol. 150, no. 6, pp. 495-500.
- Ahmad, H, Harun, SW, Chong, WY, Zulkifli, MZ, Thant, MMM, Yusof, Z & Poopalan, P, 2008, 'High-sensitivity pressure sensor using a polymer-embedded FBG', *Microwave and Optical Technology Letters*, vol. 50, no. 1, pp. 60-1.
- Allwood, G, Wild, G, Lubansky, A & Hinckley, S, 2015, 'A highly sensitive fiber Bragg grating diaphragm pressure transducer', *Optical Fiber Technology*, vol. 25, pp. 25-32.
- Annamdas, VGM, 2012, 'Review on developments in fiber optical sensors and applications', *International Journal of Materials Engineering*, vol. 1, no. 1, pp. 1-16.
- Atkins, RM, Lemaire, PJ, Erdogan, T & Mizrahi, V, 1993, 'Mechanisms of enhanced UV photosensitivity via hydrogen loading in germanosilicate glasses', *Electronics Letters*, vol. 29, no. 14, pp. 1234-5.
- Bal, HK, Dragomir, NM, Sidiropoulos, F, Wade, SA, Baxter, GW & Collins, SF, 2011, 'Response of some pi-phase-shifted Bragg gratings to elevated pressure', *Proc. SPIE*, vol. 7753, p.775389.
- Bal, HK, Sidiropoulos, F, Brodzeli, Z, Wade, SA, Baxter, GW & Collins, SF, 2010, 'Fibre Bragg grating transverse strain sensing using reflections at twice the Bragg wavelength', *Measurement Science and Technology*, vol. 21, no. 9, p. 094004.
- Barlow, AJ & Payne, DN, 1983, 'The stress-optic effect in optical fibers', *IEEE Journal of Quantum Electronics*, vol. 19, no. 5, pp. 834-9.
- Bennett, J, El-Sherif, MA & Froggatt, ME, 2001, 'Transverse loading effects on embedded Bragg fiber system', *Proc. SPIE*, vol. 4204, p.11.
- Bertholds, A & Dandliker, R, 1988, 'Determination of the individual strain-optic coefficients in single-mode optical fibers', *Journal of Lightwave Technology*, vol. 6, no. 1, pp. 17-20.
- Bhowmik, K, Peng, G-D, Luo, Y, Ambikairajah, E, Lovric, V, Walsh, WR & Rajan, G, 2015, 'Experimental study and analysis of hydrostatic pressure sensitivity of polymer fibre Bragg gratings', *Journal of Lightwave Technology*, vol. 33, no. 12, pp. 2456-62.
- Bilodeau, F, Johnson, DC, Malo, B, Vineberg, KA, Hill, KO, Morse, TF, Kilian, A & Reinhart, L, 1990, 'Ultraviolet-light photosensitivity in Er<sup>3+</sup>-Ge-doped optical fiber', *Optics Letters*, vol. 15, no. 20, pp. 1138-40.
- Bjerknes, L, Johannessen, K & Guo, X, 1997, 'Measurements of Bragg grating birefringence due to transverse compressive forces', *12th International Conference on Optical Fiber Sensors*, Optical Society of America, OTuC7

- Bock, WJ, 1990, 'High-pressure polarimetric sensor using birefringent optical fibers', *IEEE Transactions On Instrumentation And Measurement*, vol. 39, pp. 233-7.
- Bock, WJ, Chen, J, Mikulic, P & Eftimov, T, 2007, 'A novel fiber-optic tapered long-period grating sensor for pressure monitoring', *IEEE Transactions on Instrumentation and Measurement*, vol. 56, no. 4, pp. 1176-80.
- Brady, GP, Kalli, K, Webb, DJ, Jackson, DA, Reekie, L & Archambault, JL, 1997, 'Simultaneous measurement of strain and temperature using the first and second-order diffraction wavelengths of Bragg gratings', *Optoelectronics, IEE Proceedings -*, vol. 144, no. 3, pp. 156-61.
- Broer, MM, Cone, RL & Simpson, JR, 1991, 'Ultraviolet-induced distributed-feedback gratings in Ce<sup>3+</sup>-doped silica optical fibers', *Optics Letters*, vol. 16, no. 18, pp. 1391-3.
- Buchwald, K, 2007, 'Fused Silica Transmission Gratings- A White Paper', <<https://ibsen.com/wp-content/uploads/White-paper-Fused-Silica-Transmission-Gratings-v1.0.pdf>>.
- Budiansky, B, Drucker, DC, Kino, GS & Rice, JR, 1979, 'Pressure sensitivity of a clad optical fiber', *Applied Optics*, vol. 18, no. 24, pp. 4085-8.
- Canning, J, 2008, 'Fibre gratings and devices for sensors and lasers', *Laser & Photonics Review*, vol. 2, no. 4, pp. 275-89.
- Chavel, P & Strand, TC, 1984, 'Range measurement using Talbot diffraction imaging of gratings', *Applied Optics*, vol. 23, no. 6, pp. 862-71.
- Chen, CG & Schattenburg, ML, 2004, 'A Brief History of Gratings and the Making of the MIT Nanoruler', <<http://snl.mit.edu/pub/papers/WP/Nanoruler-White-Paper.pdf>>.
- Chen, LR & Azana, J, 2005, 'Spectral Talbot phenomena in sampled arbitrarily chirped Bragg gratings', *Optics Communications*, vol. 250, no. 4-6, pp. 302-8.
- Chuang, W, Bai-Ou, G, Zhi, W & Xinhuan, F, 2010, 'Characterization of pressure response of Bragg gratings in grapefruit microstructured fibers', *Journal of Lightwave Technology*, vol. 28, no. 9, pp. 1392-7.
- Clough, RW, 1980, 'The finite element method after twenty-five years: A personal view', *Computers & Structures*, vol. 12, no. 4, pp. 361-70.
- COMSOL Inc, n.d., *Step-index fiber*, viewed 21 May 2019, <<https://www.comsol.com/model/step-index-fiber-145>>.
- Cooksey, GA & Ahmed, Z, 2016, 'Optofluidic temperature and pressure measurements with fiber Bragg gratings embedded in microfluidic devices', *TechConnect World Innovation Conference & Expo*, Washington, DC,
- Correia, R, Chehura, E, James, SW & Tatam, RP, 2007, 'A pressure sensor based upon the transverse loading of a sub-section of an optical fibre Bragg grating', *Measurement Science & Technology*, vol. 18, no. 10, pp. 3103-10.

- Correia, R, Chehura, E, Li, J, James, SW & Tatam, RP, 2010, 'Enhanced sensitivity fibre Bragg grating (FBG) load sensor', *Measurement Science & Technology*, vol. 21, no. 9.
- Dianov, EM, Golant, KM, Mashinsky, VM, Medvedkov, OI, Nikolin, IV, Sazhin, OD & Vasiliev, SA, 1997, 'Highly photosensitive nitrogen-doped germanosilicate fibre for index grating writing', *Electronics Letters*, vol. 33, no. 15, pp. 1334-6.
- Doyle, KB, Hoffman, JM, Genberg, VL & Michels, GJ, 2002, 'Stress birefringence modeling for lens design and photonics', *Proc. SPIE*, vol. 4832, pp. 436-47.
- Dragomir, NM, 2004, 'Microscopic characterisation of photonic devices', PhD thesis, Victoria University, Australia.
- Dragomir, NM, Rollinson, C, Wade, SA, Stevenson, AJ, Collins, SF, Baxter, GW, Farrell, PM & Roberts, A, 2003, 'Nondestructive imaging of a type I optical fiber Bragg grating', *Optics Letters*, vol. 28, no. 10, pp. 789-91.
- Dyer, PE, Farley, RJ & Giedl, R, 1995, 'Excimer laser irradiated phase masks for grating formation', *IET Conference Proceedings*, Institution of Engineering and Technology, p.2.
- Echevarria, J, Quintela, A, Jauregui, C & Lopez-Higuera, JM, 2001, 'Uniform fiber Bragg grating first- and second-order diffraction wavelength experimental characterization for strain-temperature discrimination', *Photonics Technology Letters, IEEE*, vol. 13, no. 7, pp. 696-8.
- El-Diasty, F, 2000, 'Multiple-beam interferometric determination of Poisson's ratio and strain distribution profiles along the cross section of bent single-mode optical fibers', *Applied Optics*, vol. 39, no. 19, pp. 3197-201.
- Electronicast, 2012, *Fiber Optic Sensors*, <<http://www.jphotonics.cn/news-detail.asp?id=181>>.
- Espejo, RJ & Dyer, SD, 2007, 'Transverse-stress fiber Bragg grating sensor with high spatial resolution and temperature stability', *Journal of Lightwave Technology*, vol. 25, no. 7, pp. 1777-85.
- Giallorenzi, TG, Bucaro, JA, Dandridge, A, Sigel, GH, Cole, JH, Rashleigh, SC & Priest, RG, 1982, 'Optical fiber sensor technology', *IEEE Journal of Quantum Electronics*, vol. 18, no. 4, pp. 626-65.
- Gianino, PD & Bendow, B, 1981, 'Calculations of stress-induced changes in the transverse refractive-index profile of optical fibers', *Applied Optics*, vol. 20, no. 3, pp. 430-4.
- Gloge, D, 1971, 'Weakly guiding fibers', *Applied Optics*, vol. 10, no. 10, pp. 2252-8.
- Goh, XM, Kou, SS, Kouskousis, BP, Dragomir, NM, Collins, SF, Baxter, GW & Roberts, A, 2014, 'Non-destructive three-dimensional optical imaging of a fiber Bragg grating', *IEEE Photonics Journal*, vol. 6, no. 5, pp. 1-7.

- Guigay, JP, Zabler, S, Cloetens, P, David, C, Mokso, R & Schlenker, M, 2004, 'The partial Talbot effect and its use in measuring the coherence of synchrotron X-rays', *Journal of Synchrotron Radiation*, vol. 11, pp. 476-82.
- Harrison, GR, 1949, 'The production of diffraction gratings I. Development of the ruling art', *Journal of Optical Society of America*, vol. 39, no. 6, pp. 413-26.
- Harrison, GR & Loewen, EG, 1976, 'Ruled gratings and wavelength tables', *Applied Optics*, vol. 15, no. 7, pp. 1744-7.
- Hill, KO, 2000, 'Photosensitivity in optical fiber waveguides: from discovery to commercialization', *IEEE Journal of Selected Topics in Quantum Electronics*, vol. 6, no. 6, pp. 1186-9.
- Hill, KO, Malo, B, Bilodeau, F, Johnson, DC & Albert, J, 1993, 'Bragg gratings fabricated in monomode photosensitive optical fiber by UV exposure through a phase mask', *Applied Physics Letters*, vol. 62, no. 10, pp. 1035-7.
- Hill, KO, Malo, B, Bilodeau, F, Johnson, DC, Morse, TF, Kilian, A, Reinhart, L & Oh, K, 1991, 'Photosensitivity in Eu<sub>2+</sub>:Al<sub>2</sub>O<sub>3</sub>-doped-core fiber: Preliminary results and application to mode converters', *Optical Fiber Communication*, San Diego, California, Optical Society of America, PD3
- Hill, KO & Meltz, G, 1997, 'Fiber Bragg grating technology fundamentals and overview', *Journal of Lightwave Technology*, vol. 15, no. 8, pp. 1263-76.
- Hocker, GB, 1979, 'Fiber-optic sensing of pressure and temperature', *Applied Optics*, vol. 18, no. 9, pp. 1445-8.
- Hosono, H, Abe, Y, Kinser, DL, Weeks, RA, Muta, K & Kawazoe, H, 1992, 'Nature and origin of the 5-EV band in SiO<sub>2</sub>:GeO<sub>2</sub> glasses', *Physical Review B*, vol. 46, no. 18, pp. 11445-51.
- Hosono, H, Kawazoe, H & Nishii, J, 1996, 'Defect formation in SiO<sub>2</sub>:GeO<sub>2</sub> glasses studied by irradiation with excimer laser light', *Physical Review B*, vol. 53, no. 18, pp. 11921-3.
- Hsu, YS, Likarn, W, Wen-Fung, L & Chiang, YJ, 2006, 'Temperature compensation of optical fiber Bragg grating pressure sensor', *IEEE Photonics Technology Letters*, vol. 18, no. 7, pp. 874-6.
- Huang, J, Zhou, Z, Tan, Y, Liu, M & Zhang, D, 2014, 'Design and experimental study of a fiber Bragg grating pressure sensor', *Proceedings of the 2014 International Conference on Innovative Design and Manufacturing (ICIDM)*, IEEE, pp.217-21.
- James, SW, Dockney, ML & Tatam, RP, 1996, 'Simultaneous independent temperature and strain measurement using in-fibre Bragg grating sensors', *Electronics Letters*, vol. 32, no. 12, pp. pp.1133-4.
- Kanakaraj, U, Lhaden, T & Karthic, RV, 2015, 'Analysis of structural mechanics of solid microneedle using COMSOL software', *2015 International Conference on Innovations in Information, Embedded and Communication Systems (ICIIECS)*, IEEE, 1-5

- Kashyap, R, Armitage, JR, Wyatt, R, Davey, ST & Williams, DL, 1990, 'All-fibre narrowband reflection gratings at 1500 nm', *Electronics Letters*, vol. 26, no. 11, pp. 730-2.
- Keck, DB, 1981, "Fundamentals of optical fiber communications." edited by MK Barnoski (Academic Press, New York, 1981).
- Kersey, A, Davis, MA, Patrick, HJ, Leblanc, M, Koo, KP, Askins, CG, Putnam, MA & Friebele, EJ, 1997, 'Fiber grating sensors', *Journal of Lightwave Technology*, vol. 15, no. 8, pp. 1442-63.
- Kersey, AD, 2012, 'Fiber optic sensors shine bright: industrial applications where FOS bring differentiated performance/value', *Proc. SPIE*, vol. 8421, p.4.
- Kouskousis, BP, 2009, 'Microscopic characterisation of fiber Bragg grating', PhD thesis, Victoria University, Australia.
- Kouskousis, BP, Kitcher, DJ, Collins, SF & Baxter, GW, 2013, 'Numerical investigation on the effects of fabrication conditions on fiber Bragg grating spectra using the phase mask technique', *Applied Optics*, vol. 52, no. 14, pp. 3338-44.
- Lam, DKW & Garside, BK, 1981, 'Characterization of single-mode optical fiber filters', *Applied Optics*, vol. 20, no. 3, pp. 440-5.
- Latimer, P, 1993a, 'Talbot effect reinterpreted - reply', *Applied Optics*, vol. 32, no. 19, pp. 3468-9.
- Latimer, P, 1993b, 'Talbot plane patterns - grating images or interference effects', *Applied Optics*, vol. 32, no. 7, pp. 1078-83.
- Latimer, P, 1993c, 'Use of the Talbot effect to couple the phases of lasers', *Applied Physics Letters*, vol. 62, no. 3, pp. 217-8.
- Lawrence, CM, Nelson, DV, Udd, E & Bennett, T, 1999, 'A fiber optic sensor for transverse strain measurement', *Experimental Mechanics*, vol. 39, no. 3, pp. 202-9.
- Leduc, D, Lecieux, Y, Morvan, P-A & Lupi, C, 2013, 'Architecture of optical fiber sensor for the simultaneous measurement of axial and radial strains', *Smart Materials and Structures*, vol. 22, no. 7.
- Lemaire, PJ, Atkins, RM, Mizrahi, V & Reed, WA, 1993, 'High pressure H<sub>2</sub> loading as a technique for achieving ultra high UV photosensitivity and thermal sensitivity in GeO<sub>2</sub> doped optical fibres', *Electronics Letters*, vol. 29, no. 13, pp. 1191-3.
- Limberger, HG, Fonjallaz, PY, Lambelet, P, Salathe, RP, Zimmer, C & Gilgen, HH, 1993, 'OLCR characterization of efficient Bragg gratings in optical-fiber', *Proc. SPIE*, vol. 2044, pp.272-83.
- Liu, HY, Liu, HB & G.D., P, 2005, 'Tensile strain characterization of polymer optical fibre Bragg grating', *Optical Communication*, vol. 251, no. 1-3, pp. 37-43.
- Liu, L, 1988a, 'Interferometry based on the partially coherent effect lying between the Talbot and Lau effects', *Journal of Modern Optics*, vol. 35, no. 10, pp. 1605-18.

- Liu, L, 1988b, 'Partially coherent diffraction effect between Lau and Talbot effects', *Journal of the Optical Society of America A*, vol. 5, no. 10, pp. 1709-16.
- Liu, L, Zhang, H, Zhao, Q, Liu, Y & Li, F, 2007, 'Temperature-independent FBG pressure sensor with high sensitivity', *Optical Fiber Technology*, vol. 13, no. 1, pp. 78-80.
- Liu, Y, Guo, Z, Zhang, Y, Chiang, KS & Dong, X, 2000, 'Simultaneous pressure and temperature measurement with polymer-coated fibre Bragg grating', *Electronics Letters*, vol. 36, no. 6, pp. 564-6.
- Loewen, E & Popov, E 1997, *Diffraction gratings and applications*, Taylor & Francis, NY, USA.
- Ma, Y, 2009, 'Characterization of higher order modes in optical fibers', PhD thesis, University of Erlangen-Nuremberg, Germany.
- Malo, B, Hill, KO, Bilodeau, F, Johnson, DC & Albert, J, 1993, 'Point-by-point fabrication of micro-Bragg gratings in photosensitive fibre using single excimer pulse refractive index modification techniques', *Electronics Letters*, vol. 29, no. 18, pp. 1668-9.
- Mastro, S, A., 2005, 'Optomechanical behavior of embedded fiber Bragg grating strain sensors', PhD thesis, Drexel University, PA, USA.
- McLandrich, MN & Rast, HE, 1978, 'Fiber interferometer gyroscope', *Proc. SPIE*, vol. 157, pp.127-30.
- Mehta, DS, Dubey, SK, Shakher, C & Takeda, M, 2006, 'Two-wavelength Talbot effect and its application for three-dimensional step-height measurement', *Applied Optics*, vol. 45, no. 29, pp. 7602-9.
- Meltz, G, Morey, WW & Glenn, WH, 1989, 'Formation of Bragg gratings in optical fibers by a transverse holographic method', *Optics Letters*, vol. 14, no. 15, pp. 823-5.
- Méndez, A, 2007, 'Fiber Bragg grating sensors: a market overview', *Proc. SPIE*, vol. 6619, p.661905.
- Mihailov, SJ, 2012, 'Fiber Bragg Grating Sensors for Harsh Environments', *Sensors*, vol. 12, no. 2, p. 1898.
- Mills, JD, Hillman, CWJ, Blott, BH & Brocklesby, WS, 2000, 'Imaging of free-space interference patterns used to manufacture fiber Bragg gratings', *Applied Optics*, vol. 39, no. 33, pp. 6128-35.
- Nishii, J, Kitamura, N, Yamanaka, H, Hosono, H & Kawazoe, H, 1995, 'Ultraviolet-radiation-induced chemical-reactions through one-photon and 2-photon absorption processes in GeO<sub>2</sub>-SiO<sub>2</sub> glasses', *Optics Letters*, vol. 20, no. 10, pp. 1184-6.
- Osuch, T & Jaroszewicz, Z, 2017, 'Influence of optical fiber location behind an apodized phase mask on Bragg grating reflection efficiencies at Bragg wavelength and its harmonics', *Optics Communications*, vol. 382, pp. 36-41.

- Othonos, A & Kyriacos, K 1999, *Fiber Bragg gratings -fundamentals and applications in telecommunications and sensing*, Artech House, MA, USA.
- Pachava, VR, Kamineni, S, Madhuvarasu, SS & Putha, K, 2014, 'A high sensitive FBG pressure sensor using thin metal diaphragm', *Journal of Optics*, vol. 43, no. 2, pp. 117-21.
- Pachava, VR, Kamineni, S, Madhuvarasu, SS, Putha, K & Mamidi, VR, 2015, 'FBG based high sensitive pressure sensor and its low-cost interrogation system with enhanced resolution', *Photonic Sensors*, vol. 5, no. 4, pp. 321-9.
- Patent Insight Pro, 2011, 'Technology Insight Report: Fibre Optic Sensors', <<http://www.patentinsightpro.com/techreports/0811/Techonology%20Insight%20Report%20-%20Fiber%20Optic%20Sensors.pdf>>.
- Paul, J, Zhao, LP, Ngoi, BKA & Fang, ZP, 2005, 'Evaluation of the effect of polymer coating on the lateral pressure tuning of fiber Bragg gratings', *Applied Physics Letters*, vol. 86, no. 23, pp. 231107-13.
- Pelosi, G, 2007, 'The finite-element method, Part I: R. L. Courant [Historical Corner]', *Antennas and Propagation Magazine, IEEE*, vol. 49, no. 2, pp. 180-2.
- Peng, GD, 2002, 'Prospects of polymer optical fibres and gratings in sensing', *Proceedings of the International Conference on Optical Fiber Sensors*, IEEE, pp.714-6.
- Peters, K, 2011, 'Polymer optical fiber sensors-a review', *Smart Materirals and Structures*, vol. 20, no. 1, pp. 1-17.
- Pinet, E, 2011, 'Pressure measurement with fiber-optic sensors: Commercial technologies and applications', *Proc. SPIE*, vol. 7753, p.775304.
- Poeggel, S, Tosi, D, Duraibabu, D, Leen, G, McGrath, D & Lewis, E, 2015, 'Optical fibre pressure sensors in medical applications', *Sensors*, vol. 15, no. 7, p. 17115.
- Poole, C, Wiesenfeld, JM, DiGiovanni, DJ & Vengsarkar, AM, 1994, 'Optical fiber-based dispersion compensation using higher order modes near cutoff', *Journal of Lightwave Technology*, vol. 12, no. 10, pp. 1746-58.
- Prabhugoud, M & Peters, K, 2007, 'Finite element analysis of multi-axis strain sensitivities of Bragg gratings in PM fibers', *Journal of Intelligent Material Systems and Structures*, vol. 18, no. 8, pp. 861-73.
- Rayleigh, L, 1881, 'On the manufacture and theory of diffraction grating', *Philosophical Magazine*, vol. 11, pp. 196-205.
- Rivera, MJ, Molina, JAL, Trujillo, M, Romero-García, V & Berjano, EJ, 2010, 'Analytical validation of COMSOL multiphysics for theoretical models of radiofrequency ablation including the hyperbolic bioheat transfer equation', *2010 Annual International Conference of the IEEE Engineering in Medicine and Biology*, IEEE, 3214-7
- Rollinson, CM, 2012, 'Microscopic and spectral characterisation of optical fibre Bragg gratings', PhD thesis, Victoria University, Australia.

- Rollinson, CM, Wade, SA, Dragomir, NM, Baxter, GW, Collins, SF & Roberts, A, 2005, 'Reflections near 1030nm from 1540nm fibre Bragg gratings: Evidence of a complex refractive index structure', *Optics Communications*, vol. 256, no. 4-6, pp. 310-8.
- Russell, PSJ, Hand, DP, Chow, YT & Poyntz-Wright, LJ, 1991, 'Optically induced creation, transformation, and organization of defects and color centers in optical fibers', *Proc. SPIE*, vol. 1516, p.8.
- Shang, Q & Lin, B, 2010, 'Simulation and analysis on hydrostatic pressure sensor using fiber Bragg grating', *2010 International Conference on Measuring Technology and Mechatronics Automation (ICMTMA)*, IEEE, 362-5
- Shu, X, Zhao, D, Liu, Y, Gwandum, B, Floreani, F, Zhang, L & Bennion, I, 2002, 'Effectively simultaneous temperature and strain measurement utilising a dual-grating sensor formed by type IA and type IIA FBGs', *Sensors, 2002, Proceedings of IEEE*, vol. 2, pp.1740-5.
- Sirkis, JS, 1993, 'Unified approach to phase -strain temperature models for smarts structure interferometric optical fiber sensors', *Optical Engineering*, vol. 32, pp. 752-9.
- Smelser, CW, Grobnic, D & Mihailov, SJ, 2004, 'Generation of pure two-beam interference grating structures in an optical fiber with a femtosecond infrared source and a phase mask', *Optics Letters*, vol. 29, no. 15, pp. 1730-2.
- Snyder, AW & Love, J 2012, *Optical Waveguide Theory*, Springer US.
- Srimannarayana, K, Rao, PV, Shankar, MS & Kishore, P, 2014, 'FBG sensor for temperature-independent high sensitive pressure measurement with aid of a Bourdon tube', *Proc. SPIE*, vol. 9141, p.91412E.
- Starinshak, DP, Smith, ND & Wilson, JD, 2008, 'Using COMSOL multiphysics software to model anisotropic dielectric and metamaterial effects in folded-waveguide traveling-wave tube slow-wave circuits', *2008 IEEE International Vacuum Electronics Conference*, 162-3
- Talbot, HF, 1836, 'Facts relating to optical sciences', *The London Edinburgh Philosophical Magazine and Journal of Science (Third Series)*, vol. 9, pp. 401-7.
- Tarnowski, K & Urbanczyk, W, 2013, 'Origin of Bragg reflection peaks splitting in gratings fabricated using a multiple order phase mask', *Optics Express*, vol. 21, no. 19, pp. 21800-10.
- Toroghi, S, Latifi, H, Afshari, M & Aref, SH, 2006, 'A new structure of fiber Bragg grating with increased sensitivity to pressure and decreased sensitivity to temperature', *International Conference on Laser, Applications, and Technologies 2005: Laser Sensing, Imaging, and Information Technologies*, vol. 6162, p. Q1620.
- Udd, E, Black, K, Schulz, W, Kreger, S, Kunzler, M & Heider, D, 2002, 'In-situ evaluation of composite structural performance in presence of high stress/strain gradients using multi-axis fiber grating strain sensors', *Proceedings of Optical*

*Fiber Sensors Conference Technical Digest, OFS 2002*, vol. 1, IEEE, OR, USA, pp.59-62.

- Udd, E, Schulz, W, Seim, J, Haugse, E, Trego, A, Johnson, P, Bennett, TE, Nelson, D & Makinod, A, 2000, 'Multidimensional strain field measurements using fiber optic grating sensors', *Proc. SPIE*, vol. 3986, pp.254-62.
- Vorathin, E, Hafizi, ZM, Aizzuddin, AM & Lim, KS, 2018a, 'A highly sensitive multiplexed FBG pressure transducer based on natural rubber diaphragm and ultrathin aluminium sheet', *Optics & Laser Technology*, vol. 106, pp. 177-81.
- Vorathin, E, Hafizi, ZM, Aizzuddin, AM & Lim, KS, 2018b, 'A natural rubber diaphragm based transducer for simultaneous pressure and temperature measurement by using a single FBG', *Optical Fiber Technology*, vol. 45, pp. 8-13.
- Wade, SA, Robertson, DF, Thompson, AC & Stoddart, PR, 2011, 'Changes in spectral properties of fibre Bragg gratings owing to bending', *Electronics Letters*, vol. 47, no. 9, pp. 558-9.
- Wagreich, RB, Atia, WA, Singh, H & Sirkis, JS, 1996, 'Effects of diametric load on fibre Bragg gratings fabricated in low birefringent fibre', *Electronics Letters*, vol. 32, no. 13, pp. 1223-4.
- Williams, DL, Ainslie, BJ, Armitage, JR, Kashyap, R & Campbell, R, 1993, 'Enhanced UV photosensitivity in boron codoped germanosilicate fibres', *Electronics Letters*, vol. 29, no. 1, p. 45.
- Xie, WX, Douay, M, Bernage, P, Niay, P, Bayon, JF & Georges, T, 1993, '2nd-order diffraction efficiency of Bragg gratings written within Germanosilicate fibers', *Optics Communications*, vol. 101, no. 1-2, pp. 85-91.
- Xiong, Z, Peng, GD, Wu, B & Chu, PL, 1999, 'Highly Tunable Bragg Gratings in Single-Mode Polymer Optical Fibers', *IEEE Photonics Technology Letters*, vol. 11, no. 3, pp. 352-4.
- Xu, MG, Archambault, JL, Reekie, L & Dakin, JP, 1994, 'Discrimination between strain and temperature effects using dual-wavelength fibre grating sensors', *Electronics Letters*, vol. 30, no. 13, pp. 1085-7.
- Xu, MG, Geiger, H & Dakin, JP, 1996, 'Fibre grating pressure sensor with enhanced sensitivity using a glass-bubble housing', *Electronics Letters*, vol. 32, pp. 128-9.
- Xu, MG, Reekie, L, Chow, YT & Dakin, JP, 1993, 'Optical in-fibre grating high pressure sensor', *Electronics Letters*, vol. 29, no. 4, pp. 398-9.
- Yam, SP, Brodzeli, Z, Kouskousis, BP, Rollinson, CM, Wade, SA, Baxter, GW & Collins, SF, 2009, 'A phase-shifted fiber Bragg grating fabricated using a single phase mask', *14th Opto Electronics and Communications Conference*, Hong Kong, China, 1-2
- Yam, SP, Kitcher, DJ, Wade, SA, Baxter, GW & Collins, SF, 2008, 'Investigation of wavelength variations of fibre Bragg grating features using a chirped phase mask', *Journal of Optics A-Pure and Applied Optics*, vol. 10, no. 5.

- Yan, C, Ferraris, E, Geernaert, T, Berghmans, F & Reynaerts, D, 2010, 'Development of flexible pressure sensing polymer foils based on embedded fibre Bragg grating sensors', *Procedia Engineering*, vol. 5, pp. 272-5.
- Yan, C, Ferraris, E & Reynaerts, D, 2011, 'A pressure sensing sheet based on optical fibre technology', *Procedia Engineering*, vol. 25, pp. 495-8.
- Yuan, W, Stefani, A, Bache, M, Jacobsen, T, Rose, B, Herholdt-Rasmussen, N, Nielsen, FK, Andresen, S, Sørensen, OB, Hansen, KS & Bang, O, 2011, 'Improved thermal and strain performance of annealed polymer optical fiber Bragg gratings', *Optics Communications*, vol. 284, no. 1, pp. 176-82.
- Yunqi, L, Zhuanyun, G, Ying, Z, Kin Seng, C & Xiaoyi, D, 2000, 'Simultaneous pressure and temperature measurement with polymer-coated fibre Bragg grating', *Electronics Letters*, vol. 36, no. 6, pp. 564-6.
- Zhang, Y, Feng, D, Liu, Z, Guo, Z, Dong, X, Chiang, KS & Chu, BCB, 2001, 'High-sensitivity pressure sensor using a shielded polymer-coated fiber Bragg grating', *IEEE Photonics Technology Letters*, vol. 13, no. 6, pp. 618-9.
- Zhao, Y, Zheng, H, Lv, R & Yang, Y, 2018, 'A practical FBG pressure sensor based on diaphragm-cantilever', *Sensors and Actuators A: Physical*, vol. 279, pp. 101-6.
- Zheng, XH, 1986, 'Finite-element analysis for fused couplers', *Electronics Letters*, vol. 22, no. 15, pp. 804-5.
- Zhong, X, Wang, Y, Liao, C, Liu, S, Tang, J & Wang, Q, 2015, 'Temperature-insensitivity gas pressure sensor based on inflated long period fiber grating inscribed in photonic crystal fiber', *Optics Letters*, vol. 40, no. 8, pp. 1791-4.